

Universidad de Granada

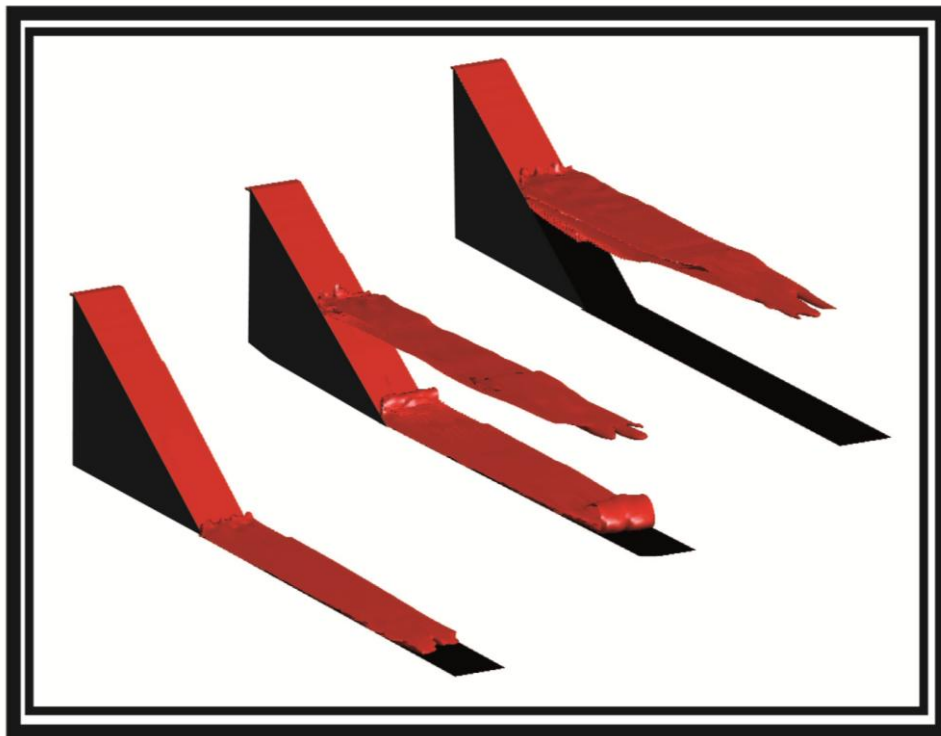
Departamento de Ingeniería Civil e Instituto de Investigación del Agua

Programa de Doctorado en Ingeniería Civil



SPLITTING GRAVITY CURRENTS IN STRATIFIED SYSTEMS

COMPORTAMIENTO DE CORRIENTES DE GRAVEDAD EN
SISTEMAS ESTRATIFICADOS



Tesis Doctoral

Alicia Cortés Cortés

Granada 2014

Universidad de Granada

Departamento de Ingeniería Civil e Instituto de Investigación del Agua

Programa de Doctorado en Ingeniería Civil



**SPLITTING GRAVITY CURRENTS IN
STRATIFIED SYSTEMS**

COMPORTAMIENTO DE CORRIENTES DE GRAVEDAD EN
SISTEMAS ESTRATIFICADOS

Memoria presentada para la obtención del
Grado de Doctor por la Universidad de Granada
con Mención de Doctorado Internacional

Autor: Alicia Cortés Cortés

Director: Dr. Francisco J. Rueda Valdivia

Granada 2014

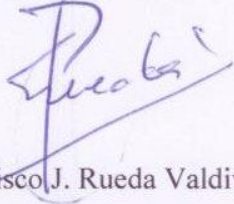
Editor: Editorial de la Universidad de Granada
Autor: Alicia Cortés Cortés
D.L.: GR 1967-2014
ISBN: 978-84-9083-167-0

TESIS DOCTORAL 2014

La doctoranda, Alicia Cortés Cortés, y el director de la tesis Francisco J. Rueda Valdivia garantizamos, al firmar esta tesis doctoral, que el trabajo ha sido realizado por el doctorando bajo la dirección del director de la tesis y hasta donde nuestro conocimiento alcanza, en la realización del trabajo, se han respetado los derechos de otros autores a ser citados, cuando se han utilizado sus resultados o publicaciones.

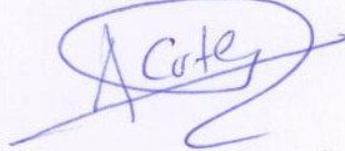
Granada, Junio de 2014

Director de la Tesis



Fdo.: Francisco J. Rueda Valdivia

Doctorando



Fdo.: Alicia Cortés Cortés

*A todos los que estimo,
por hacerme siempre sonreír*

This work was funded by the Spanish Ministry of Science and Innovation
(project CGL2008-06101/BOS)

ACKNOWLEDGEMENTS

It is weird that for a long time I have been looking forward to writing the acknowledgements of my thesis, and now that the chance has come I do not even know how to start. I feel more comfortable expressing my gratitude in Spanish, so I apologize for the switch in the language, but I will make sure that I write the part where I say 'thanks' to you in English.

Echando la vista atrás, hoy veo más claro que nunca que este trabajo no es sólo el esfuerzo de una persona, sino de todo el mundo que me ha rodeado durante estos cinco años. Es difícil citarlos a todos, por eso, perdonad aquellos que no aparezcáis nombrados a continuación. Sin embargo, sabéis que no tengo palabras para daros las GRACIAS en mayúsculas.

Quisiera dedicar mis primeras palabras de gratitud a Francisco Rueda, por su papel como director de tesis. Trabajador incansable, siempre al pie del cañón a pesar de las muchas obligaciones que tienes, fuente inagotable de ideas y mejoras. Gracias por no perder totalmente los nervios ante mis preguntas y despistes, por repetirme una y otra vez el “hilo conductor de la historia”. Tu profesionalidad, tus ganas por hacer “cosas ordinarias extraordinariamente bien”, me han enseñado no solo a saber de ciencia, sino a querer aprender a hacer ciencia.

Muchos sois los profesores y personal investigador de la Universidad de Granada y asociados los que, sin duda, habéis formado pieza fundamental en este rompecabezas. Ada, gracias por el tiempo invertido en la organización y realización de muestreos, tus recomendaciones en temas de calidad del agua (¡me llevo la espinita de no haber podido profundizar más en este tema, pero seguimos en contacto!), tus consejos y apoyo incondicional incluso bajo el efecto de “las lágrimas de fluoresceína”. Quique, gracias por aceptar mis continuas peticiones a “empaparte” en rodamina o levantar estaciones meteorológicas, por compartir conmigo tu conocimiento en la materia, y por aportar siempre esa chispa en el campo, cuyo recuerdo hoy dibuja en mi cara una sonrisa. *Bill, thanks for your multiple contributions to this work. You can not imagine how confident I felt if you were at the field experiments. Anything could be wrong if you were nearby. You have been a key element both in the field and in the office.* Victoria y Luis, pareja ejemplar a mis ojos, por haberme demostrado siempre su humanidad y ternura. JuanFran, gracias por ser un “punto de apoyo” más sólido, si cabe, que los que pusimos en nuestras rectificaciones de imágenes en Béznar.

Aunque cada etapa de este proceso de aprendizaje me ha enriquecido de muchas maneras, tal vez el trabajo de campo haya sido en el que haya “cultivado mejores frutos”. Muy larga es la lista de personas a las que he “engañado” para que me echarais una mano. Todos y cada uno de vosotros os merecéis el cielo. Y de forma más particular, sois muchos a los que quiero decir gracias. Un agradecimiento especial a Francisco Calvo y Eduardo Díaz (Agencia Andaluza del Agua, Granada), por proporcionarnos tanto datos hidrológicos del Embalse de Béznar como los permisos necesarios para realizar nuestras tareas de campo. Eduardo, gracias por tu apoyo y labor de guía. Mari Ángeles, fuiste la persona que me contaste la historia desde cero a mi llegada en 2009. Me enseñaste todo sobre estrategias e instrumentos de campo. Gracias por tu dedicación absoluta al proyecto y por el tiempo que compartimos juntas. Sergio, sorprendida me has dejado siempre con tus ideas de MacGyver. Gracias por tus soluciones. Clara, gracias por tu ayuda durante las primeras campañas del 2010. Y llegaste tú, mi Fátima. Daba igual cual fuera el obstáculo que nos tocara ese muestreo: caja de cambios rechinante, luna reventada, polea desaparecida, viento al atardecer hacia presa, barca pinchada con mayor entrada que salida de agua, tapones que se “suicidaban”. Podemos con todo, ¿verdad que sí? Nunca olvidaré todos los ratos compartidos contigo tanto en el campo como en el laboratorio. Y a vosotros también os tocó la china en numerosas ocasiones, mis compis de laboratorio (Anna, Andrea, Mario y Cintia). Seguro que os echabais a temblar cada vez que salía el tema de “campaña de campo en Béznar”. Os doy las gracias aquí, pero me reservo un agradecimiento más personalizado más adelante. También doy las gracias a los que habéis colaborado de forma espontánea en nuestras salidas al campo: Francisco Jiménez, Francisco Cruz, Jorge, Roberto, Javi, Andrés, Cristina, Luis. Gracias también al personal de la depuradora de El Valle, especialmente a Antonio, por ayudarnos en la recogida de muestras a largo plazo. Y una vez en el laboratorio, muchas son las personas que me han proporcionado los conocimientos técnicos necesarios para levantar todos los “inventos” de campo que nos traíamos entre manos. Gracias a al Servicio Técnico de la Universidad de Málaga por su análisis IPC-MS, a Renato y Tobías (EIC) por ayudarme con termistores y sensores meteorológicos, a Mauro y Mónica (EMS) por desmigajarme todos los detalles de CTD y fluorímetro, a Sofía (Instrumentación Analítica) por sus consejos técnicos, a Eulogio por tener siempre el Nissan a punto (¡todo un reto!) y por supuesto, a mis amigos de Ferretería Santa Clotilde por darme siempre soluciones prácticas a mis problemas de tuercas y tornillos.

Durante estos cinco años he conocido y trabajado con otros estudiantes de Máster y Doctorado, que han hecho el trabajo mucho más estimulante y agradable, y han convertido la tesis una experiencia muy humana. Quiero empezar dando las gracias a esas 22 personas con las que compartí mis cursos de doctorado en el CEAMA. Fue sorprendente lo bien que sobrellevamos tantas horas de Matlab, ejercicios de Mecánica de Fluidos, prácticas de campo ... Buen humor y motivación fueron los ingredientes de

aquel guiso sublime que se coció con nosotros. A pesar de que todos hemos seguido nuestro camino en diferentes lugares, quiero destacar el corazón tan bonito de personas como mi Inmi, Elisa, David, Gema o Montse, que demuestran que con mi llegada a Granada hice amistades que durarán mucho tiempo. Por otra parte, quiero dar las gracias a los investigadores del Instituto del Agua, un grupo de gente buena, que no sólo se preocupa por el trabajo, sino también por las personas que los rodean. Me alegro mucho de haberos conocido Cris, Guille, Irene, Marco, Ana, Emilio, Javito, Tere y Sergio. Y de nuevo, gracias a los que me habéis acompañado en ese despacho con ambiente de biblioteca estos años. Tanto fuera como dentro me habéis demostrado que hemos formado una buena piña. Anna y Andrea, gracias por haber sido mis mamis en el instituto. Mario, gracias por tu paciencia y aceptar ser “el informático” del despacho. Cintia, mi pendejilla isleña. Demasiadas horas discutiendo sobre lingüística castellana... Ni te imaginas lo que me ha ayudado tu carácter tranquilo a bajar mi ritmo frenético. No me importaría salir contigo otra vez más a comer bajo el sol granadino en compañía de nuestros amigos felinos. Gracias a todos por vuestra simpatía, espontaneidad, alegría y amistad. Gracias también a todo el personal del Instituto del Agua (Maribel, Maria Angustias, Paco, Antonio), quienes desde un principio me habéis hecho sentir como en casa.

My thesis has involved a stay at the University of Toronto, in Canada. I want to thank Mathew Wells, for his enthusiasm to my request of visiting them and all his help in the lab (even if I was an absolute disaster at the beginning ...). He has been extremely helpful, motivating, and very patient to teach me when I did not know anything about laboratory. I also want to thank the graduate students, postdocs and technicians who I met during my stay: Sisi, Bill, Remo, Patricia, Bogdan, Alex. I want to acknowledge also my Whitney family who made my stay a pleasure: Michael, Rebecca, Regina, Neeru, Rob, Jessica, Diana, Marcel, David or Paul.

Tanto o más importantes como las personas relacionadas con el trabajo, son aquellos que no tienen nada que ver con él. Ellos me han hecho tener una vida plena, saludable, y siempre, siempre me han apoyado para que esta tarea terminase bien. Gracias a los que me habéis demostrado ser amigos desde siempre: Ruth, Valeria, María, Sara, Montse, Esther, Yanet, Sandra, Irene, Almu, así como mis “agronomitos” madrileños, o mis personitas del Erasmus como tú, mi Mari Carmen. Y por supuesto, gracias a mi tropa granadina, quienes siempre han aguantado mis fricadas con una sonrisa y no se han cansado de ofrecerme planes capaces de mantener viva mi motivación por seguir adelante, como son mi Inmi, Jose, Antonio, Marcos, Anita, Lara, JuanPe, Rocío, Paco, Héctor, mis dos Anas, Carlos, Sandra, David, Lucas, Andreu. No puedo olvidar a mis queridos profesionales en psicología, medicina y biología, con los que he compartido más de una carcajada, como mi Antonio, JuanLu, Lidia, Mari Jose, David, Andrés, Sabina, Jesús, Rebeca, Maribel; o mi familia en Almuñecar formada por Carmen, Victor, Olivia, Ruben, Alba, Carlos. Pero hay una familia mucho más sólida

creada durante los últimos años aquí en Granada. Y esa la formáis vosotras, mis Triviñeras-Angelitas: Jara, Ana y Elena. Vosotras erais las que hacíais que me sintiera que llegaba a casa por la noche, o encendíais la mañana cuando todavía teníamos los ojos cerrados deseándonos un feliz día. A todos y cada uno de vosotros, muchas gracias por estar siempre dispuestos a escucharme y tratar de encontrar soluciones, y simplemente, por ser un amigo de siempre y para siempre. Gracias de corazón por dejarme formar parte de vuestra vida estos años.

Y por supuesto, quiero agradecerle a mi familia: a mi padre Alfonso, a mi madre Engracia, a mi hermana Marta, a mi cuñado Edu, y en general al resto de mi familia. Me habéis demostrado en todo momento que pase lo que pase puedo sentirme segura, valorada y muy muy querida. Perdonad todos los momentos en los que os haya preocupado demasiado o por aquellos en los que no haya estado a vuestro lado todo lo que debería. Sin embargo, de sobra sabéis que sois la base de la que hoy soy y que sin vosotros esto no hubiera “tiraio pa’ late”. Un agradecimiento también muy especial para “mi familia adoptiva”, Mari Carmen, Jesús, Nieves, Sergio y abuela María. Gracias por estar pendientes de mí siempre, por hacer de un domingo cualquiera una bonita reunión familiar cuando la mía estaba tan lejos.

Y sí, faltas tú. Eres quien realmente has visto de cerca todo el camino, y por tanto sabes “toda la historia”. Eres quien más ha “sufrido” mis idas y venidas (sobre todo en los últimos meses), mis nervios, mis preocupaciones. Chema, gracias por estar conmigo los últimos años, por comprenderme, por ayudarme a tener más confianza en lo que puedo hacer por mí misma, y por hacerme entender lo que es querer estar con alguien para toda la vida.

RESUMEN EXTENSO

La entrada de agua fluvial cargada de nutrientes, así como materia orgánica fácilmente asimilable, representa uno de los mayores responsables del cambio en la ecología de sistemas acuáticos *estratificados*¹ (es decir, con gradientes verticales de densidad), dado que estas entradas controlan la distribución vertical de luz y nutrientes, y por tanto, la abundancia y composición de la comunidad fitoplanctónica. La respuesta bio-geoquímica del ecosistema a la entrada de un río cargado de nutrientes depende en gran medida de la distribución del agua fluvial en el sistema estratificado, es decir, de si el río fluye en superficie (*overflows*), o se hunde para formar intrusiones en la columna de agua. Ríos con flotabilidad positiva u *overflows* (es decir, menos densos que el agua ambiental en superficie) pueden incorporar nutrientes directamente en la capa superficial de mezcla (o *surface-mixed layer*, SML). Sin embargo, la disponibilidad en esta capa superficial de nutrientes disueltos en el agua de ríos con flotabilidad negativa (es decir, más densos que el agua ambiental en superficie) depende de la posición vertical a la que la intrusión se inserta en la columna de agua. Estas intrusiones formadas por ríos con flotabilidad negativa pueden fluir a lo largo de la base de la SML (*interflows*), o penetrar dicha capa para formar una intrusión en el metalimnion o en el fondo del sistema (*underflows*). En este trabajo, presentamos resultados de una serie de experimentos de campo, laboratorio y simulaciones numéricas para ilustrar los dos comportamientos mencionados de ríos con flotabilidad negativa (o de forma genérica, *corrientes de gravedad*), así como para demostrar la existencia de un tercer comportamiento, de acuerdo al cual se pueden formar varias intrusiones a la vez en la columna de agua debido a la entrada de una única corriente de gravedad. En este último caso, la corriente de gravedad se divide en dos partes (*split flows*): (a) una intrusión superficial a lo largo de la base de la SML, cuyos nutrientes disueltos pueden estar fácilmente disponibles para el crecimiento algal, y (b) una intrusión profunda que penetra la SML y forma una intrusión en el metalimnion. Sin embargo, no se han encontrado referencias bibliográficas que describan cuando *split flows* deberían formarse debido a la entrada de corrientes de gravedad en medios estratificados. Por tanto, nuestro conocimiento actual de las rutas de distribución de agua fluvial en estos sistemas acuáticos está todavía incompleto, a pesar de su importancia para la

¹ La columna de agua de un sistema acuático natural estratificado está normalmente caracterizada por una capa superficial más caliente y bien mezclada (es decir, de baja densidad y uniforme en profundidad) llamada 'capa superficial de mezcla', situada sobre una capa con gradientes de densidades que incrementan con profundidad, denominada metalimnion.

funcionalidad del ecosistema. Según esto, los principales objetivos de esta Tesis Doctoral han sido: (1) caracterizar la distribución vertical de corrientes de gravedad en sistemas acuáticos estratificados, (2) identificar las condiciones que favorecen la formación de intrusiones próximas a las base de la SML, y (3) cuantificar la fracción del flujo de flotabilidad de dicha corriente de gravedad que puede ser incorporada en las capas superficiales del sistema acuático.

En el campo, hemos realizado una serie de experimentos de trazadores bajo diferentes condiciones de estratificación para caracterizar las rutas de distribución del agua del río que entraba en un embalse estratificado del Mediterráneo (Embalse de Béznar, Granada, España). Según las condiciones de cada experimento, observamos que la corriente de gravedad fluyó en su totalidad a lo largo de la base de la SML (*interflow*), penetró dicha capa para formar una intrusión única y profunda en el metalimnion (*underflow*), o se dividió en dos para formar *split flows*. Durante el experimento realizado a finales del periodo de verano y principios del otoño, parte de la corriente de gravedad se separó del fondo del embalse tras impactar con la base de la capa superficial de mezcla, dando lugar a dos intrusiones: una en el metalimnion y otra a lo largo de la base de la SML. Esta última intrusión se incorporó en las capas más superficiales del embalse durante la noche siguiente al experimento, debido al engrosamiento de la SML por mezcla convectiva. Además, hemos parametrizado los tres comportamientos de la corriente de gravedad en el embalse en función de un número adimensional que hemos denominado ‘*número de Richardson en la transición*’, Ri_{12} , y que cuantificamos como el cociente entre el salto de densidad en la columna de agua que observamos en la base de la SML, y la diferencia de densidad entre la corriente de gravedad y dicha capa superficial, de la forma siguiente,

$$Ri_{12} = \left(\frac{\rho_2 - \rho_1}{\rho_0 - \rho_1} \right) \Gamma$$

Siendo ρ_0 , ρ_1 , y ρ_2 las densidades del agua del río, la capa superficial de mezcla, y la capa metalimnética situada bajo ella, respectivamente; y Γ es la dilución total que sufre la corriente de gravedad tanto la zona de hundimiento como a lo largo del fondo del embalse. Según nuestros resultados, la corriente de gravedad se separa del fondo (al menos parcialmente) y forma intrusiones en la base de la SML cuando $Ri_{12} \geq 1$. Por otra parte, la corriente penetra dicha capa superficial y forma intrusiones solo en el metalimnion si $Ri_{12} \ll 1$. En el Embalse de Béznar, la formación de intrusiones en la base de la capa de mezcla ocurre más frecuentemente durante periodos de máxima estratificación (verano), pero también se observan al comienzo del otoño cuando comienza el enfriamiento de la columna de agua. Además, hemos relacionado la formación de *split flows* tanto con (a) la formación de fluido interfacial en la capa más externa de la corriente de gravedad con propiedades cuyos valores son intermedios entre los observados en la corriente y en el agua ambiental, así como (b) la existencia cambios

bruscos de densidad en la base de la SML. Por otra parte, la formación de fluido interfacial entre la corriente de gravedad y el agua ambiental, lo hemos relacionado con: (1) la existencia de una capa superficial de mezcla profunda, (2) diluciones iniciales significativas en la zona de hundimiento; y (3) mezcla intensa en la capa interfacial entre corrientes de gravedad supercríticas y el agua ambiental. La interpretación del comportamiento de las corrientes de gravedad en campo está fundamentalmente basada en los resultados obtenidos en los siguientes experimentos de laboratorio.

A través de una serie de experimentos de laboratorio en un sistema estratificado en doble capa (ρ_1 en superficie y ρ_2 en el fondo, siendo $\rho_2 \gg \rho_1$), ilustramos como una corriente de gravedad confinada (bi-dimensional o 2D) puede dividirse en dos partes cuando choca con el salto de densidad ($\Delta\rho_{12} = \rho_2 - \rho_1$), y definimos las condiciones necesarias para que se formen *split flows* debido a la entrada de dicha corriente de gravedad en el sistema. Nuestras observaciones de laboratorio destacan la importancia de la presencia de gradientes internos en la corriente de gravedad (cuantificados mediante el ‘*número de Froude densimétrico*’, Fr , ver Ellison and Turner (1959)), además de la intensidad de la estratificación en la columna de agua (medida a través del ‘*número de Richardson densimétrico*’, Ri_ρ , ver Wells and Wettlaufer (2007)), en la caracterización del comportamiento de una corriente de gravedad cuando entra en un sistema estratificado en doble capa. El número de Froude densimétrico lo calculamos en función de las características promediadas en profundidad de la corriente de gravedad (velocidad U , espesor h , y gravedad reducida G'), de la siguiente forma,

$$Fr = \frac{U}{(G'h)^{1/2}}$$

mientras que la intensidad de la estratificación en función del número de Richardson densimétrico (Ri_ρ), la calculamos como,

$$Ri_\rho = \frac{g'_{12} H}{B_0^{2/3}}$$

siendo $g'_{12} = g \Delta\rho_{12} / \rho_1$ la gravedad reducida en el salto de densidad, g la aceleración gravitacional, B_0 el flujo de flotabilidad inicial de la corriente de gravedad por unidad de anchura, y H la distancia vertical desde la profundidad inicial de la corriente de gravedad hasta el salto de densidad. Nuestros resultados muestran que la corriente de gravedad tienen a dividirse en dos partes al chocar con un salto de densidad cuando la capa interfacial entre la corriente y el agua ambiental es difusa y gruesa (corrientes con régimen supercrítico, $Fr > 1$). Sin embargo, es más probable que la corriente de gravedad forme una única intrusión cuando la capa interfacial corriente-agua ambiental es de menor espesor (corrientes con régimen sub-crítico, $Fr < 1$). Usando los perfiles verticales que caracterizan los gradientes internos de una corriente de gravedad, hemos desarrollado una teoría que predice la partición del flujo de flotabilidad inicial de la

corriente de gravedad que fluye como *interflow* y *underflow* cuando dicha corriente se divide al encontrar un salto de densidad. Además, hemos confirmado nuestras predicciones sobre dichas fracciones mediante la información de los cambios de densidad observados en el sistema estratificado debido a la entrada de dicha corriente. Sin embargo, los experimentos de laboratorio nos proporcionaron sólo un conjunto reducido de medidas para poder confirmar nuestra teoría sobre la partición del material de la corriente de gravedad, y por tanto, necesitábamos probar que nuestros argumentos eran también aplicables para otros regímenes en la corriente de gravedad (Fr) e intensidad de la estratificación (Ri_ρ) diferentes a los estudiados en laboratorio.

Finalmente, usamos simulaciones numéricas para confirmar y extender la teoría que desarrollamos en laboratorio sobre la partición del material de una corriente de gravedad en dos fracciones a su entrada en un sistema estratificado en doble capa. Observamos una buena correlación entre resultados de laboratorio y de simulaciones, que confirman la importancia de los dos números adimensionales descritos (Fr y Ri_ρ) en la determinación de la partición de una corriente de gravedad cuando entra un sistema estratificado. En general, observamos mayores cambios de densidad en el agua ambiental debido al choque de corrientes de gravedad supercríticas ($Fr > 1$) con grandes saltos de densidad ($Ri_\rho \gg 1$). Además, hemos usado los resultados del modelo para evaluar los errores en la estimación de las fracciones en las que se divide el material de la corriente de gravedad debido a la incertidumbre ocasionada tanto a la posición donde se hicieron las medidas experimentales, como debido a las diferentes fuentes de error asociadas al modelo numérico. Una vez evaluados estos errores, los resultados de las simulaciones nos han permitido caracterizar el proceso de partición del flujo de flotabilidad de la corriente de gravedad con regímenes (Fr) e intensidad de la estratificación (Ri_ρ) diferentes a los estudiados en laboratorio, en función de: (1) los cambios de los gradientes internos de la corriente de gravedad debido a su choque con el salto de densidad, y (2) el mecanismo predominante que causa la transformación de energía en el sistema estratificado debido a la inyección de la corriente de gravedad en el mismo. Primero, hemos parametrizado el nivel de re-estructuración de los gradientes internos de la corriente de gravedad debido al choque con un salto de densidad mediante relaciones lineales entre los cambios normalizados de las propiedades de la corriente de gravedad (velocidad y exceso de densidad) a través del salto de densidad, y los dos números adimensionales arriba descritos (Fr y Ri_ρ). A continuación, hemos usado un balance de fuerzas (flotabilidad vs. inercia) a ambos lados del salto de densidad para identificar las condiciones que controlan los diferentes comportamientos de la corriente de gravedad (*interflow*, *underflow*, *split flow*) para un conjunto de regímenes diferentes a los observados en laboratorio. En general, nuestros resultados indican que un predominio de las fuerzas de flotabilidad en la corriente de gravedad formada tras el salto de densidad da lugar a la formación de *underflows* fluyendo por el fondo del sistema, mientras que la formación de *interflows* a lo largo del salto de densidad está a

asociado con una mayor importancia relativa de las fuerzas de inercia en la corriente de gravedad formada tras su impacto con $\Delta\rho_{12}$. Además, observamos *split flows* cuando la reducción de tanto las fuerzas de inercia como de flotabilidad se compensaron tras el paso de la corriente de gravedad a través del salto de densidad. Finalmente, valores de eficiencia de mezcla calculados a partir de los resultados de nuestras simulaciones se encuentran en el extremo superior del rango de valores encontrados en la literatura (> 0.5), lo que sugiere que la energía introducida a través de una corriente de gravedad en un sistema estratificado tiende a almacenarse de forma irreversible (como energía potencial de referencia), siendo la mezcla el mecanismo predominante de transformación de energía (en lugar de disipación por esfuerzos viscosos), y causando cambios en la distribución de densidad del sistema. De acuerdo a las tendencias mostradas por nuestros resultados simulados de eficiencia de mezcla, los cambios de densidad en el agua ambiental son más obvios en experimentos donde tanto Fr como Ri_ρ son altos.

Resultados publicados de un amplio rango de medidas de campos muestran gradientes internos significativos de velocidad y densidad en los perfiles verticales de las corrientes de gravedad, las cuales, según nuestros argumentos en experimentos de campo, laboratorio y simulaciones numéricas, tendrán mayor tendencia a retener (o según el termino anglosajón '*detrain*') una parte de (o posiblemente todo) el material de dicha corriente en la base de la capa de mezcla. La formación de este tipo de intrusiones próximas a la SML y su incorporación en las capas superficiales puede resultar en flujos de nutrientes disueltos en el agua del río que queden disponibles en esta zona del embalse para su consumo. Por tanto, proponemos el uso combinado de la teoría analítica presentada sobre la partición del flujo de flotabilidad de la corriente de gravedad junto con simulaciones numéricas como una herramienta para predecir y cuantificar los flujos de nutrientes disueltos en el agua del río que pueden quedar retenidos en la base de la SML y, por tanto, disponibles para incorporarse en las capas superficiales donde serán utilizados para el crecimiento la comunidad fitoplanctónica. La distribución de estos nutrientes disueltos en el agua fluvial en capas superficiales puede influir en la ecología del sistema acuático natural y, por tanto, en su calidad del agua.

ABSTRACT

Rivers inflows, carrying large loads of nutrients, labile organic matter or particulates, represent one of the major drivers of the ecology in stratified water bodies (lakes, reservoirs, ocean), controlling the vertical distribution of light and nutrients, and hence, the abundance and composition of algal communities. The biogeochemical response of the ecosystem to inflows, largely depends on the pathways of distribution of river water in the system, i.e., whether they form overflows and inject nutrients directly into the surface mixed-layer (SML) or they plunge and sink as gravity currents below the base of the SML to form an unique intrusion. However, the availability at the surface layers of river-borne nutrients dissolved in gravity currents is controlled by the vertical position of the intrusions in the water column, which can either flow along the base of the SML (*interflows*), or penetrate this layer to form a metalimnetic or bottom intrusion (*underflows*).

In this work, we present results of a series of field, laboratory and numerical experiments to illustrate the two gravity current behaviors mentioned, and to demonstrate the existence of a third behavior where multiple intrusions can form. In the latter case, gravity currents ‘split’ into two portions: (a) a shallow intrusion at the base of the SML, which dissolved nutrients may be readily available for phytoplankton growth, and (b) a deep intrusion formed well below the SML in the metalimnion. No indications have been found in the literature of when *splitting* gravity currents should occur. As a result, the main aims of this dissertation are: (1) to characterize the fate of gravity currents water entering stratified water bodies, (2) to identify the conditions that favor the formation of intrusions near the base of the surface layers, and (3) to quantify the portion of the gravity currents which may be entrained into these top layers.

Our observations confirm the existence of the three described gravity current behaviors. In natural water bodies, the vertical distribution of the current changed within the stratification cycle. In addition, our observations stress the significance of the internal gradients within the gravity current, as well as the ambient stratification strength, on determining how a gravity current intrudes into a stratified ambient water. Gravity currents tend to intrude as a single intrusion when they have a sharp, more step-like density profile. However, gravity currents are more likely to detrain into two parts at a density step when they have a diffuse interface layer at the top of the current, which in turns, is linked to: (1) the existence of deep surface mixed layers; (2) large initial dilutions in the plunge zone; and (3) strong mixing rates occurring at the interface layer

between ambient water and gravity current. Using details of the internal structure of the gravity current, we developed an analytical theory to predict the partition of the inflowing buoyancy flux into the *interflow* and *underflow* when the gravity current splits at the density step, which is tested both experimentally and numerically.

As a result, this study provides the tools to predict and quantify the fraction of the gravity current material that could be retained at the base of the SML. Therefore, this portion of the river water, and thus its dissolved nutrients, may be available into the top layers, where they can be used for phytoplankton growth. The fate of the river-borne nutrients may influence the natural water bodies ecology and their water quality.

TABLE OF CONTENTS

Acknowledgements	i
Resumen Extenso	v
Abstract	xi
Table of Contents	xiii
List of Figures	xv
List of Tables.....	xxi
List of Symbols	xxiii
General Introduction and Objectives.....	1
<i>Chapter 1: Pathways of River Water to the Surface Layers of Stratified Reservoirs</i>	<i>7</i>
Abstract	9
Introduction	9
Methods.....	12
Results	18
Discussion	22
Conclusions	37
<i>Chapter 2: Experimental Observations of the Splitting of a Gravity Current at a Density Step in a Stratified Water Body.....</i>	<i>39</i>
Abstract	41
Introduction	41
Theory	45
Methods.....	50
Results	56
Discussion	60
Conclusions and implications.....	63
Appendix: Volume flux partition	64

Table of Contents

<i>Chapter 3: On the Development of Split Flows by Gravity Currents into Two-Layered Stratified Basins</i>	69
Abstract	71
Introduction	71
Methods.....	76
Results and discussion.....	82
Conclusions and remarks	101
General Conclusions	105
Conclusiones Generales	107
Scientific Production and Activity	111
References	115

LIST OF FIGURES

Fig. I.1. Conceptual model of a negatively-buoyant gravity currents entering a stratified system.	2
Fig. I.2. Behavior of a gravity current in a two-layered stratified environment, ρ_1 and ρ_2 : (a) interflows (b) underflows, and (c) split flows.	3
Fig. I.3. Aerial photograph of Lake Béznar (Spain).	4
Fig. 1.1. Conceptual model of a cold plunging inflow entering a stratified reservoir.	10
Fig. 1.2. (a) Lake Béznar bathymetry showing the location of the meteorological station and thermistor chains (M and S). Isobaths are represented every 10 m. The shaded area marks the sampling region during the tracer injections. (b, c, d) Cross-section locations during May, Jul, and Sep experiments, respectively. Isobaths are represented every 5 m from the water surface at the given time. Water surface elevation (wse) is also included in meters above sea level (m.a.s.l.) for each experiment.	13
Fig. 1.3. Stratification, heat fluxes and meteorological forcing during the tracer experiments at Lake Béznar. Each vertical set of Figs. correspond to May, Jul, and Sep experiments, respectively. The dashed and shadowed rectangles define the injection period (3 h). (a-c) Time series of reservoir temperature close to the inflow section (S – Fig. 1.2a), where the black line marks the depth of the surface mixed layer (SML) and the white line shows the nominal intrusion depth (NID). Isotherms are marked every 0.5°C. (d-f) Time series of wind speed (speed) and wind direction (dir.). (g-i) Heat fluxes (HF) at the surface of the reservoir ($W m^{-2}$): net surface heat flux omitting short wave radiation (S_H), and effective surface heat flux in the surface mixed layer (H^*). (j-l) Convective velocity (vel.) scale (w_*), and shear velocity scale (u_*) in $cm s^{-1}$	20
Fig. 1.4. Sep experiment data. (a) Geometry of the inflow basin and half-divergence angle of the main inflowing plume ($\delta = 90^\circ$). Transects X-0.5 and X-1 are also marked. (b) ADCP velocity east-west (top) and north-south (bottom) along transect X-0.5 (plunge zone). (c) ADCP velocity east-west (top) and north-south (bottom) in the buoyancy-dominated region, shortly after the plunge zone (X-1).	22
Fig. 1.5. Observed tracer concentration (tracer conc.) of Rhodamine WT (RWT) or fluorescein (FDA) and observed CTD-temperature profiles (temp. obsv.) collected close to the inflow section during each tracer experiments. The associated theoretical temperature profile (temp. theo.) defines the density step at the base of the SML. The temperature step ($T_1 - T_2$) and the field value of the transition Richardson number (Ri_{12}) for each experiment are also shown. (a, b) May : Profiles collected at cross section X-2, (a) at 20:00 h on 26 May 2011, and (b) at 14:00 h on 27 May 2011. (c, d) Jul : Profiles collected at cross section X-4, (c) at 20:00 h on 22 July 2010, and (d) at 13:00 h on 23 July 2010. (e, f) Sep : Profiles collected at cross section X-5, (e)	

at 20:00 h on 10 Sept 2009, and (f) at 11:00 h on 11 Sept 2009. Note that conc. in (a-d) is in logarithmic scale. 23

Fig. 1.6. Gravity current profiles in the plunge zone at one transect measured between the inlet and X-1: (a-d) May, and (e-h) Sep. (a, e) Normalized field measured east-west velocity profile laterally averaged across the transect, compared with the fitted curves for the subcritical (subcrit.) and supercritical (supercrit.) regimens defined by Sequeiros (2012). (b, f) Normalized field measured tracer concentration profile. (c, g) Normalized field measured temperature profile. (d, h) Normalized field measured density excess profile, compared with the fitted curves for the subcritical and supercritical regimens defined by Sequeiros (2012). We have included the average values of the variables at the gravity current: velocity (U), tracer concentration (C), temperature (T), density excess (ΔP), and thickness (h). 28

Fig. 1.7. Possible behaviors of a cold plunging inflow (ρ_0) into a two-layered stratified system with a density step ($\rho_2 - \rho_1$) at the base of a warm constant temperature surface mixed layer (SML) with a linearly stratified metalimnetic layer underneath: (a) interflow (b) underflow, and (c) split flow, where ρ_G is the density of the current at the base of the SML. 31

Fig. 1.8. Estimation of the fractions of river buoyancy flux that penetrates the density step (b_2), from gravity current profiles at one transect measured close to X-1: (a, b) May, (c, d) Jul, and (e, f) Sep. (a, c, e) Portion of the river buoyancy flux that penetrates the density step (b_2), as a function of height (z). (b, d, f) Portion of the river buoyancy flux that penetrates the density step (b_2), as a function of the density excess ($\Delta\rho$). We mark the density step at the base of the SML ($\Delta\rho_{12}$) for each experiment. 33

Fig. 1.9. Seasonal estimations of transition Richardson number (Ri_{12}) and its controlling factors, using daily data of 2011 at site-M. In all panels, the shadow region corresponds to the sub-period of maximum stratification. (a) Estimations of Ri_{12} . We include the values of Ri_{12} for the days of the tracer experiments (black dots) according to daily records, independently of the year of the release. (b) Density changes at the base of the SML ($\rho_2 - \rho_1$), and inflow-SML density differences ($\rho_0 - \rho_1$). (c) Total dilution (Γ). (d) Initial dilution (Γ_I), and gravity current dilution (Γ_E). (e) Inflow Froude number (Fr_0). (f) Thickness of the surface mixed layer (D), as the daily maximum from hourly estimates with $\Delta T_{0z} = 0.2^\circ\text{C}$. (g) Ratio of nominal intrusion depth to surface mixed layer thickness, [NID : D]. 35

Fig. 1.10. Seasonal evolution of reservoir specific conductance (SC) at site-M in years (a) 2009, (b) 2010, and (c) 2011. Intrusion depths (white dots) are estimated as the average depth where the lake SC equals the SC at the intrusion (SC_m). The former is calculated as $SC_m = SC_1 (\Gamma - 1) + SC_0$, where the subscripts indicate whether the SC is measured at the inflow (0), lake surface (1), and intrusion (m), and Γ is the total dilution at the plunge zone and buoyancy-dominated region. 36

Fig. 2.1. Behavior of a 2D-gravity current of average density ρ_G in a two-layered stratified environment, ρ_1 and ρ_2 . (a) Interflows occur when $\rho_1 < \rho_G < \rho_2$. (b) Underflows occur if $\rho_G > \rho_2$. (c) Split flows form if the gravity current has significant internal density gradients. 42

Fig. 2.2. Summary of field and laboratory observations of gravity current profiles: velocity (2a and 2b) and density excess (2c and 2d). Data has been normalized by the average thickness of the gravity currents (h), and by maximum values of velocity and density excess (U_{max} and $\Delta\rho^*$).

Subcritical flows ($Fr < 1$) are shown in 2a and 2c, and supercritical flows ($Fr > 1$) in 2b and 2d.
 44

Fig. 2.3. Gravity current entering a two-layered stratified system. (a) Definition of variables in the water body. (b) Velocity $u_G(z)$ and density excess $\Delta\rho(z)$ profiles of the gravity current. The profiles were measured at S_N , before the gravity current reaches the density step $\Delta\rho_{12}$ located at S_{12} . We mark the average variables of the current ($h, U, \Delta P$), and the maximum value of $\Delta\rho(z)$ as $\Delta\rho^*$ 46

Fig. 2.4. (a) Experimental estimation of buoyancy flux portions at the interflow and the underflow (b_1 and b_2 , respectively) when the gravity current splits due to a density step ($\Delta\rho_{12}$), from the observed initial and final density profiles in the ambient water ($\rho_{int}(y)$ and $\rho_{obs}(y)$, respectively). (b) Density excess profile of the gravity current, $\Delta\rho(z)$. We mark the maximum value, $\Delta\rho^*$. (c) Velocity profile of the gravity current, $u_G(z)$. (d) Predictions of b_1 and b_2 as a function of height, z_i . (e) Predictions of b_1 and b_2 as a function of the density Richardson number, Ri_ρ . We mark the critical value, Ri_ρ^* 48

Fig. 2.5. (a) Hypothetical velocity profiles of two gravity currents with different regime: subcritical (gray) and supercritical (black), and (b) the corresponding hypothetical density excess profiles, where the maximum value is $\Delta\rho^*$. (c) Predictions of buoyancy flux portions at the interflow and underflow (b_1 and b_2 , respectively) when the hypothetical gravity currents split at a density step, as a function of the density Richardson number (Ri_ρ). We mark the critical value, Ri_ρ^* 50

Fig. 2.6. (a) Schematic layout of the experimental setup. The dashed rectangle in the main tank marks the study region to obtain the time slices series. The MSCTI is shown at the two locations where it was placed during the experiments. (b) Releasing mechanism in A-runs (subcritical regime, $Fr < 1$). (c) Releasing mechanism in B-runs (supercritical regime, $Fr > 1$) 51

Fig. 2.7. Photographs of the central 1 m-length section of the tank (Fig. 2.6a) during different runs with supercritical regime. Photo (a) was taken after 0.5 min of injection and (b-d) after 7 min. We observe the actual splitting of the gravity current in (a), interflow in (b), underflow in (c) and split flow in (d). The dashed lines mark the predominant pathways of the gravity current.
 55

Fig. 2.8. Time slices series during different experiments (Table 2.2). The dashed line marks 7 min after the beginning of the injection 57

Fig. 2.9. Ambient water density profiles before the gravity current injection (ρ_{int}) and after ca. 7 min since the beginning of the injection (ρ_{obs}), gathered with the MSTCI at $x = 1.5$ m in the experimental tank (Fig. 2.6a) during different experiments (Table 2.2). 57

Fig. 2.10. Experimental profiles of the two gravity currents, with subcritical ($Fr < 1$, a-c) and supercritical ($Fr > 1$, d-f) regimes. All profiles are referred to the S - z reference system and measured at S_N (Fig. 2.6a). The average values of thickness, velocity and density excess ($h, U, \Delta P$) are shown above. Error bars mark the standard deviation of the observed variables over the study period. (a, d) Velocity profile, $u_G(z)$. (b, e) Density excess profile, $\Delta\rho(z)$. The red points are an extrapolation of the profile in order to conserve the inflow buoyancy flux per unit width. (c, f) Gradient Richardson number (Ri_g) where the dashed line marks the critical value, $Ri_g = 0.25$, and the shaded rectangle marks interface layer at the top of the current. 58

Fig. 2.11. Predictions (lines) and experimental results (symbols) of buoyancy flux portions as a function of the density Richardson number (b versus Ri_ρ), from the experimental (a) subcritical gravity current ($Fr < 1$), and (b) supercritical gravity current ($Fr > 1$) entering the two-layered system (Fig. 2.10). The black dot marks the critical value of Ri_ρ^* and the thin dashed line marks the $Ri_\rho[0.5]$ for each regime. The shaded regions show the range of predicted values of b due to the error introduced by neglecting additional entrainment of ambient water before the gravity current reached the density step (Fig. 2.6a)..... 60

Fig. 2.12. Application results: predicted interflow buoyancy flux portions of the inflowing current (b_1) as a function of the density Richardson number (Ri_ρ) for different densimetric Froude numbers (Fr) of theoretical gravity currents [Sequeiros, 2012]. Values of b_1 along the white dashed line at $Ri_\rho = 20$ are commented in the text. We also mark with symbols (circles and triangles) the predicted portions of b_1 for the two gravity currents observed in our lab experiments. 62

Fig. 2A1. (a) Density excess profile of the gravity current, $\Delta\rho(z)$. We mark the maximum value, $\Delta\rho^*$. (b) Velocity profile of the gravity current, $u_G(z)$. (c) Predictions of the volume flux portions q_1 and q_2 as a function of height, z_i . (d) Predictions of q_1 and q_2 as a function of the density Richardson number, Ri_ρ . We mark the critical value Ri_ρ^* 66

Fig. 2A2. Experimental observations of interflow and underflow thickness, h_1 and $(h^* - h_1)$, for the two sets of runs: subcritical $Fr < 1$ (squares), and supercritical $Fr > 1$ (triangles). The dashed lines mark h^* for each regime. Black means interflow (1) and gray underflow (2) in all plots. . 67

Fig. 2A3. Predictions (lines) and experimental results (symbols) of volume flux portions as a function of the density Richardson number (q versus Ri_ρ) from experimental profiles of (a) subcritical gravity current ($Fr < 1$), and (b) the supercritical gravity current ($Fr > 1$) entering the two-layered stratified systems. The black dot marks Ri_ρ^* and the thin dashed line marks the $Ri_\rho[0.5]$ for each regime. 68

Fig. 3.1. Behavior of a 2D-gravity current of average density ρ_G in a two-layered stratified environment, ρ_1 and ρ_2 . (a) Interflows occur when $\rho_1 < \rho_G < \rho_2$. (b) Underflows occur if $\rho_G > \rho_2$. (c) Split flows form if the gravity current has significant internal density gradients. 72

Fig. 3.2. (a) Schematic layout of the experimental setup (not scaled). The vertical solid line ($x = 1.17$ m) marks the location where ambient density profiles were experimentally measured. The vertical dashed line at the slope ($S_N = 0.32$ m) marks the location where gravity current profiles were measured. The region inside the dashed rectangles is study in Fig. 3.10. (b) Theoretical velocity $u_G(z)$ and density excess $\Delta\rho(z)$ profiles of the gravity current measured at S_N . We mark the average variables of the current ($h, U, \Delta\rho$), and the maximum value of $\Delta\rho(z)$ as $\Delta\rho^*$ 74

Fig. 3.3. (a) Experimental estimation of buoyancy flux portions at the interflow and the underflow (b_1 and b_2 , respectively) when the gravity current splits due to a density step ($\Delta\rho_{12}$), from the observed initial and final density profiles in the ambient water ($\rho_{int}(y)$ and $\rho_{obs}(y)$, respectively). (b) Density excess profile of the gravity current, $\Delta\rho(z)$. We mark the maximum value, $\Delta\rho^*$. (c) Velocity profile of the gravity current, $u_G(z)$. (d) Predictions of b_1 and b_2 as a function of height, z_i . (e) Predictions of b_1 and b_2 as a function of the density Richardson number, Ri_ρ . We mark the critical value, Ri_ρ^* 78

Fig. 3.4. Computational domain depicting the dimensions and boundary conditions for the simulations corresponding to the experimental runs (Fig. 3.2a). Note that in the simulations the vertical coordinate k is referred to the tank surface and down-wards. 79

Fig. 3.5. Simulated, experimental and analytical (Sequeiros 2012) profiles of the two gravity currents gathered at the slope before the current hits the density step (S_N), with subcritical ($Fr < 1$, a,b) and supercritical ($Fr > 1$, c,d) regimes, where (a, c) are velocity profile, $u_G(z)$, and (b, d) density excess profile, $\Delta\rho(z)$. Error bars mark the standard deviation of the simulated profiles due to the point of measurement at the slope. 83

Fig. 3.6. Experimental (lab.) and simulated (sim.) ambient water density profiles before the gravity current injection (ρ_{int}) and after ca. 7 min since the beginning of the injection (ρ_{obs}), gathered at $x = 1.17$ m in the tank from the beginning of the ramp (Fig. 3.2a) during the experiments mark in bold in Table 3.2. Maximum standard deviations in the simulated profiles (due to the point of measurement in the tank) are marked in the lower right corner of the graph with horizontal bars. Values of the normalized $RMSE$ ($nRMSE$) are also included in each subplot. 85

Fig. 3.7. Simulated spatial distribution of the tracer concentration (conc.) in the tank after 7 min of injection of the two experimental gravity currents (a,c) subcritical, and (b,d) supercritical, into a stratified system with different density step (a,b) $Ri_\rho \sim 42$, and (c, d) $Ri_\rho \sim 7$ 85

Fig. 3.8. Laboratory (a, b) and simulated (c, d) buoyancy flux portions as a function of the density Richardson number (b versus Ri_ρ) for the two types of gravity current: (a, c) subcritical gravity current ($Fr < 1$), and (b, d) supercritical gravity current ($Fr > 1$). Portions from current profiles are marked with lines, while portions from density changes in the tank are represented by symbols. The black dot marks the critical value of Ri_ρ^* and the thin dashed line marks the $Ri_\rho[0.5]$ for each regime. The shaded regions show the range of predicted values of b due to the error introduced by neglecting additional entrainment of ambient water before the gravity current reached the density step (Fig. 3.2a). Vertical lines represent the maximum standard deviation in the portion values due to errors association to the measurements point of the density changes in the tank. 86

Fig. 3.9. Simulated spatial distribution of the two pulses of different tracer concentrations (C_1 and C_2) in the tank after 3 min release of the two experimental gravity currents (a,c) subcritical, and (b,d) supercritical, into a stratified system with a density step $Ri_\rho \sim 20$. Concentration of the tracer injected at the top of the current (C_1) is shown in a,b, while concentration of the tracer injected at the bottom of the current (C_2) is shown in c,d. 88

Fig. 3.10. (a-d) Downstream variation of (a,b) velocity $u_G(z)$, and (c,d) density excess $\Delta\rho(z)$ gravity current profiles along the x-direction, for the two extreme regimes study: (a,c) $Fr = 0.61$ (subcritical) and (b,d) $Fr = 1.22$ (supercritical). We mark the average current thickness, h . (e-l) Spatial variation of average properties: (e,f) average velocity, U ; (g,h) average density excess, ΔP ; (i,j) densimetric Froude number, Fr ; (k,l) entrainment coefficient, E . Different colors and symbols correspond to experiments with different density strength (Ri_ρ). We mark properties before (subscript b) and after (subscript a), the density step at S_{12} , which is represented by the red dashed line. Black dashed-dotted lines are discussed in the text. 95

Fig. 3.11. (a) Theoretical prediction of buoyancy flux portions flowing as interflow (b_1) and underflow (b_2) of five current regimes studied through simulations. (b-e) Normalized changes of

different variables across the density step against the stratification strength, Ri_ρ , for different current regimes, Fr : (b) changes of average velocity dU_{ba}/U , (c) changes of average density excess $d\Delta P_{ba}/\Delta P$, (d) changes of the densimetric Froude number $\Delta Fr_{ba}/Fr$, and (e) changes of the entrainment coefficient $\Delta E_{ba}/E$. Color dashed lines in (b) and (c) were used to estimate Eqs. 3.11 and 3.12. Black dashed-dotted lines in (d) and (e) are used in the discussion of the results. 97

Fig. 3.12. Energy budgets. (a-b) Time-series of: (a) the rate of change of the background potential energy ($\Phi_b = \Delta PE_b / \Delta t$), and (b) dissipation ε , during the injection of different current regimes (Fr) into a two-layered system with similar $Ri_\rho \sim 20$. (c) Mixing efficiency by the end of the injection for different current regimes (Fr) and density steps (Ri_ρ). 100

LIST OF TABLES

Table 1.1. Specifications of each injection during the three tracer experiments. The injections in bold are described in the results.	14
Table 1.2. Specifications of the instruments used during the tracer experiments and seasonal monitoring at Lake Bézinar.	15
Table 1.3. Stratification and hydraulic characteristics during the three tracer experiments.	19
Table 1.4. Field observations and theoretical estimates of intrusion depth, intrusion thickness, and initial dilution for each tracer experiment. We include the values of the variables required in our theoretical estimates using Fischer’s model and different approaches.	27
Table 1.5. Characteristic values of the gravity current observed at transect X-1 (i.e., buoyancy-dominated region) during the three tracer experiments.	29
Table 2.1. Dimensions and initial conditions in the tank, and constant inflow conditions of the experimental two-dimensional gravity currents.	52
Table 2.2. Experimental specifications of A- (subcritical, $Fr < 1$) and B- (supercritical, $Fr > 1$) runs (Fig. 2.6b, 2.6c). Ambient water density profiles were measured only in the runs marked in bold. Photos were taken in all runs.	53
Table 3.1. Tank dimensions and constant inflow conditions of the two-dimensional gravity currents created in the laboratory and simulated in this work.	73
Table 3.2. Specifications of the experimental A- (subcritical, $Fr < 1$) and B- (supercritical, $Fr > 1$) runs. We mark in bold the runs whose results are shown in Fig. 3.6.	76
Table 3.3. Average gravity current properties from laboratory experiments and simulations results for the two current regimes (subcritical $Fr < 1$, and supercritical $Fr > 1$). We use the same values as in the simulations to dimensionalize analytical profiles by Sequeros (2012). ..	84
Table 3.4. Results of buoyancy flux portions at the inflow (b_1), average gravity current properties (h , U , ΔP), and $RMSE$ from vertical profiles of two reference runs (A13 and B29, mark in bold) and a new sets of runs (a-d) to evaluate the parametric uncertainty of model results.	89
Table 3.5. Results of buoyancy flux portions at the inflow (b_1), average gravity current properties (h , U , ΔP), and errors ($RMSE$) from a new sets of runs (reference in Fig. 3.6) to evaluate the uncertainty of model results due to vertical resolution of inflow configuration.	92

LIST OF SYMBOLS

The following symbols are used in this PhD thesis:

B_G	Total buoyancy flux per unit width in the gravity current	$\text{m}^3 \text{s}^{-3}$
B_s	Buoyancy flux through the free surface	W kg^{-1}
B_0	Inflow buoyancy flux per unit width ($= g'_0 Q_0 / W$)	$\text{m}^3 \text{s}^{-3}$
B_2 and B_1	Buoyancy flux per unit width that becomes an underflow/interflow	$\text{m}^3 \text{s}^{-3}$
C	Concentration. Subscripts indicate location of measurement. No subscript means average value at the current	$\mu\text{g L}^{-1}$
C_D	Drag coefficient	-
C_κ	Von Karman constant ($= 0.41$)	-
C_p	Specific heat of water	$\text{J kg}^{-1} \text{ }^\circ\text{C}^{-1}$
D	Thickness of the surface mixed layer SML	m
D_k	Depth of each simulated domain column	m
E	Entrainment coefficient	-
Fr	Densimetric Froude number (at the current)	-
F_q	Mechanical energy flux	$\text{m}^3 \text{s}^{-3}$
Fr_0	Inflow Froude number	-
G'	Average reduced gravity at the current	m s^{-2}
H	Vertical distance from the initial depth of the gravity current to the density step	m
H_s	Sensible heat fluxes through the free surface	W m^{-2}
H^*	Effective surface heat flux into the diurnal mixed layer	W m^{-2}
K	Molecular diffusivity	$\text{m}^2 \text{s}^{-1}$
K_t	Eddy diffusivity	$\text{m}^2 \text{s}^{-1}$
L	Total length of the tank	m
L_c	Advective length scale	m
L_H	Latent heat fluxes through the free surface	W m^{-2}
L_N	Lake number	-
LW_{in} and LW_{out}	Incoming and emitted long-wave radiation	W m^{-2}
M and J	Coefficients of linear relationships to characterize the partition process	-
N^2	Buoyancy frequency	s^{-2}
PE	Total potential energy	J
PE_a	Available potential energy	J
PE_b	Background potential energy	J
Pr_t	Turbulent Prandtl number	-
Q	Flow rate	$\text{m}^3 \text{s}^{-1}$
Q_G	Volume flux of the current	$\text{m}^3 \text{s}^{-1}$
Q_1 and Q_2	Volume fluxes at the interflow and underflow	$\text{m}^3 \text{s}^{-1}$

List of Symbols

Re	Reynolds number	-
RH	Relative humidity	%
Ri_g	Gradient Richardson number	-
Ri_ρ	Density Richardson number, with critical value Ri_ρ^*	-
Ri_{12}	Transition Richardson number. Ri_{12c} is the critical value	-
S	Down-slope coordinate	m
SC	Specific conductance	$\mu\text{S cm}^{-1}$
SR	Solar radiation	W m^{-2}
S_H	Net surface heat fluxes into the lake, excluding short-wave radiation	W m^{-2}
T	Temperature. Subscripts indicate location of measurement. No subscript means average value at the current	$^\circ\text{C}$
U	Current velocity. Subscripts indicate location of measurement. No subscript means average value at the current	m s^{-1}
V	Volume of the reservoir	m^3
W	Width. Subscripts indicate location of measurement.	m
W_N	Wedderburn number	-
WD	Wind direction	$^\circ$
WS	Wind speed	m s^{-1}
Y	Total depth of water in the tank	m
b_1 and b_2	Portions of the inflow buoyancy flux flowing along the density step (base of SML) or along the bottom	-
$d\Delta P_{ba}/\Delta P$	Normalized change in the average current density excess across the density step	-
$d\Delta U_{ba}/U$	Normalized change in the average current velocity across the density step	-
g	Acceleration of gravity	m s^{-2}
g'	Reduced gravity. Subscripts indicate location of measurement.	m s^{-2}
g'_{12}	Reduced gravity of the ambient water density step ($=g \Delta\rho_{12}/\rho_1$)	m s^{-2}
h	Current thickness. Subscripts indicate location of measurement. No subscript means average value at the current	m
h^*	Thickness of the interflow when there is no underflow	m
k	Flow depth $k (= y - Y)$ referred to the tank surface	m
l	Tank dimensions	m
n	Number of grid cells a specific direction (see subscripts)	-
$nRMSE$	Normalized root mean square error	%
q	Volume flux per unit width ($= Q / W$)	$\text{m}^2 \text{s}^{-1}$
q_t	Velocity scale for the turbulent motions	m s^{-1}
q_1 and q_2	Volume flux portions at the interflow and underflow	-
t	Time	s
$u_G(z)$	Gravity current velocity profile	m s^{-1}
u_τ	Bottom shear friction velocity	m s^{-1}
u_1	Current velocity at the first grid point above the bottom boundary	m s^{-1}
u^*	Shear velocity	m s^{-1}

w^*	Convection velocity	m s^{-1}
x	Horizontal coordinate	m
y	Vertical coordinate, upwards from the horizontal bottom	m
z	Vertical coordinate, upwards from the down-slope bottom	m
z_i	Height within the gravity current profile where its density excess equals to the ambient density step, $\Delta\rho(z_i) = \Delta\rho_{12}$	m
Γ	Total dilution	-
Γ_E	Gravity current dilution	-
Γ_I	Initial dilution	-
$\Delta E_{ba}/E$	Normalized change in the entrainment coefficient across the density step	-
$\Delta Fr_{ba}/Fr$	Normalized change in the densimetric Fr across the density step	-
ΔP	Average density excess of the gravity current ($= \rho_G - \rho_1$)	kg m^{-3}
ΔS_{0i}	Distance from the inflow to the intrusion depth	m
ΔT_{0z}	Temperature difference from the surface to the base of the SML	$^{\circ}\text{C}$
Δt	Time interval between the initial and final ambient density profiles	s
$\Delta\rho(z)$	Gravity current density excess profile ($= \rho(z) - \rho_1$). Maximum value (bottom) as $\Delta\rho^*$	kg m^{-3}
$\Delta\rho_{12}$	Density step ($= \rho_2 - \rho_1$)	kg m^{-3}
Φ_b	Rate of change of the background potential energy ($= \Delta PE_b/\Delta t$)	$\text{m}^3 \text{s}^{-3}$
α and β	Constants of correction of the turbulent viscosity	-
α_T	Coefficient of thermal expansion	$^{\circ}\text{C}^{-1}$
α_{12}	Sharpness of the interface	-
δ	Half-divergence angle of the inflowing plume	$^{\circ}$
δ_{12}	Interface thickness between the two layers	M
ε	Viscous dissipation	$\text{m}^3 \text{s}^{-3}$
η	Mixing efficiency	-
η_k	Kolmogorov microscale	m
θ	Bottom slope angle	$^{\circ}$
ν	Molecular viscosity	$\text{m}^2 \text{s}^{-1}$
ν_t	Turbulent viscosity	$\text{m}^2 \text{s}^{-1}$
ρ	Densities. Subscripts indicate location of measurement	kg m^{-3}
ρ_G	Average gravity current density	kg m^{-3}
$\rho_{int}(y)$, and $\rho_{obs}(y)$,	Density profiles collected in the tank before, and after the injection of a given gravity current	kg m^{-3}
τ	Surface wind shear stress	N m^{-2}
φ	Intrusion thickness	m

The following subscripts are used in this PhD thesis:

a	After the density step
b	Before the density step
c	Coarse vertical resolution of the simulated domain
d	Medium vertical resolution of the simulated domain
f	Fine vertical resolution of the simulated domain
i, j, k	Longitudinal, lateral and vertical direction
m	Intrusion
w	water
0	Inflow or initial
1	Lake surface or SML
2	Metelimnetic or bottom layer

The following acronyms are used in this PhD thesis:

ADCP	Acoustic Doppler Current Profiler
CTD	Conductivity, temperature, and depth profiler
FDA	Fluorescein
LES	Large-eddy simulation
NID	Nominal intrusion depth
PAR	Photosynthetically active radiation
RANS	Reynolds-averaged Navier-Stokes
RWT	Rhodamine water tracing
SML	Surface mixed layer
TID	Theoretical intrusion depth
Jul	Field tracer release experiment undertaken in July 2010
May	Field tracer release experiment undertaken in May 2011
Sep	Field tracer release experiment undertaken in September 2009
m.a.s.l.	Meters above sea level
wse	Water surface elevation
2D	Two-dimensional
3D	Three-dimensional

GENERAL INTRODUCTION AND OBJECTIVES

Gravity currents into lakes, reservoirs, and the ocean have been shown to influence the vertical distribution of salinity (Dallimore et al. 2001; Legg et al. 2009; Wobus et al. 2013), suspended solids (Rimoldi et al. 1996; De Cesare et al. 2006), inorganic pollutants (Morillo et al. 2008), and biochemical material such as nutrients, dissolved oxygen, and biomass (Fischer and Smith 1983; Brookes et al. 2004; Botelho and Imberger 2007). The biochemical response of aquatic ecosystems can be significantly affected by the external input of cold water carrying dissolved or particulate matter. For instance, the growth of phytoplankton at the onset of stratification depletes the pool of nutrients at the surface layers, due to a strong thermocline that inhibits vertical distribution of nutrients from the hypolimnion to the surface layers. As a result, further development of phytoplankton will rely on either the recycling of living organisms, or the supply of new nutrients. The new nutrient loads, in turns, depend on vertical mixing processes that incorporate nutrients from the metalimnion to the surface layers, or external sources, such as gravity current inflows. Thus, nutrients carried by gravity currents entering stratified systems could fuel algal growth either when: (a) vertical mixing of deep persistent intrusion at season scales occurs (Jellison and Melack 1993; MacIntyre et al. 1999; Serra et al. 2007), or (b) when intrusions form close to the base of the surface mixed layer (SML) (Marti et al. 2011), which can be shortly entrained into the surfaces layers. Therefore, the contribution of gravity current to basin-scale vertical distribution of nutrients largely depends on the mixing processes with the ambient water and the depth where they intrude laterally in stratified water columns.

Incoming waters behave as negatively-buoyant gravity currents when their density is larger than the receiving water. The conceptual model traditionally accepted to describe the fate of gravity currents as they enter water systems is based on an extensive body of literature which includes laboratory experiments (Ellison and Turner 1959; Alavian et al. 1992; Hallworth et al. 1996), numerical simulations (Chung and Gu 1998; Bournet et al. 1999; Kassem et al. 2003), and the analysis of field data (Hebbert et al. 1979; Stevens et al. 1995; Dallimore et al. 2001). In this model, the gravity current push the quiescent ambient water until the momentum of the current is balanced by the buoyancy forces, due to the density differences between the current-ambient water. At

this point, the current plunges beneath the surface and flows along the bottom of the system as a gravity current, entraining ambient water as it flows down, until it reaches the depth of neutral buoyancy and intrudes laterally into the system. The dilution of the current occurs as a result of entrainment of ambient water into the plume both in the region of the plunge (initial dilution, Γ_I) and after the flow has assumed the form of a gravity current (gravity current dilution, Γ_E ; Fig. I.1). The rate at which ambient and inflowing water mix is a key factor in predicting the fate of gravity current water within a water body because it determines, together with the current-ambient density difference prior to the plunge zone, the depth of neutral buoyancy.

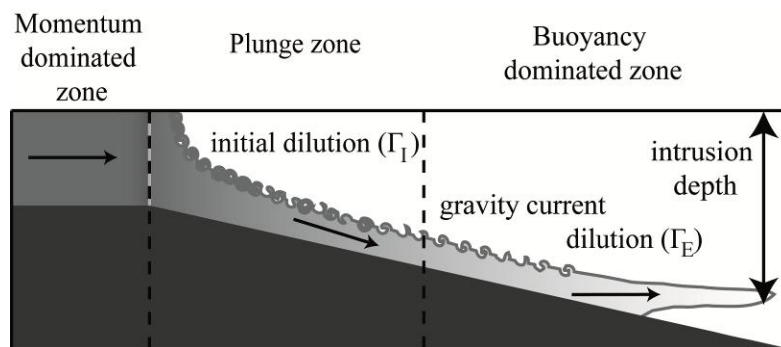


Fig. I.1. Conceptual model of a negatively-buoyant gravity currents entering a stratified system.

A large number of theoretical and experimental studies have been conducted to understand mixing in gravity currents and its interaction with ambient stratification in closed basins, forming a unique intrusion of limited thickness, centered at the depth of neutral buoyancy (Fischer et al. 1979; Wells and Nadarajah 2009). However, several observations suggest that this traditional framework may not be entirely satisfactory. Fischer and Smith (1983) conducted a series of tracer experiments in Lake Mead, and concluded that a significant fraction (10-20%) of river nutrients could be immediately available for primary production in the surface layers of the lake, well above the depth of neutral buoyancy. Recent laboratory experiments suggest that gravity currents in linearly density stratified environments not only entrain ambient water, but they also ‘detrain’ water from the current as they flow down-slope before they reach the depth of neutral buoyancy (Baines 2001). In many of those studies about gravity current mixing, the stratification in the basin has been approximated by two-layer stratification, with a well-mixed surface layer separated by a sharp density step from the deep denser waters (Monaghan et al. 1999; Samothrakis and Cotel 2006a,b; Wells and Wetlauffer 2007). When a gravity current enters such a two-layers stratification, two inflow behaviors have been widely study (Fischer et al., 1979): if the impinging current is lighter than the lower layer then an intrusion forms on the thermocline (Fig. I.2a, ‘interflow’); otherwise, it will intrude at the base of the basin (Fig. I.2b, ‘underflow’). However,

gravity currents can also split as they impinge into a density step to form two intrusions (Fig. I.2c) (Monaghan 2007). This behavior has been previously observed in laboratory experiments with vertical plumes (Kulkarni et al. 1993; Cotel and Breidenthal 1997) and turbidity currents (Rimoldi et al. 1996; Cesare et al. 2006). Wobus et al. (2013) showed with their numerical results the three inflow behaviors presented in Fig. I.2, and characterized them in terms of the increase in potential energy in the system. However, no indication was given of when splitting gravity currents should occur. Therefore, our current understanding of the pathways of cold river inflows in stratified lakes and reservoirs is far from complete (Rueda et al. 2007; Marti et al. 2011), in spite of its relevance to ecosystem function.

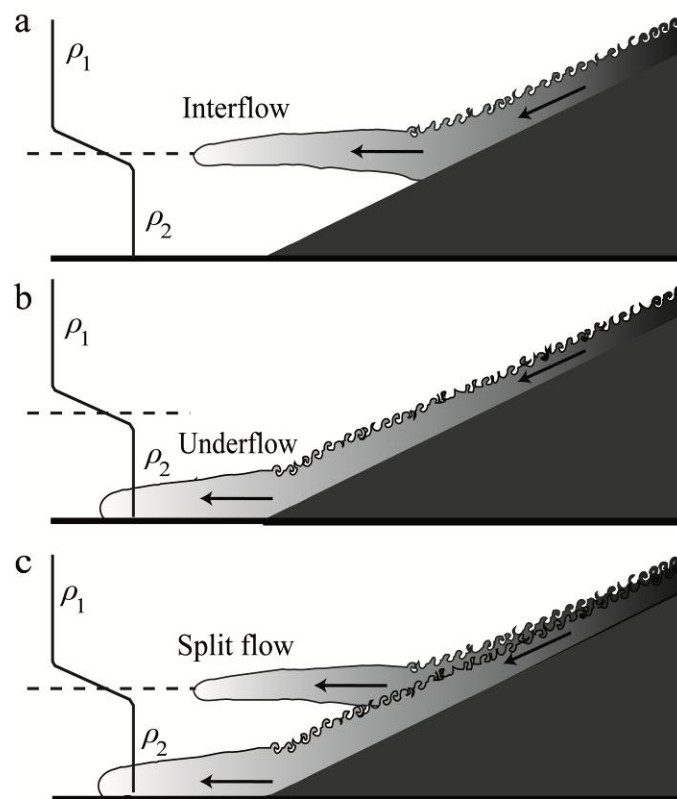


Fig. I.2. Behavior of a gravity current in a two-layered stratified environment, ρ_1 and ρ_2 : (a) interflows (b) underflows, and (c) split flows.

The main objective of this PhD thesis is to gain a better understanding of the vertical distribution of gravity currents into stratified systems. In particular, we demonstrate that a fraction of the inflowing gravity current can be retained at the base of the surface layers, entraining into the SML after vertical mixing. The biological significance of this behavior feature relies on the fact the nutrient loads dissolved in the gravity current water could be available for phytoplankton growth in the top layers of the stratified system at short time scales. Previous studies have already shown the

formation of near surface intrusions (De Cesare et al. 2006; Wobus et al. 2013), but the novelty of this research is the characterization of the factors controlling the portion of current flowing at the base of the SML, as well as the magnitude of this gravity current portion.

In this dissertation, the gravity current behavior in stratified systems has been study through field, laboratory and numerical experiments, and the results of these studies are presented in three chapters. Each chapter has been written as an independent article with its own introduction, methodology, results, discussion and conclusions; some of them having already been published and others in process of being submitted. The fact that they are written as individual articles means that some of the concepts can be repetitive for the reader but, on the other hand, each chapter can be read independently. The chapters are arranged in a logical order, starting with the observations in the field (Lake Béznar, Spain), followed by the laboratory experiments in two-layered systems, and finishing with numerical experiments to extend the conditions observed in the laboratory and in the field. The specific objectives of each chapter are summarized as follows:

- **Chapter 1** presents the results from three tracer release experiment in Lake Béznar (Spain) (Fig. I.3), which were used to characterize the fate of a cold plunging river into this Mediterranean reservoir under different stratification conditions. Field results demonstrated that a significant fraction of the inflow may be quickly entrained into the surface layers when intrusions near the base of the SML form (interflows or slipt flows). The interpretation of the current behavior in the field is largely based on the results obtained from the laboratory experiments shown in **Chapter 2**.

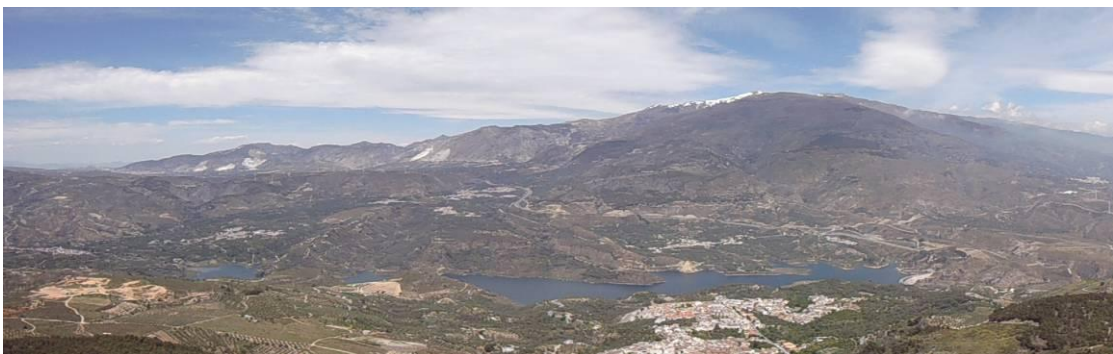


Fig. I.3. Aerial photograph of Lake Béznar (Spain).

- **Chapter 2** describes the results from laboratory experiments in two-layered stratified systems, which aimed at establishing the conditions that need to hold for the splitting of a gravity current at a density step. We also present and test a theory to quantify the portions of the current that go into each intrusion, based upon the internal gradients within the gravity current and the magnitude of the ambient density step.
- **Chapter 3** presents the numerical simulations to confirm and further extend the experimental current partition theory described in **Chapter 2**, as well as quantifying the effects of the impingement process on the gravity current internal structure and define the predominant forces (buoyancy vs. inertial) which control each gravity current regime.

In all, this PhD thesis aims to provide the reader with the required tools to: (1) characterize the fate of gravity currents water entering stratified water bodies, (2) identify the conditions that favor the formation of intrusions near the base of the surface layers, and (3) quantify the portion of the current which may be entrained into these top layers, in order to be able to assess the possible implications of different gravity current behaviors in aquatic ecosystems.

Chapter 1

PATHWAYS OF RIVER WATER TO THE SURFACE LAYERS OF STRATIFIED RESERVOIRS



This article is published in the Journal **Limnology and Oceanography** as:

Cortés, A., W. Fleenor, M.G. Wells, I. de Vicente, and F. Rueda (2014), Pathways of river water to the surface layers of stratified reservoirs. *Limnol. and Oceanogr.*, 59(1), 233-250, doi: 10.4319/lo.2014.59.1.0233

Abstract

This study uses tracer experiments to characterize the fate of a cold plunging river into a Mediterranean reservoir under different stratification conditions. Three tracer experiments in Lake Bézna (Spain) demonstrate that a significant fraction of the inflow may be quickly entrained into the surface mixed layer (SML), rather than flowing to lower depths. We observe that a fraction (and possibly all) of river inflow entrains into the SML when the gravity current forms intrusions at the top of the metalimnetic layer. Intrusions near the base of the SML form due to lighter interfacial fluid at the top of the gravity current with intermediate properties between river-reservoir water when there is sufficient dilution of the cold inflow, and abrupt density changes at the base of the SML. Consequently, a layer of fluid splits from the denser part of the current and intrudes just below the SML, while any remaining fluid flows to lower depths. We parameterize this splitting behavior in terms of the transition Richardson number, $Ri_{12} = \Gamma \times (\rho_2 - \rho_1) / (\rho_0 - \rho_1)$, where ρ_0 , ρ_1 , and ρ_2 are densities of the inflow, the SML and the metalimnetic layer underneath, respectively; and Γ is the total dilution through the plunge zone and subsequent entrainment. Splitting occurs when $Ri_{12} \geq 1$, consistent with previous laboratory experiments. We use this theory to predict the seasonal fate of river water during the stratification of Lake Bézna, and identify the conditions that favor the formation of intrusions near the base of the SML.

Introduction

River inflows, carrying large loads of nutrients, labile organic matter or particulates, represent one of the major drivers of the ecology of river valley reservoirs (Kennedy 1999), controlling the vertical distribution of light and nutrients, and hence, the abundance and composition of algal communities. The biogeochemical response of the ecosystem to inflows, largely depends on the pathways of distribution of river water in the lake, i.e., whether they form overflows or they become inserted within the water column to form intrusions. Nutrients or labile organic matter carried by positively buoyant inflows are introduced directly into the surface layers, and can be immediately available for phytoplankton or bacterial growth (Vincent et al. 1991). Negatively buoyant inflows, in contrast, can form metalimnetic intrusions (or lower) which could fuel algal growth on short time scales whether they occur above or below the compensation depth, where growth rates exceed respiration and loss rates. If they occur above the compensation depth, those intrusions will lead to the development of deep chlorophyll maxima. If they occur below, the fate of river-borne nutrients largely depends on the persistence of the intrusion. Nutrients and labile organic matter can be

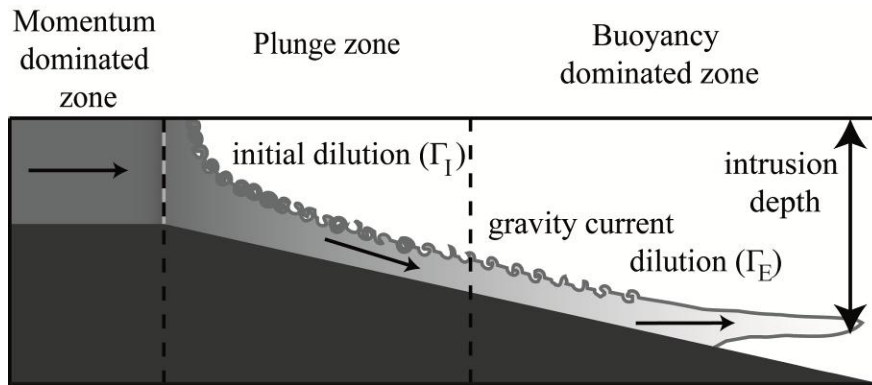


Fig. 1.1. Conceptual model of a cold plunging inflow entering a stratified reservoir.

adsorbed to particulates and settle to the hypolimnion, or they can be used by bacteria (Jellison and Melack 1993; MacIntyre et al. 1999; Serra et al. 2007) in deep persistent intrusions, which are only mixed vertically at seasonal scales as a result of deep convective mixing in winter or spring time. Alternatively, nutrients can be available for phytoplankton growth if the intrusions form close to the base of the surface mixed layer (SML), being readily mixed vertically and entrained in the SML within several days to months after the intrusion forms. Given that the time scales for the generation of intrusions are usually much faster than the vertical mixing time scales (Marti et al. 2011), the bioavailability of nutrients brought in by inflows is mostly determined by the vertical position of the intrusion. Therefore, to properly assess the biological response of reservoirs to river nutrient loadings, it is critical to understand the processes controlling the intrusion depth of cold river plumes in stratified water columns.

The conceptual model traditionally accepted by most limnologists to describe the fate of cold river plumes as they enter lakes and reservoirs is based on an extensive body of literature which includes laboratory experiments (Ellison and Turner 1959; Alavian et al. 1992; Hallworth et al. 1996) and numerical simulations (Chung and Gu 1998; Bournet et al. 1999; Kassem et al. 2003) conducted under simplified conditions. In this conceptual model, a negatively buoyant inflow will first push the quiescent lake (or ambient) water ahead of itself until buoyancy forces, due to the difference in density between reservoir and stream water, arrest the flow (Fig. 1.1). At this point, the river plunges beneath the surface, entraining ambient water as it sinks. Once submerged, the denser river water flows downward along the bottom as a gravity-driven current that gradually dilutes as a result of mixing with overlaying ambient water. Eventually, the gravity current will reach the depth of neutral buoyancy and intrude into the ambient water, or, if insufficient mixing occurs, it will reach the lake bottom (Stevens et al. 1995; Ahlfeld et al. 2003). The dilution of the denser inflowing water occurs as a result of entrainment of ambient water into the inflow both in the region of the plunge (initial dilution, Γ_I) and after the flow has assumed the form of a gravity current (gravity

current dilution, Γ_E ; Fig. 1.1). The intrusion depth after the initial and gravity current dilutions (theoretical intrusion depth) will be shallower than the depth estimated by presuming no mixing (nominal intrusion depth). The ‘nominal intrusion depth’ (NID) can be estimated by visually identifying the depth in the reservoir where water density is equal to the river water density. The ‘theoretical intrusion depth’ (TID) requires estimates of mixing in the plunge and subsequent gravity current. Therefore, the rate at which ambient and inflowing water mix is a key factor in predicting the fate of river water within the reservoir because it determines, together with the river-reservoir density difference prior to the plunge zone, the depth of neutral buoyancy.

In the traditional framework where density is controlled by temperature, the gravity current is implicitly assumed to be internally well mixed, so that a cold river entering a stratified reservoir with constant temperature gradients will form a unique intrusion of limited thickness, centered at the depth of neutral buoyancy (Fischer et al. 1979). However, several observations suggest that this model is not entirely satisfactory. Fischer and Smith (1983) conducted a series of tracer experiments in Lake Mead, and concluded that a significant fraction (10-20%) of river nutrients could be immediately available for primary production in the surface layers of the lake, well above the TID. As demonstrated by Baines (2001, 2005, 2008) in a series of experiments conducted under laboratory conditions, inflows entering linearly stratified bodies form continuous intrusions distributed throughout the water column above the TID. Baines (2001, 2005) argued that interfacial fluid may enter the water column (or detrain) from the gravity current at different levels before reaching the TID. Fernandez and Imberger (2008a,b) demonstrated, through experiments in large laboratory tanks, that inflows subject to dynamic density changes could cause the formation of layers of mixed inflow-ambient water above the TID. The formation of multiple intrusions has also been attributed to the existence of strong density gradients in the ambient water together with highly energetic inflows. De Cesare et al. (2006) reported the development of two intrusions in Lake Lugano during a flood event on the Cassarate River, when the river was highly loaded with suspended sediments, and the lake exhibited a strong thermocline. The shallowest intrusion formed by the turbidity gravity current was observed at the base of the surface mixed layer (SML). The deepest was formed at its theoretical intrusion depth. They attributed the formation of intrusions at the thermocline to what they referred to as ‘hydrodynamic effect’ of the turbidity current on the strong stratification existing in the lake at that time. Wells and Wettlaufer (2007) conducted a series of laboratory experiments with two-dimensional (2D) gravity currents entering a two-layered stratified system, and studied the conditions required for a gravity current to detach at a density step and form interflows along the base of the SML (Monaghan 2007). Those conditions were defined in terms of the initial buoyancy flux, the thickness of the top layer and the magnitude of the density step. Multiple intrusions might be expected to occur in natural, stratified lakes where the density

structure is known to exhibit complex patterns of vertically varying density gradients that evolve at seasonal and even shorter time scales. Therefore, our current understanding of the pathways of cold river inflows in stratified lakes and reservoirs is far from complete (Rueda et al. 2007; Marti et al. 2011), in spite of its relevance to ecosystem function.

Our general goal is to understand the pathways of negatively buoyant inflows in stratified Mediterranean reservoirs, characterized by thick and strongly stratified metalimnetic layers with seasonally varying strength. In particular, we demonstrate that a significant fraction of the cold plunging inflows can be incorporated into the SML within a few hours after entering the reservoir, as a result of the formation of intrusions near the base of the SML and the subsequent convective mixing of this top layer at night. We establish the conditions controlling the magnitude of these fluxes retained in the SML after inflow. In this work, we present and analyze field data collected in the course of three tracer experiments conducted in Lake Bézna, taken as a typical stratified Mediterranean reservoir, under different stratification conditions. This document is organized as follows: (1) we describe the methodology followed to characterize the short-term behavior of the river inflow in Bézna reservoir during the three experiments and the relevant theoretical concepts used in the analysis of the field data; (2) we present the field data showing the most relevant observations and interpret the data in the light of recently published results; and (3) we state the conclusions of this work.

Methods

Approach - A series of tracer experiments was conducted in Lake Bézna under different stratification conditions in fall 2009, summer 2010, and spring 2011. Fluorescent tracers were injected into the Izbor River, the largest inflow into the lake. Additional data were collected to support the interpretation of the experimental results. The field data allowed us to characterize the factors controlling the pathways of cold plunging inflow water from the river to the SML, which could make river-borne nutrients available for phytoplankton growth in the top layers at short time scales. We established the stratification, inflow conditions, and dilution values required for fluxes of river water to be incorporated into the surface layers of Mediterranean reservoirs.

Study site - Lake Bézna is a small mesotrophic reservoir located in southern Spain (Fig. 1.2a). The reservoir has an elongated shape oriented along the northwest-southeast direction (Fig. 1.2a), with a maximum depth of 83.7 m at the dam, maximum

length along the thalweg of nearly 4 km, and rather steep longitudinal slope (2-3%), similar to other reservoirs existing along the coast in southern Spain. When full, the volume of water held in the reservoir (V) is $54.6 \times 10^6 \text{ m}^3$, its surface area is $1.7 \times 10^6 \text{ m}^2$, and the elevation of the free surface is 486.2 m above sea level (m.a.s.l.). The average inflow (Q) that enters the reservoir is $1.8 \text{ m}^3 \text{ s}^{-1}$ with large seasonal variations. The largest inflow occurs at the northwest end from the Izbor River, which normally enters the reservoir perpendicular to the inflow section (i.e., as a free jet). This inflow accounts for 93% of the total flow into the reservoir. Two outlets exist at the dam, which are located at 411.2 m.a.s.l. (bottom outlet) and 453.2 m.a.s.l. (middle outlet), respectively. The lake is stratified from May to October. Stratification is characterized by the existence of a thick (ca. 25-30 m) metalimnion with temperatures that decrease almost linearly with depth; with surface temperatures that are usually warmer than the inflowing river water (Rueda et al. 2007); and develops, like other Mediterranean reservoirs, as a result of the strong insolation and the large volumes of water withdrawn during summer (Casamitjana et al. 2003; Vidal et al. 2007).

Tracer experiments - Three tracer experiments were conducted in Lake Béznar. The first was done in late summer to early fall, in September 2009, the second, in mid-summer during July 2010 under strongly stratified conditions, and the third in May

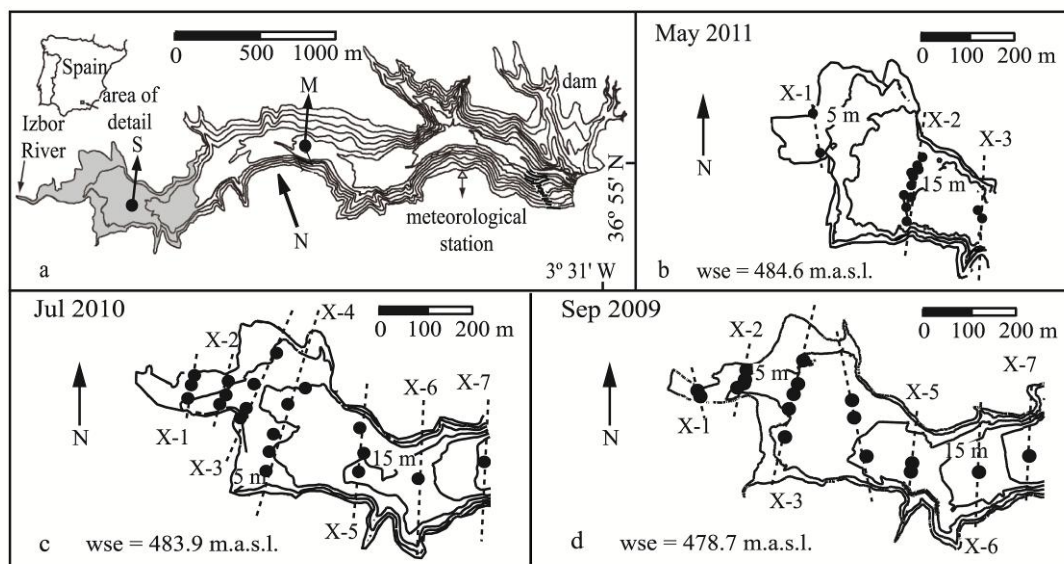


Fig. 1.2. (a) Lake Béznar bathymetry showing the location of the meteorological station and thermistor chains (M and S). Isobaths are represented every 10 m. The shaded area marks the sampling region during the tracer injections. (b, c, d) Cross-section locations during May, Jul, and Sep experiments, respectively.

Isobaths are represented every 5 m from the water surface at the given time. Water surface elevation (wse) is also included in meters above sea level (m.a.s.l.) for each experiment.

2011 under weakly stratified conditions typical of the early stages of the stratification development in the reservoir. Hereafter, we will refer to those experiments as Sep, Jul and May, without reference to the year. Furthermore, and to place our results in the context of the seasonal cycle, we will discuss first the experiment conducted in May early in the stratification cycle, followed by the results of the mid-summer (Jul) experiment at the time of maximum stratification, and ending with the description of the Sep experiment in late summer-early fall at the onset of the seasonal cooling. A fluorescent tracer, either Rhodamine water tracing (RWT) or fluorescein (FDA), was continuously injected through a 1 m diffuser bar in the Izbor River, 250-500 m upstream of the inlet, over a 3 h period. The length of the injection was set to minimize the variations of river and lake temperatures during the release period. The release period was, though, long enough so that the tracer distribution would reach steady-state conditions prior to the intrusion. Target tracer concentration in the river during the injections was established so that it did not exceed legal thresholds defined by environmental agencies. The injection date and times, the types of fluorescent tracer used, their target concentrations, and other details of the tracer experiments are shown in Table 1.1.

Fluorescent tracer concentrations were monitored using two calibrated Cyclops-7 fluorometers, manufactured by Turner Designs, connected to a C6 Multi-Sensor Platform (Table 1.2). Tracer concentration in the river was estimated from a series of samples collected downstream of the injection site during the injections, ca. 30 m upstream from the inflow section. The samples were collected every 15 minutes in Sep and every 30 minutes in the other two experiments. All samples were taken to the laboratory and diluted with distilled water to form samples with concentrations within

Table 1.1. Specifications of each injection during the three tracer experiments. The injections in bold are described in the results.

Tracer experiment	Date of injection	Starting injection time	Tracer	wse (m.a.s.l.)	Estimated flow ($\text{m}^3 \text{s}^{-1}$)	Target river tracer conc. ($\mu\text{g L}^{-1}$)
May 2011	26	16:00 h	Rhodamine WT	484.6	4.00	150
	27	08:30 h	Fluorescein	484.6	4.00	400
Jul 2010	22	16:30 h	Rhodamine WT	483.9	1.2	200
Sep 2009	10	16:30 h	Fluorescein	478.71	1.00	400
	11	11:30 h	Rhodamine WT	478.71	1.00	100

wse - water surface elevation, conc. – concentration

the range of measurement of the fluorometer. Tracer concentrations in the reservoir were monitored during the injections, and during the first day after the releases along three to seven transects. The transects were numbered starting from those closest to the inlet (Figs. 1.2b-d). From one to five fluorometer profiles were collected across each transect during the releases in Sep and Jul, and up to 25 profiles in May. The same fluorometer was used in the laboratory and the field to evaluate tracer concentrations.

Table 1.2. Specifications of the instruments used during the tracer experiments and seasonal monitoring at Lake Béznar.

Instrument	Model	Manufacture	Accuracy	Resolution	Other specifications
Acoustic Doppler current profiler (ADCP)	Workhorse	RD Instruments	0.3% water velocity	0.1 cm s ⁻¹	resolution of 5 cm in depth frequency of sampling: 1200 kHz
Conductivity, temperature and depth profiler (CTD)	SBE 19plus	Sea-Bird Electronics	<i>T</i> : 0.005°C <i>SC</i> : 5 μS cm ⁻¹	<i>T</i> : 0.0002°C <i>SC</i> : 0.5 μS cm ⁻¹	-
Conductivity logger	HOBO U24-002	Onset	<i>T</i> : 0.1°C <i>SC</i> : 50 μS cm ⁻¹	<i>T</i> : 0.01°C <i>SC</i> : 2 μS cm ⁻¹	-
Digital camera	D-60	Nikon	-	-	-
Fluorometer sensors	Cyclops-7	Turner Designs	5%	-	minimum detection limit: 0.01 μg L ⁻¹
Li-Cor PAR	LI-193SA	LI-COR Biosciences	-	-	sensitivity: 7 μA response time: 10 μS
Portable hand probe (<i>T</i> , <i>SC</i>)	EC-300	VWR International	<i>T</i> : 0.2°C <i>SC</i> : 5%	<i>T</i> : 0.1°C <i>SC</i> : 2.5%	-
Thermistor (<i>T</i>)	HOBO H20-001	Onset	<i>T</i> : 0.2°C	<i>T</i> : 0.02°C	sampling interval = 1 min. variable logging interval (10-30 min). response time = 5 min
<i>Meteorological station sensors</i>					
Air <i>T</i> and RH sensors	S-THA-M006	Onset	<i>T</i> : 0.7°C RH: 3%	<i>T</i> : 0.4°C RH: 0.5%	-
Silicon Pyranometer sensor (SR)	S-LIB-M003	Onset	10 W m ⁻²	1.25 W m ⁻²	-
Wind speed and direction sensors	S-WCA-M003	Onset	WS: 0.5 m s ⁻¹ WD: 5°	WS: 0.19 m s ⁻¹ WD: 1.4°	-

T – temperature, *SC* - specific conductance, PAR - photosynthetically active radiation, RH - relative humidity, SR - solar radiation, WS - wind speed, WD - wind direction.

Supporting information – Additional information was collected during the injections to aid in the interpretation of the tracer concentration data. Sequences of photographs of the inflow region were collected using a tripod-mounted D-60 digital camera deployed on a high point. High resolution water velocity profiles, with 5 cm bins, were also collected along several cross-sections in the lake, using a downward-looking 1200 kHz RD Instruments-Workhorse Acoustic Doppler Current Profiler (ADCP), configured to operate on pulse-to-pulse coherent mode 5. Temperature, specific conductance (*SC*), turbidity, and photosynthetically active radiation (PAR) data were collected along the sampling transects with a Seabird SBE-19plus conductivity, temperature, and depth (CTD) profiler with a vertical resolution of ~10 cm. The sampling points and times for the CTD profiles coincided with those of the fluorometer probe. In addition, two thermistor chains with HOBO H20-001 temperature loggers were deployed in Lake Béznar prior to each injection at two sites located 800 m and 1700 m from the inflow section, respectively (S- and M-sites, respectively, in Fig. 1.2a). The thermistors were programmed to sample every minute and record the average every 30 minutes, and were arranged every 1 m in the shallowest 30 m of the strings. The spacing between loggers increased up to 4.5 m below that depth.

Inflows and meteorological forcing - The inflow rates during the time of the injections were provided by the Regional Water Agency ('Agencia Andaluza del Agua', Granada, Spain), and measured using chemical gauging techniques (Herschly 2009). Inflow temperatures were monitored during the releases on Jul and Sep using HOBO H20-001 thermistors located 500 m upstream from the inlet and with a frequency of 30 minutes and 10 minutes, respectively. On May, *SC* was also monitored, using a HOBO U24-002 data logger. This sensor measured both variables every 30 minutes during the May injection ca. 500 m upstream from the inlet. Inflow *SC* during Sep was measured only once prior to the release and upstream of the injection site with a portable hand probe (VWR EC-300). This probe was also used during the other two experiments (May and Jul) to measure inflow temperature and *SC* with a frequency of 30 minutes. All temperature and *SC* sensors used during the experiments were recalibrated after the field campaigns, so the different measurements were comparable. Densities (ρ) were calculated as function of water temperatures (T), using the equation of state of Chen and Millero (1986), as reported by Pawlowicz (2008). The contribution of *SC* to density was neglected, given that it normally accounted for < 10% of the density differences between lake and river water. Therefore, *SC* is used only as a conservative tracer to test our conclusions on the fate of river water in the reservoir. Meteorological variables (wind speed and direction, air temperature, relative humidity, and solar radiation) were continuously measured and recorded every 30 minutes at a site near the dam (Fig. 1.2a). The specifications of all instruments used in the experiments are shown in Table 1.2.

Energy fluxes and mixing scales in the surface mixed layer – Estimates of the surface wind shear stress (τ), sensible heat (H_s), and latent heat (L_H) fluxes through the free surface were calculated, following the bulk-parameter method of Fairall et al. (1996), and accounted for the effects of atmospheric stability. Net surface heat fluxes (S_H) into the lake, excluding short-wave radiation, were estimated as function of L_H , H_s and the incoming and emitted long-wave radiation (LW_{in} and LW_{out}), as $S_H = LW_{in} - LW_{out} + L_H + H_s$. The buoyancy flux through the free surface (B_s) was derived from heat flux estimates, and calculated as (Wüest and Lorke 2003):

$$B_s = \frac{g \alpha_T H^*}{C_p \rho_w} \quad (1.1)$$

Here g is the acceleration of gravity, α_T is the coefficient of thermal expansion, C_p is the specific heat of water, ρ_w is water density, and H^* is the effective surface heat flux into the diurnal mixed layer, calculated as in MacIntyre et al. (2002). In these calculations the attenuation coefficient was set to 0.45 m^{-1} , as observed in the field. The penetrative convection velocity (w_*) was calculated from the surface buoyancy flux (B_s), as $w_* = (B_s D)^{1/3}$ (Wüest and Lorke 2003). The depth of the surface mixed layer SML (D) was determined from analysis of temperature profiles collected in the field as the depth where the water temperature difference from the surface (ΔT_{0z}) is 0.2°C (the logger accuracy, see Table 1.2). The mechanical energy flux (F_q) was derived from surface cooling and shear production in the wind surface layer and parameterized following MacIntyre et al. (2002), as $F_q = 0.5 (w_*^3 + C_N^3 u_*^3)$ where $C_N = 1.33$ (Imberger 1985), and $u_* = (\tau / \rho_w)^{1/2}$ the shear velocity. The velocity scale for the turbulent motions in the surface mixed layer were calculated as $q_t = F_q^{1/3}$.

Mixing and dilution calculations - The initial dilution (Γ_1) experienced by cold plunging flows entering as free jets in lakes was parameterized in terms of the inflow Froude number, $Fr_0 (= U_0 g'_0{}^{-1/2} h_0^{-1/2})$. Here, the inflow velocity is represented as U_0 , its depth as h_0 , and the reduced gravity, g'_0 , is calculated as $g(\rho_0 - \rho_1)/\rho_1$, in terms of the inflow and lake surface densities, ρ_0 and ρ_1 , respectively. Two alternative parameterizations were used for the initial dilution. First, we used the approach of Johnson et al. (1989), in which Γ_1 is assumed proportional to Fr_0 , with the constant of proportionality being $C = 3.6$ (i.e., $\Gamma_1 = 3.6 Fr_0$). We also used the parameterization of Fleenor (2001), in which Γ_1 depends on Fr_0 and the reservoir shoreline geometry, characterized in terms of the angle formed between the axis of the river channel and the reservoir shoreline at the inlet (the half-divergence angle of the inflowing plume, δ). Fleenor (2001) proposed the following expression to quantify the initial dilution:

$$\Gamma_1 = 0.223 Fr_0 + 0.008 \delta + 1 \quad (1.2)$$

Mixing in the buoyancy-dominated region between the gravity current and the overlying ambient water is quantified here using bulk entrainment rates (Ellison and Turner 1959; Turner 1986; Cenedese and Adduce 2010). Due to interfacial mixing, the average thickness of the gravity current (h) increases downslope (S) with a constant rate, so that the entrainment coefficient can be defined as $E = \Delta h / \Delta S$ (Ellison and Turner 1959). As a result, the gravity current dilution (Γ_E) can be expressed as:

$$\Gamma_E = \frac{\Delta h + h}{h} = E \frac{\Delta S}{h} + 1 \quad (1.3)$$

Note that we are assuming that the velocity is constant within the gravity current, which corresponds to normal conditions, to which downflows quickly asymptote (Fischer et al. 1979). The parameterization of Cenedese and Adduce (2010) was used to estimate the entrainment coefficient in gravity currents flowing downslope with a densimetric Froude number, $Fr (= U G^{r1/2} h^{-1/2})$, close to unity, as follows (*see* their figs. 2 and 3),

$$E = \frac{4 \times 10^{-5} + 3.4 \times 10^{-3} Fr^{7.18}}{1 + 3.4 \times 10^{-3} C_2 (Fr + 0.51)^{7.18}}, \quad \text{where } C_2 = 1 + \left(\frac{243.52}{Re^{7.18}} \right) \quad (1.4)$$

where Re is the Reynolds number, θ is the bottom slope angle, U is the average gravity current velocity, and reduced gravity is now defined in terms of local variables as $G' = g (\rho_G - \rho_1) / \rho_1$, where ρ_G and ρ_1 are the average gravity current and reservoir surface densities, respectively.

Results

Stratification and meteorological forcing - The reservoir was stratified during all three tracer experiments, with a warm SML above a linearly stratified metalimnion (Figs. 1.3a-c). The thickness and temperature of the SML (D and T_1), and the buoyancy frequency in the metalimnion (N^2) varied depending on the experiment (Table 1.3), consistent with the seasonal changes in stratification reported earlier (Vidal et al. 2007) for Lake Béznar. The shallowest SML was observed early in the stratification period (May), and the deepest, in late summer-early fall after the onset of the seasonal cooling (Sep). Temperatures in the SML peaked in mid-summer (Jul), at the time of maximum insolation. In all cases, the metalimnion extended from the base of the SML to the depth of the middle outlet, which remains open during the stratification period. Below the middle outlet, the water temperature remains uniform and almost steady (ca. 10°C) throughout the year. The thickness of the metalimnion is maximum at the start of the

Table 1.3. Stratification and hydraulic characteristics during the three tracer experiments.

Variable	Tracer experiment		
	May	Jul	Sep
Thickness of SML, D (m)	2	3 - 6	4 - 8
SML temperature, T_1 (°C)	21.5	27.2	25.9
Buoyancy frequency, N^2 (s ⁻²)	6.0×10^{-4}	11.0×10^{-4}	8.2×10^{-4}
Nominal intrusion depth, NID (m)	14	8.5	19
Inflow temperature, T_0 (°C)	16 ± 0.2	22.0 ± 1	21.0 ± 0.5
Inflow rate, Q_0 (m ³ s ⁻¹)	3.8 ± 0.3	1.2 ± 0.2	0.83 ± 0.1
Inflow width, W_0 (m)	13 ± 3	8 ± 2	5.3 ± 2
Inflow depth, h_0 (m)	0.75 ± 0.1	0.38 ± 0.05	0.36 ± 0.05
Inflow specific conductance, SC_0 ($\mu\text{S cm}^{-1}$)	352 ± 20	680 ± 25	620
Inflow tracer concentration, C_0 ($\mu\text{g L}^{-1}$)	132.5 ± 8	185.8 ± 14.2	422 ± 28
Half-divergence angle, δ (°)	45	90	90
Inflow Froude number, Fr_0	4.32	5.64	6.72

SML – surface mixed layer

stratification and decreases thereafter as a result of changes in the SML and deep withdrawals. At seasonal scales, the strongest gradients in the metalimnion are expected in mid-summer time (Jul) or in late summer-early fall (Sep), and the weakest occur early in the stratification period (May). This is consistent with the values of N^2 measured close to the inflow that we show in Table 1.3, and with the values calculated from thermistor chain data at site-M.

Very noticeable in Figs. 1.3a-c are the hourly changes exhibited by water temperatures in the metalimnion. These oscillations are associated with changes in wind forcing, which, before and during the experiments, exhibited strong diurnal periodicity, typical of land-sea breezes. Maximum wind speeds occurred during the afternoon (from 15:00 to 18:00 h), mostly from the southeast towards the inlet; lowest wind speed values, in turn, occurred during the night and early morning, when the wind direction reverses (Figs. 1.3d-f). The strongest winds (up to 7 m s^{-1}) were observed in Sep. By contrast, the May experiment was conducted under extremely calm conditions, with northwesterly winds up to 1.5 m s^{-1} in magnitude. The response of the water column to winds, at the scale of individual events, can be analyzed on the basis of values of Wedderburn (W_N) and Lake numbers (L_N). Small Lake numbers ($L_N < 1$) are associated with vertical mode 1 tilting of the temperature field and the upwelling of hypolimnetic water, whereas small Wedderburn numbers ($W_N \sim \text{O}[1]$ or $W_N < 1$) are associated with a higher vertical mode 2 response, in which the metalimnion compresses downwind and stretches upwind (Stevens and Imberger 1996). Before and during the tracer experiments, $L_N \gg 1$ and $W_N \approx > 1$; consequently, the response of the water column to wind forcing was largely characterized by oscillations in the thickness of the

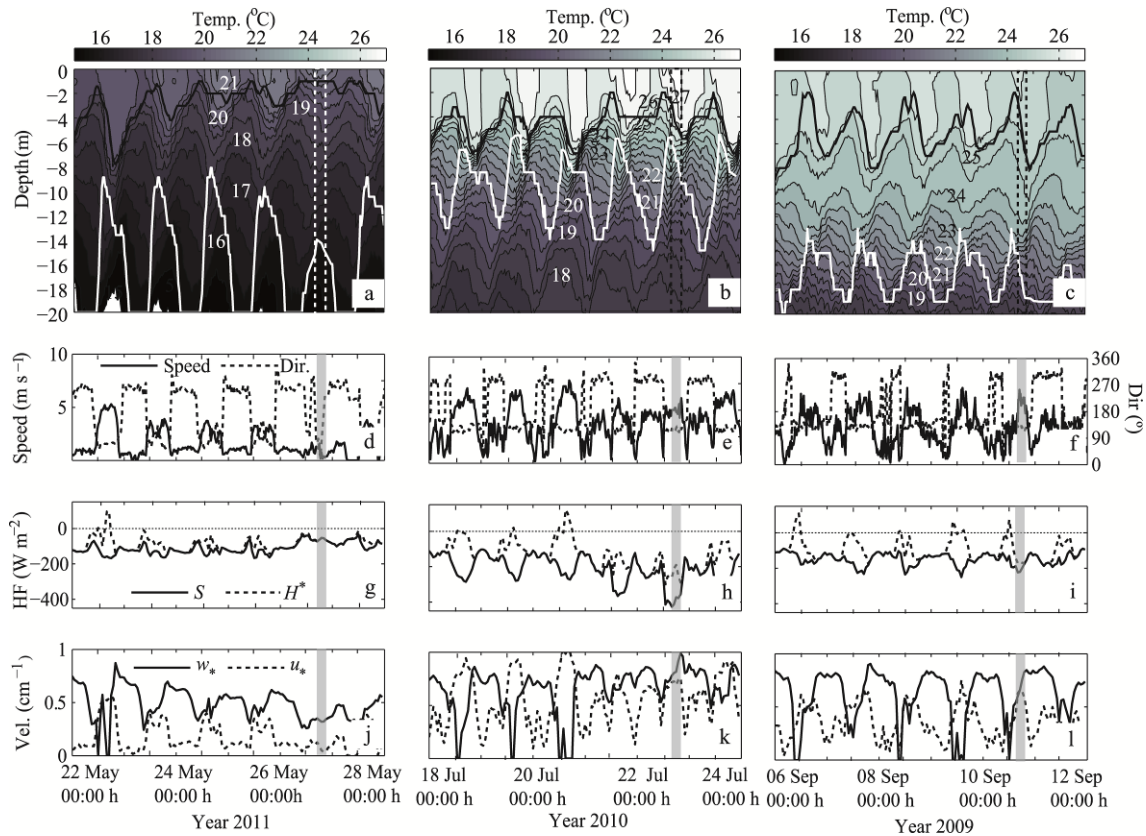


Fig. 1.3. Stratification, heat fluxes and meteorological forcing during the tracer experiments at Lake Bézinar. Each vertical set of Figs. correspond to May, Jul, and Sep experiments, respectively. The dashed and shadowed rectangles define the injection period (3 h). (a-c) Time series of reservoir temperature close to the inflow section (S – Fig. 1.2a), where the black line marks the depth of the surface mixed layer (SML) and the white line shows the nominal intrusion depth (NID). Isotherms are marked every 0.5°C . (d-f) Time series of wind speed (speed) and wind direction (dir.). (g-i) Heat fluxes (HF) at the surface of the reservoir (W m^{-2}): net surface heat flux omitting short wave radiation (S_H), and effective surface heat flux in the surface mixed layer (H^*). (j-l) Convective velocity (vel.) scale (w_*), and shear velocity scale (u_*) in cm s^{-1} .

metalimnion, as reported earlier by Vidal et al. (2007). The isotherms near the inlet compressed during the afternoon and evening in response to southeasterly winds, as depicted in Figs. 1.3a-c. Note that the thickness D and the temperature of the SML increase near the inlet during the afternoon as a result of warmer SML water being pushed downwind. The amplitudes of these wind-driven oscillations of D were up to 4 m in Sep (i.e., from 4 m to 8 m).

The changes in depth and temperature of the SML are also associated with heat fluxes into and from the reservoir via the atmosphere. Our estimates of those fluxes before and during the experiments are shown in Figs. 1.3g-i. Note that, the SML only gained heat around noon in Jul and Sep, when $H^* > 0$. During those experiments, heat losses (S_H) at night ranged from $200\text{--}400 \text{ W m}^{-2}$, two to four times larger than in May (50 W m^{-2}). The deepening of the SML in all cases was largely driven by night-time

convection ($w_* > u_*$, Figs. 1.3j-l), with a ratio of surface buoyancy flux to the total kinetic energy ($0.5 w_*^3 / F_q$) close to unity after the injection. The total mechanical energy flux (F_q) ranged between $30 \times 10^8 - 60 \times 10^8 \text{ m}^3 \text{ s}^{-3}$ in Jul and Sep, but it was almost one order of magnitude lower in May ($F_q = 10^8 \text{ m}^3 \text{ s}^{-3}$), which suggests that vertical mixing and SML deepening were weaker at that time.

Inflow conditions – In all experiments the river was negatively buoyant, forming cold plunging flows with a nominal intrusion depth (NID) that was always below the SML (Figs. 1.3a-c). Only in Jul, the NID was close to the base of the SML. Note in Figs. 1.3a-c the large fluctuations exhibited by the NID. These are partly due to the oscillations in the thermal structure near the inflow, but are also largely associated with hourly changes in the inflow temperatures. These changes can be up to 5-8°C over a day, depending on the time of the year, and maximum in mid-summer (July). During the releases, the lowest inflow temperatures and the most stable ($16.0 \pm 0.2^\circ\text{C}$) were recorded in May (Table 1.3). Maximum inflow temperatures and the largest variations as well, occurred in Jul ($22.0 \pm 1^\circ\text{C}$). The minimum inflow rates were recorded in Sep at the end of the dry summer season, while the maximum flow rates, largely attributed to snowmelt, were measured in May. Average inflow rates (Q_0), temperature (T_0), specific conductance (SC_0), and tracer concentration (C_0) during each injection are summarized in Table 1.3. The dimensions of the inlet channel (its width, W_0 , and depth, h_0) and the geometry of the shoreline near the inflow, characterized in terms of the half-divergence angle of the main river plume (δ), were estimated for each injection and are also shown in Table 1.3. Note that the inflow geometry varied considerably among injections. The half-divergence angle of the main plume was $\delta = 90^\circ$ (free-jet) in Jul and Sep, but $\delta = 45^\circ$ in May (Table 1.3; Figs. 1.4a,b for Sep). These changes in reservoir geometry were largely due to changes in the free surface elevation (Table 1.1, Figs. 1.2b-d). Also, a flood event in winter 2009 modified the inflow geometry, creating an elevated sand splay on the south margin.

Observed distribution of tracers and intrusions - Temperature and tracer concentration profiles collected towards the end of the injections, and one day after are shown in Fig. 1.5. The SML in May was only 2 m thick, overlying a metalimnion with the weakest stratification ($N^2 = 6.0 \times 10^{-4} \text{ s}^{-2}$) observed during the three experiments. The depth of the SML remained constant during the injection. The tracer concentration profiles collected at transect X-2 (Fig. 1.2b) at the end of the release show that a single, wide intrusion formed between the shallow SML and the NID (= 14 m), with peak tracer concentrations at ca. 6 m (Fig. 1.5a). The day after this injection the tracer remained confined in the metalimnion, and did not mix into the SML (Fig. 1.5b).

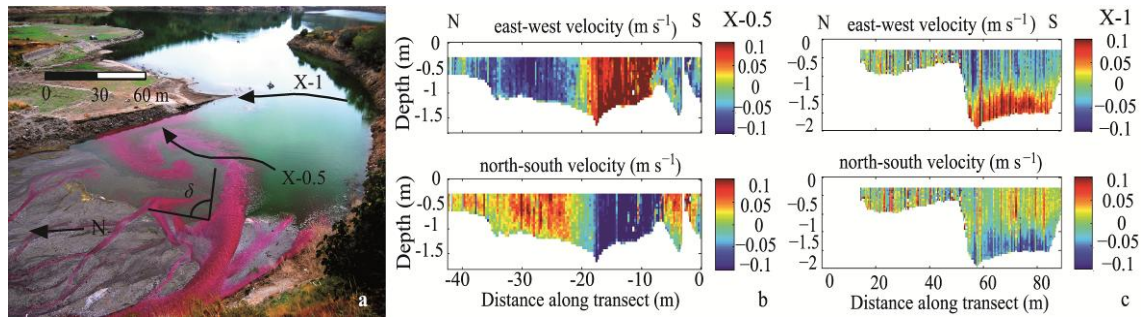


Fig. 1.4. Sep experiment data. (a) Geometry of the inflow basin and half-divergence angle of the main inflowing plume ($\delta = 90^\circ$). Transects X-0.5 and X-1 are also marked. (b) ADCP velocity east-west (top) and north-south (bottom) along transect X-0.5 (plunge zone). (c) ADCP velocity east-west (top) and north-south (bottom) in the buoyancy-dominated region, shortly after the plunge zone (X-1).

In contrast to May, cold river inflows formed intrusions at the base of the SML in Jul and Sep. In Jul, the metalimnion was strongly stratified ($N^2 = 1.1 \times 10^{-3} \text{ s}^{-2}$ at site X-4), and the depth of the SML varied from ca. $D = 3$ to 6 m during the release. A unique intrusion was observed at the end of the experiment at a depth of 6.5 m, near the base of the SML and ca. 2 m above the NID (Fig. 1.5c). One day after the Jul injection, the intrusion had already mixed into the SML, likely as a result of night-time convective mixing (Fig. 1.5d). The base of the SML in Sep was initially at 4 m below the surface, increasing up to 8 m at the end of the 3 h injection. The strength of the stratification in the metalimnion was intermediate between that of the other two experiments ($N^2 = 8.2 \times 10^{-4} \text{ s}^{-2}$). The tracer concentration profiles collected at site X-5 towards the end of Sep release reveal the existence of two intrusions: one at the base of the SML, and another one deeper at ca. 12 m (Fig. 1.5e). The morning after the injection, the deeper intrusion persisted, but the shallower intrusion had been entrained in the SML, also as a result of convective mixing during the night (Fig. 1.5f). The observed thickness of the intrusions at end of the injections ranged from 6.2 m in May to 4.8 m and 2.5-3 m in Jul and Sep injections, respectively (Table 1.4). The thickness of the intrusions, however, is not only the result of river temperature fluctuations during the injections. For example, inflow temperatures in May varied by only 0.2°C during the release. The intrusion, though, formed between two isotherms differing in temperature up to 2°C (Table 1.3; Fig. 1.5).

Discussion

Our field observations do not follow the expected behavior for a negatively buoyant inflow, as depicted in Fig. 1.1, and incorporated, for example, in the inflow

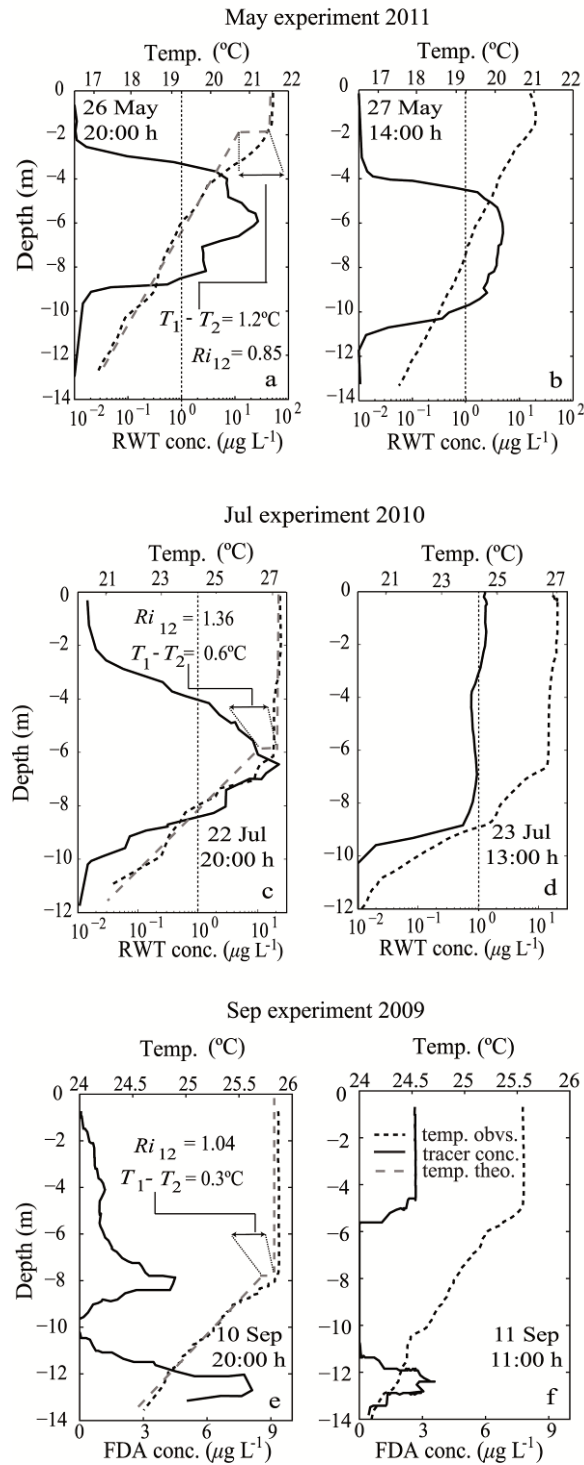


Fig. 1.5. Observed tracer concentration (tracer conc.) of Rhodamine WT (RWT) or fluorescein (FDA) and observed CTD-temperature profiles (temp. obs.) collected close to the inflow section during each tracer experiments. The associated theoretical temperature profile (temp. theo.) defines the density step at the base of the SML. The temperature step ($T_1 - T_2$) and the field value of the transition Richardson number (Ri_{12}) for each experiment are also shown. (a, b) **May**: Profiles collected at cross section X-2, (a) at 20:00 h on 26 May 2011, and (b) at 14:00 h on 27 May 2011. (c, d) **Jul**: Profiles collected at cross section X-4, (c) at 20:00 h on 22 July 2010, and (d) at 13:00 h on 23 July 2010. (e, f) **Sep**: Profiles collected at cross section X-5, (e) at 20:00 h on 10 Sept 2009, and (f) at 11:00 h on 11 Sept 2009. Note that conc. in (a-d) is in logarithmic scale.

mixing model described in Fischer et al. (1979) (p. 213-219). This is a steady-state model of gravity currents in a drowned river valley of prismatic section and predicts a unique intrusion of limited thickness (φ) centred at the TID, for a given inflow temperature T_0 and lake temperature profile. We will refer to this as Fischer's model. The intrusion thickness φ parameterization depends upon a non-dimensional number $R = q_m / (N^{1/3} L^{2/3} \nu^{2/3})$ (Fischer et al. 1979), where $q_m (= Q_m / W_m)$ is the volume flux per unit width of the intrusion, W_m is the width of the basin at the separation point, N and L are the buoyancy frequency and length of the reservoir at the intrusion depth, respectively, and ν the vertical viscosity ($\nu = 10^{-6} \text{ m}^2 \text{ s}^{-1}$). During all the releases, $R > 1$, and φ was calculated as,

$$\varphi = 2 \left(\frac{q_m}{N} \right)^{1/2} \quad (1.5)$$

Using temperature profiles taken at the end of the injection periods (Figs. 1.5a,c,e) and the range of T_0 recorded during the experiments, to account for the variability of the system (see *Results*), the values of the TIDs were in the range $12.1 \pm 0.28 \text{ m}$, $7.85 \pm 0.57 \text{ m}$, and $17.95 \pm 0.45 \text{ m}$ in May, Jul, and Sep, respectively (Table 1.4, 'Fischer literature' column). The model parameters in these calculations were taken from the literature. The bottom drag coefficient, for example, was set to 0.001 and all other geometry parameters for Lake Béznar were taken from Rueda et al. (2007). The initial dilution Γ_1 was set to 1.3, the average of the values reported for other lakes (see Rueda et al. 2007). The values of W_m in Eq. 1.5 were taken from the bathymetry maps (Fig. 1.2) at the observed intrusion depths. The theoretical intrusion thickness φ , accounting for the observed changes in T_0 within the release period, were $1.46 \pm 10^{-4} \text{ m}$, $0.62 \pm 0.01 \text{ m}$, and $0.66 \pm 0.01 \text{ m}$ in May, Jul and Sep, respectively (Table 1.4, 'Fischer literature' column). In general, the theoretical estimates of TID were well below the observed intrusions, identified as peaks in the tracer concentration profiles. The theoretical intrusion thicknesses (φ) were also, on average, 20% of the observed values. Furthermore, the development of two intrusions as observed in Sep (one at the base of the SML and another at the TID), rather than only one intrusion, cannot be explained with the conceptual model depicted in Fig. 1.1. This behavior has been reported in other stratified lakes, but mainly associated with turbidity flows, and it has not been interpreted in terms of density stratification and inflow conditions (De Cesare et al. 2006). The differences between observations and theoretical estimates can be due to the effects of internal waves or strong mixing rates between the gravity current and ambient water forming fluid with intermediate density and momentum between those of the lake and the river, which could detrain at different depths in the water column.

Total dilution – Temperature observations were used to estimate the total dilution Γ at the intrusion levels as,

$$\Gamma = \frac{(T_1 - T_0)}{(T_1 - T_m)} \quad (1.6)$$

Here the subscripts indicate whether the temperature is measured at the inflow (0), at the lake surface (1), or at the intrusion depth (m). We assume in Eq. 1.6 that all of the entrainment is from the lake surface. Using the average values of T_0 and T_1 from Table 1.3, and the observations collected at section X-2 (Fig 1.5a), Γ was ca. 3 by the end of the injection in May. This was less than half the value calculated for Jul ($\Gamma \approx 7$), from observations collected at X-4 (Fig 1.5c). It was also four times lower than the dilution in Sep at the base of the SML ($\Gamma \approx 14$), estimated from observations collected at X-5 (Fig 1.5e). Note that the total dilutions were estimated from observations collected at different sites, depending on the experiment (Figs. 1.2b-d). The distance from the sampling site to the inflow x_{0m} was 380 m in May and Jul, and 505 m in Sep. The additional entrainment into the gravity current (Γ_E , Eq. 1.3) due to larger value of x_{0m} in Sep was estimated to be 16.5%. The large values of Γ observed in Lake Béznar can be attributed to strong mixing rates near the inflow section or at the upper interface of the gravity current. These processes are examined next. Other processes leading to wide or split intrusions, such as braiding of rivers or incomplete mixing of source inflow water (Marti et al. 2011), were deemed negligible in Lake Béznar but could be important in other lakes.

Initial dilution - Strong initial mixing is likely to occur near the inlet, where the river forms a free jet. This is particularly evident in the photographs collected in Sep (Fig. 1.4a). The signature of the main river jet can be seen in transect X-0.5, 30 m from the inflow (plunge region), with flow from top to bottom that is predominately east-south (Fig. 1.4b). Large horizontal velocity gradients develop in this region (with differences of ca. 0.25 m s^{-1} in 40 m), generating instabilities and the formation of horizontal vortices on both sides of the jet (Fig. 1.4a), and leading to large horizontal mixing rates between river and lake water. Once the cold river plunges beneath the reservoir surface, the gravity current flows laterally confined, with strong flow to the east-south at 1 m below the lake surface in Sep experiment (Fig. 1.4c).

Initial dilution values were estimated from tracer concentration (C) profiles collected at a transect between the inlet and X-1, as $\Gamma_1(C) = C_0/C$, or alternatively, from temperature records (T) collected at that same site, as $\Gamma_1(T) = (T_1 - T_0)/(T_1 - T)$. As above, the subscripts 1 and 0 refer to lake surface and inflow conditions, respectively; while no subscript means average values in the gravity current. The average thickness of the current (h) was calculated as in Ellison and Turner (1959), based on the laterally-

averaged velocity profiles in the cross section, $u_G(z)$ (see their Eqs. 1, 2; see also, Wells et al. 2010). Because of the vertical resolution of the velocity data (Table 1.2), the error in our estimates of h can be ± 0.05 m. In May (Fig. 1.6a), $h = 1.24$ m at a cross-section between the inlet and X-1 (Fig. 1.2b). The average tracer concentration (RWT) in the gravity current was $C = 82 \mu\text{g L}^{-1}$ and its average temperature $T = 18.9^\circ\text{C}$ (Fig. 1.6b, c). The initial dilutions $\Gamma_I(C)$ and $\Gamma_I(T)$ were 1.6 and 2.1, respectively. The initial dilutions in Jul were not calculated due to lack of adequate data. In Sep, h was ca. 0.74 m (Fig. 1.6e), $C = 132 \mu\text{g L}^{-1}$, $T = 24.5^\circ\text{C}$ (Figs. 1.6f, g), and the initial dilutions were $\Gamma_I(C) = 3.2$ and $\Gamma_I(T) = 3.5$. Note that our calculations of Γ_I are subject to uncertainty, which is largely associated with errors in the calculation of C and T . However, these errors only account for changes in our estimates ranging from 4% and 14%. As shown in Table 1.4, estimates of initial dilution from field data are consistent with those calculated following theoretical approaches proposed in the literature to quantify this dilution, including the semianalytical model of Hauenstein and Dracos (1984), or the empirical relations based on inflow Froude number (Fr_0) at the inlet, proposed by Johnson et al. (1989) and Fleenor (2001) (Eq. 1.2). Our estimates of initial dilution in the field are also in the upper range of possible values reported in other lake studies, in all cases below 1.7 (Elder and Wunderlich 1972; Hebbert et al. 1979; Ford and Johnson 1983), but within the range of values encountered in laboratory experiments (from 1.5 to 4.5, see Johnson and Stefan 1988).

Gravity current dilution - Shortly after plunging beneath the reservoir surface, the cold river inflow reached normal conditions (Fischer et al. 1979), and the gravity current started to entrain water from the lake surface (gravity current dilution, Γ_E). The gravity current exhibited a wide mixing layer at the top of the down-flow, with interfacial fluid having intermediate density and momentum between those of the lake and the river (Fig. 1.6). The almost linear density and velocity profiles shown in Fig. 1.6 are characteristic of supercritical gravity currents with peak velocities close to the bottom and almost linear gradients above it (Sequeiros et al. 2010; Sequeiros 2012). Densimetric Froude numbers of these gravity currents (Fr), estimated from ADCP and CTD profiles collected at X-1 (Figs. 1.2b-d), were in fact above or close to one in all cases, and equal to 0.84, 1.11, and 1.24 in May, Jul, and Sep, respectively (Table 1.5). The entrainment coefficient (E), calculated from Fr and Eq. 1.4 (Cenedese and Adduce 2010) ranged between 0.001 and 0.01, depending on the experiment, with an average value of $E = 0.005$. These values are consistent with the range of values reported by Wells et al. (2010), $O(10^{-2}-10^{-3})$ for the values of Fr encountered in Lake Bézinar. Note that these estimates of E are highly sensitive to the values of Fr used. In turn, the Fr values are subject to error resulting from the lateral averaging of the velocity information (ca. 10% of the reading), the calculation of average values in the gravity current, and the accuracy of the instruments. The error in our Fr estimates could range

Table 1.4. Field observations and theoretical estimates of intrusion depth, intrusion thickness, and initial dilution for each tracer experiment. We include the values of the variables required in our theoretical estimates using Fischer's model and different approaches.

Variable	Observed	Fischer (literature)	Fischer (modified)
Fr	[0.84 – 1.24]	0.58 ^a	1.0 ^b
E	-	1.2×10^{-5} ^a	5×10^{-3} ^b
Lake temp. profile(s)	-	At the end of the injection (Fig.1.5a, c, e)	From thermistor chains over the injection (Fig. 1.3a-c)
May			
Intrusion depth (m)	6	[11.9 – 12.3]	[4.9– 6.2]
Intrusion thickness (m)	6.2	1.4 ± 10^{-4}	[1.95 – 2.67]
T_0 (°C)	[15.8 – 16.2]	[15.8 – 16.2]	[15.8 – 16.2]
Initial dilution Γ_1	C: 1.6 T: 2.1	1.3 ^c	1.59 ^d , 2.34^e , 2.75 ^f
Jul			
Intrusion depth (m)	6.5	[7.3 – 8.4]	[6.0– 6.8]
Intrusion thickness (m)	4.8	[0.62 – 0.63]	[1.07 – 1.21]
T_0 (°C)	[23.1 – 20.9]	[23.1 – 20.9]	[23.1 – 20.9]
Initial dilution Γ_1	-	1.3 ^c	2.03 ^d , 2.98^e , 3.11 ^f
Sep			
Intrusion depth (m)	shallower: 8 lower: 12	[17.5 – 18.4]	[10.4– 13.6]
Intrusion thickness (m)	shallower: 3 lower: 2.5	[0.65 – 0.66]	[2.06 – 2.29]
T_0 (°C)	[21.4 – 20.3]	[21.4 – 20.3]	[21.4 – 20.3]
Initial dilution Γ_1	C: 3.2 T: 3.5	1.3 ^c	2.42 ^d , 3.22^e , 3.87 ^f

Fr - densimetric Froude number, E - entrainment coefficient, temp or T - temperature, T_0 - inflow temperature, C - tracer concentration

^a Bottom drag coefficient $C_D = 10^{-3}$ and Fischer et al. (1979) Eqs. 6.110 and 6.111 (p. 216-217)

^b Mean value in Table 1.5

^c Average value in the literature for field values (Rueda et al. 2007)

^d Johnson et al. (1989)

^e Fleenor (2001) (Eq. 1.2)

^f Hauenstein and Dracos (1984)

between 7% and 10% of the values shown in Table 1.5, and, as a result, E could deviate 40-60% from its average value (Table 1.5).

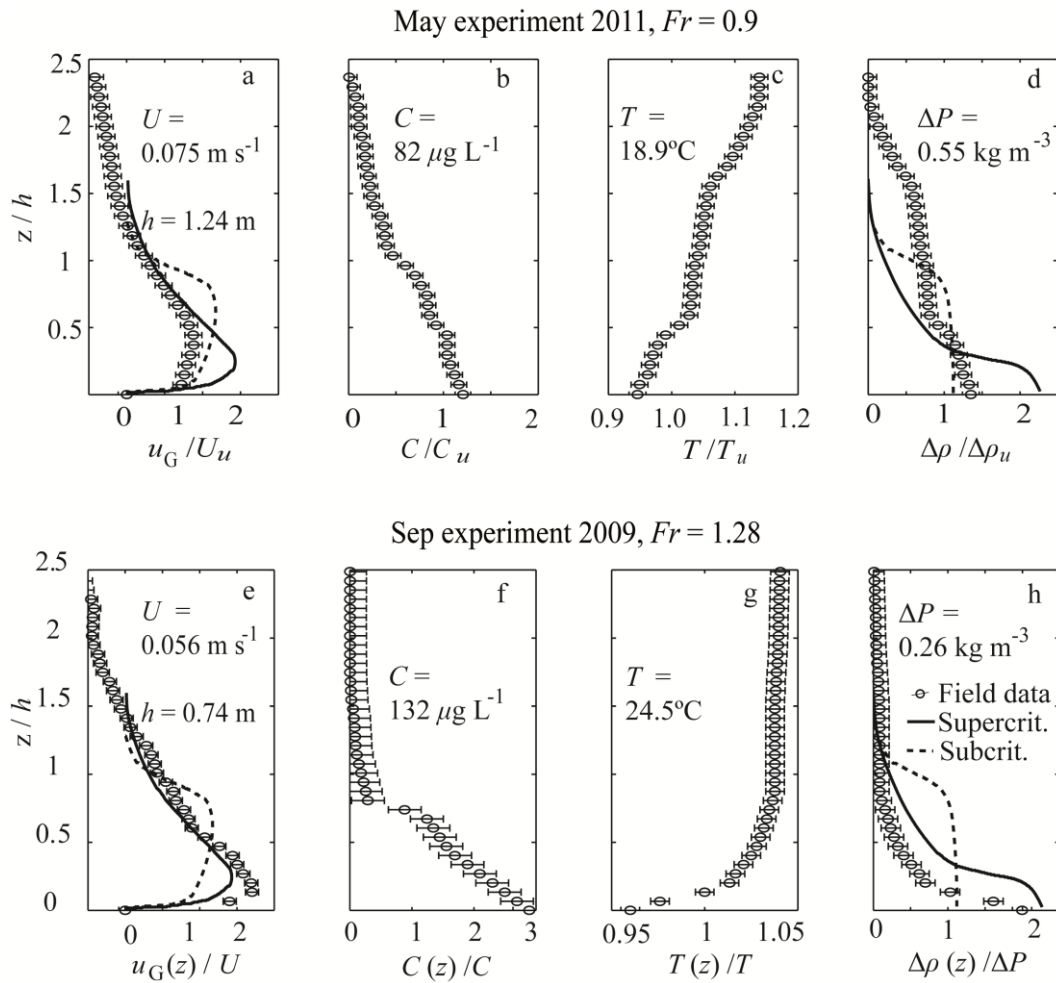


Fig. 1.6. Gravity current profiles in the plunge zone at one transect measured between the inlet and X-1: (a-d) May, and (e-h) Sep. (a, e) Normalized field measured east-west velocity profile laterally averaged across the transect, compared with the fitted curves for the subcritical (subcrit.) and supercritical (supercrit.) regimens defined by Sequeiros (2012). (b, f) Normalized field measured tracer concentration profile. (c, g) Normalized field measured temperature profile. (d, h) Normalized field measured density excess profile, compared with the fitted curves for the subcritical and supercritical regimens defined by Sequeiros (2012). We have included the average values of the variables at the gravity current: velocity (U), tracer concentration (C), temperature (T), density excess (ΔP), and thickness (h).

Internal waves and gravity current dilution- Internal-wave driven oscillations in the lake density structure were observed near the inflow section during all experiments, with maximum amplitudes of up to 2 m in Sep (Figs. 1.3a-c). To establish whether these oscillations affect inflow dynamics, we will consider any given inflow parcel with temperature T_0 entering the lake at time t_0 , and forming an intrusion after Δt_i confined between two isotherms. Once the intrusion develops, the depth of the confining isotherms is largely controlled by the internal waves dynamics; hence, the depth where the intrusion is observed will depend on the timing of observations in the internal wave cycle. However, the internal dynamics can also affect lake-river mixing

Table 1.5. Characteristic values of the gravity current observed at transect X-1 (i.e., buoyancy-dominated region) during the three tracer experiments.

Variable	Tracer experiment		
	May	Jul	Sep
Average thickness, h (m)	1.310	1.200	1.000
Average velocity, U (m s^{-1})	0.055	0.035	0.040
Average reduced gravity, G' (m s^{-2})	3.3×10^{-3}	0.8×10^{-3}	1.0×10^{-3}
Densimetric Froude number, Fr	0.840	1.110	1.240
Entrainment coefficient, E	0.001	0.006	0.010

and, thus, the actual isotherms confining the intrusion. First, the distance along the lake bottom traveled from the plunging point to the insertion depth (ΔS_{0i}), and the length of time to the formation of the intrusion (Δt_i) will vary depending on the timing of the inflow t_0 in the wave cycle. It will also depend on the magnitude of the time-varying velocity of the isotherms oscillating along the lake bottom ($U_i(t)$) compared to the gravity current velocity (U). For $U \gg U_i(t)$, the lake density structure can be assumed fixed for a given inflow parcel, and equal to that prevailing at the time t_0 . This was the case of Lake Béznar, where U is one order of magnitude larger than the maximal isotherm velocity, $U_{i\text{-max}}$. Second, the internal waves dynamics also affect the ambient temperature conditions to which parcels are exposed along ΔS_{0i} . Thus, internal oscillations affect both ΔS and E in Eq. 1.3, hence, gravity current dilution. To assess the effect of internal waves in inflow dynamics, Fischer's model was applied to simultaneous observations of inflow temperatures T_0 and lake temperature profiles, constructed from thermistor records at site-S (Fig. 1.2a). In these calculations, we incorporated initial dilutions Γ_1 estimated by Eq. 1.2 (Table 1.4; with values of 2.34, 2.98, and 3.22, in May, Jul, and Sep, respectively), and entrainment rates E estimated from the field observations (see above). The results are shown in Table 1.4 (see 'Fischer modified' column). Note that the theoretical intrusion depths sweep the range of depths where tracer was observed in May and Jul (Fig. 1.5a, c). The deeper intrusion observed in Sep can also be explained with the estimates of Table 1.4 (Fig. 1.5e). However, the formation of the shallower intrusion observed in Sep remains unexplained, if we use Fischer's model.

Interflows, underflows and splitting - The splitting of the gravity current at a density step due to strong mixing rates with the ambient water occurred at the base of the SML in Sep. It can be parameterized in terms of the transition Richardson number (Ri_{12}), defined in terms of local variables, as the ratio of density step ($\rho_2 - \rho_1$) in the ambient water, and the density excess of the down-flow at the base of the SML ($\rho_G - \rho_1$).

$$Ri_{12} = \frac{\rho_2 - \rho_1}{\rho_G - \rho_1} \quad (1.7)$$

Here the subscript 1 refers to the surface mixed layer (SML) with thickness D and the subscript 2 refers to the layer (metalimnetic) below the density step. This concept was introduced in terms of initial variables for two-dimensional plumes (Wallace and Sheff 1987), and more recently applied to laboratory and field experiments (Wells and Wettlaufer 2007; Forrest et al. 2008). Wells and Wettlaufer (2007) demonstrated that there exists a critical value for the transition Richardson number (Ri_{12c}), so that if $Ri_{12} \gg Ri_{12c}$ the gravity current will form an interflow just above the density step; by contrast, if $Ri_{12} \ll Ri_{12c}$, it will penetrate through the density step forming an underflow (Figs. 1.7a,b). For $Ri_{12} \approx Ri_{12c}$, Wells and Wettlaufer (2007) observed that part of the gravity current flowing into the density step would leak to the bottom, as an underflow. We will refer to this third case as a ‘split’ gravity current (Fig. 1.7c). According to Eq. 1.7, we expect $Ri_{12c} \approx 1$, given that the gravity current will only penetrate through a density step when it is denser than the underlying fluid, i.e., $(\rho_G - \rho_1) > (\rho_2 - \rho_1)$, or alternatively for $Ri_{12} < 1$. For $Ri_{12} \geq 1$ mixing between the ambient water and the downflow, as the gravity current descends through the SML, will generate sufficient interfacial fluid with intermediate properties between the river and the SML, so that a fraction of the cold river water will detrain at the base of the SML.

To calculate the transition Richardson numbers for the stratification and the inflow conditions prevailing during the tracer experiments, Eq. 1.7 was rearranged and expressed in terms of the the density step at the base of the SML, density excess at the inflow section, and the total dilution of the gravity current at the base of the SML (Γ) as follows,

$$Ri_{12} = \left(\frac{\rho_2 - \rho_1}{\rho_0 - \rho_1} \right) \Gamma \quad (1.8)$$

The total dilution at the the base of the SML can be defined as the product of the initial dilution in the plunge zone, Γ_I (Eq. 1.2), and the gravity current dilution in the buoyancy-dominated region, Γ_E (Eq. 1.3). The different terms in Eq. 1.8 were calculated as follows. The density step at the base of the SML ($\rho_2 - \rho_1$) was estimated from the observed temperature profiles (*see* dark dashed lines in Figs. 1.5a,c,e). Two different models were fitted to represent the temperature variations with depth in the SML and in the metalimnion. The density within the SML (ρ_1), was assumed constant and equal to the observed average density between $z = 0$ and $z = -D$. In the metalimnion, densities were assumed to vary linearly. A linear equation was fitted to the observed temperatures below $z = -D$ (*see* gray dashed lines in Figs. 1.5a,c,e). The differences in densities at $z = -D$ estimated with the constant SML temperature model and the best linear temperature model in the metalimnion were taken as the density step (*see* $T_1 - T_2$ in Figs. 1.5a,c,e).

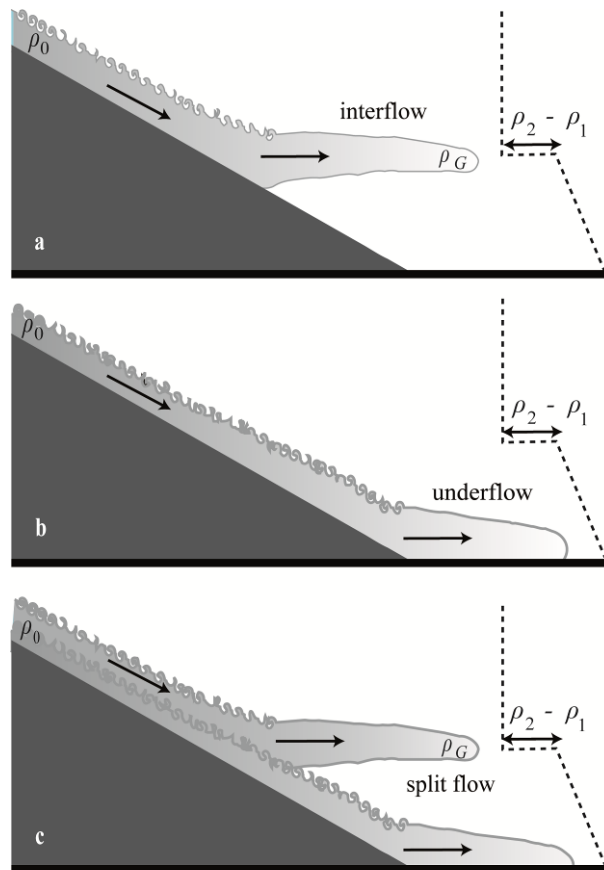


Fig. 1.7. Possible behaviors of a cold plunging inflow (ρ_0) into a two-layered stratified system with a density step ($\rho_2 - \rho_1$) at the base of a warm constant temperature surface mixed layer (SML) with a linearly stratified metalimnetic layer underneath: (a) interflow (b) underflow, and (c) split flow, where ρ_G is the density of the current at the base of the SML.

The initial dilution at the plunge zone (Γ_1) was estimated from Eq. 1.2. The gravity current dilution was estimated from Eq. 1.3, using the mean entrainment coefficient for the observed gravity currents ($E = 0.005$); a distance down-slope $\Delta S = D / \sin(\theta)$, with $\sin(\theta) \approx 0.02$ (see *Study Site*); and an average gravity current thickness h ranging between 1.0 – 1.3 m (Table 1.5).

The transition Richardson number Ri_{12} was 0.85 ($Ri_{12} < 1$) in May, when we observed an underflow below the SML (Fig. 1.5a). In Sep, Ri_{12} was 1.04 ($Ri_{12} > 1$), when the gravity current ‘splits’ and forms two intrusions (Fig. 1.5e). These observations suggest that a cold plunging flow will penetrate through the base of the SML or, alternatively, will form intrusions at that level, depending on whether Ri_{12} is below or above $Ri_{12c} \approx 1$, as hypothesized. If we accept this interpretation, in Jul, based on the value of Ri_{12} ($=1.36$), one would expect the gravity current to form an intrusion at the base of the SML. A narrow intrusion was, in fact, observed between the SML and the NID, which were only separated ca. 2 m at that time (Fig. 1.5c; Table 1.3). Given the minimum thickness of single intrusions observed (2.5 m, Table 1.4), we cannot

establish whether the gravity current split or formed a single intrusion at the base of the SML in Jul. In any case, the results of Jul are also consistent with our interpretations, based on Ri_{12} , of the fate of gravity currents as they cross the base of the SML.

Portion of river buoyancy flux directly reaching the SML – We estimate the portion of the river water that flows along the base of the SML (b_1) as a function of the gravity current properties and the density step as follows. First the buoyancy flux, $B_G(z)$, was calculated as a function of height (z) in the gravity current from the observed velocity and density excess profiles at the gravity current (e.g., Figs. 1.6a,d in May), as

$$B_G(z) = W \frac{g}{\rho_1} \int_0^z \Delta\rho(z) u_G(z) dz \quad (1.9)$$

Here W is the width of the basin at the observation site (ca. $W = 155$ m), $u_G(z)$ is the gravity current velocity profile, and $\Delta\rho(z)$ is its density excess profile, calculated from the density profiles and the density of the SML (ρ_1). The function $B_G(z)$ is maximum and equal to the total inflow buoyancy flux (B_0) at the top of the current, i.e., $B_G(\infty) = B_0$ (see Figs. 1.8a,c,e in May, Jul and Sep, respectively). It can also be expressed in terms of $\Delta\rho(z)$ rather than z , since the density excess profile within the gravity current is a monotonic function of height, z , and can be made non-dimensional using the total inflow buoyancy flux, B_0 . This non-dimensional function will be referred to as $b_2(\Delta\rho) = B_G(\Delta\rho)/B_0$ (Figs. 1.8b,d,f). It is only based upon the internal gradients within the gravity current, and represents the fraction of B_0 with enough density to flow through the density step ($\Delta\rho_{12}$) into the metalimnion. The remaining fraction ($b_1 = 1 - b_2$), represents the fraction of B_0 that inserts along the base of the SML. Laboratory experiments of Cortés et al. (2014b) have found that the fraction of inflow water that intruded at the base of the SML, rather than flowing to lower depths, could be well predicted with this approach. These calculations applied to our field observations suggest that all the inflow penetrated below the SML ($b_2 = 1$) in May, when a density step $\Delta\rho_{12}$ of 0.26 kg m^{-3} was observed below the SML. This is in agreement with the tracer observations (Figs. 1.5a, 1.8b). In Jul, with $\Delta\rho_{12} = 0.10 \text{ kg m}^{-3}$, b_2 was 0.1, which suggests that 90% of B_0 became an interflow at the base of the SML (Fig. 1.8d). Note though, that the tracer concentration profiles at that time were not conclusive on whether all or only part of the inflow plume flowed along the SML ($b_1 = 1$), given the small vertical distance between D and NID. Finally, in Sep, with $\Delta\rho_{12} = 0.072 \text{ kg m}^{-3}$, it was estimated that 90% of B_0 penetrated below the SML ($b_2 = 0.9$; Fig. 1.8f). The remaining 10% (b_1) became an interflow, being subsequently mixed into the SML over night (Figs. 1.5e-f).

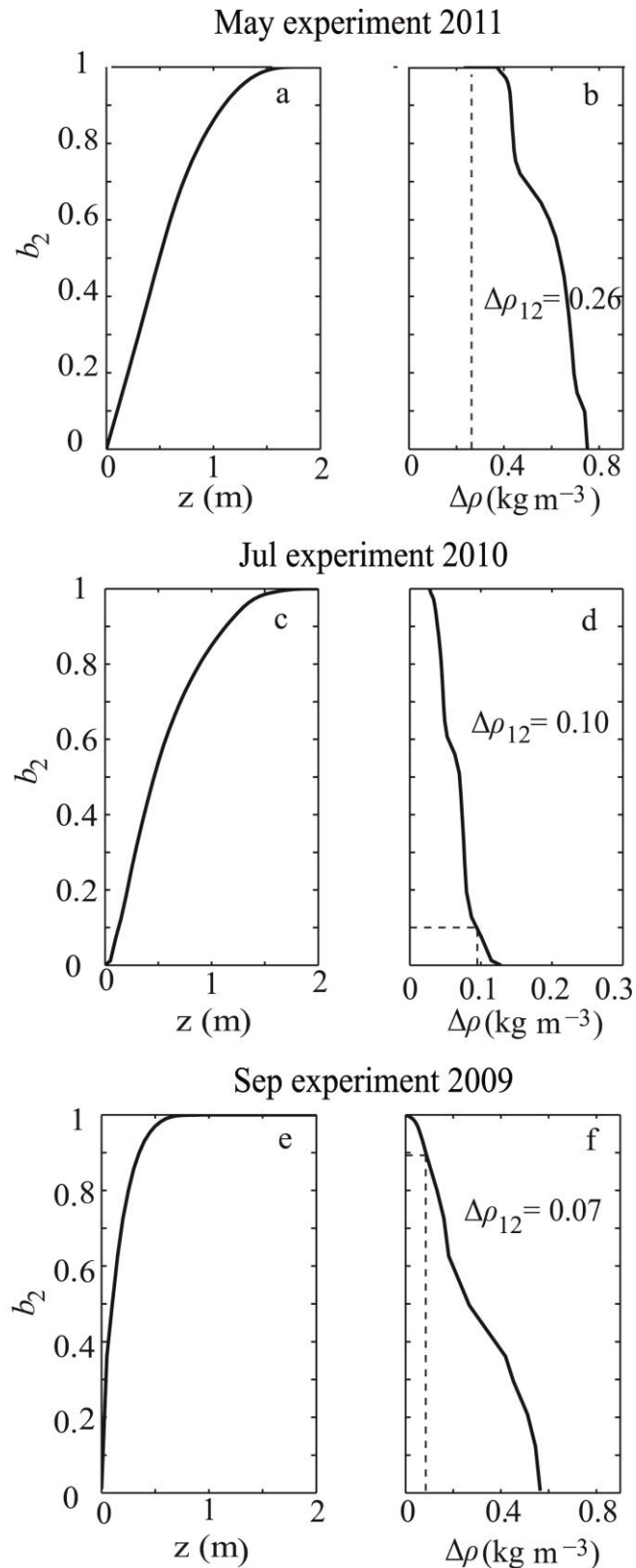


Fig. 1.8. Estimation of the fractions of river buoyancy flux that penetrates the density step (b_2), from gravity current profiles at one transect measured close to X-1: (a, b) May, (c, d) Jul, and (e, f) Sep. (a, c, e) Portion of the river buoyancy flux that penetrates the density step (b_2), as a function of height (z). (b, d, f) Portion of the river buoyancy flux that penetrates the density step (b_2), as a function of the density excess ($\Delta\rho$). We mark the density step at the base of the SML ($\Delta\rho_{12}$) for each experiment.

Hourly and seasonal variations in the pathways of distribution of river water –

If we accept the Ri_{12} parameterization proposed above (Eq. 1.8), one can use the hydrological information and the thermistor records to characterize the hourly and seasonal scale variability of the behavior of cold plunging flows in Lake Béznar. Hourly scale changes in the temperature contrast between lake and river water and in the thickness of the SML can be seen in Figs. 1.3a-c. The largest hourly variations in Ri_{12} occurred in Jul. The maximum thickness of the SML and lowest temperature differences between the river and lake surface, hence, the maximum values of Ri_{12} (i.e., $Ri_{12} > 1$), tended to occur late in the afternoon and early evening (ca. 19:00 h), when the river would form intrusions at the base of the SML. Late in the morning (at 11:00 h) the thinnest SML, and highest temperature differences between the river and the SML we recorded. As a result, values of $Ri_{12} < 1$ are calculated in the morning, when one would expect the river to form metalimnetic intrusions that penetrate below the base of the SML.

At seasonal scales, daily values of Ri_{12} were calculated from Eq. 1.8, using daily averaged river and lake temperatures from the thermistor chain at site-M. These seasonal estimates of Ri_{12} were consistent with those calculated from CTD-data collected during the tracer experiments, which supports the use of daily averaged data to predict the seasonal behavior of the inflowing plume (Figs. 1.5 and 1.9a). The seasonal estimates of Ri_{12} are shown in Fig. 1.9a for 2011, when river temperature data were continuous. Based on the evolution of Ri_{12} , the stratification period in Lake Béznar can be divided into three subperiods (Fig. 1.9a) depending on the river plume behavior. (1) Early in the stratification period, from May to mid-June ($Ri_{12} < 1$), the river is expected to form underflows. The low values of Ri_{12} early in the stratification period are associated with low values of the density step at the base of the seasonal SML ($\rho_2 - \rho_1$), and high density differences between river and lake surface ($\rho_0 - \rho_1$; Fig. 1.9b), which also minimize dilutions of the inflowing plume Γ (Figs. 1.9c-f). (2) Interflows or split-flows form under strongly stratified conditions from mid-June to mid-August, with $Ri_{12} > 1$. The large values of Ri_{12} during this period of time are associated with strong stratification ($\rho_2 - \rho_1$) and weak inflow buoyancy ($\rho_0 - \rho_1$; Fig. 1.9b). The dilutions during this sub-period are larger than those estimated for sub-period 1 (Figs. 1.9c,d) as a result of the increasing values of both Fr_0 and D (Figs. 1.9e,f). Interflows at the base of the SML are likely to be observed in this sub-period, resulting in rapid entrainment of river water into the top layers. (3) Ri_{12} oscillates above and below unity from mid-August to September, and all regimes are possible. In this subperiod, the density contrast ($\rho_2 - \rho_1$) was the smallest of the year (Fig. 1.9b); river temperatures decreased faster than the lake surface, hence, ($\rho_0 - \rho_1$) increased (Fig. 1.9b); and dilutions reach maximal values (Fig. 1.9c, d), likely associated with the high values of Fr_0 and D (Fig. 1.9e, f). Depending on the distance from the NID to the base of the SML (D),

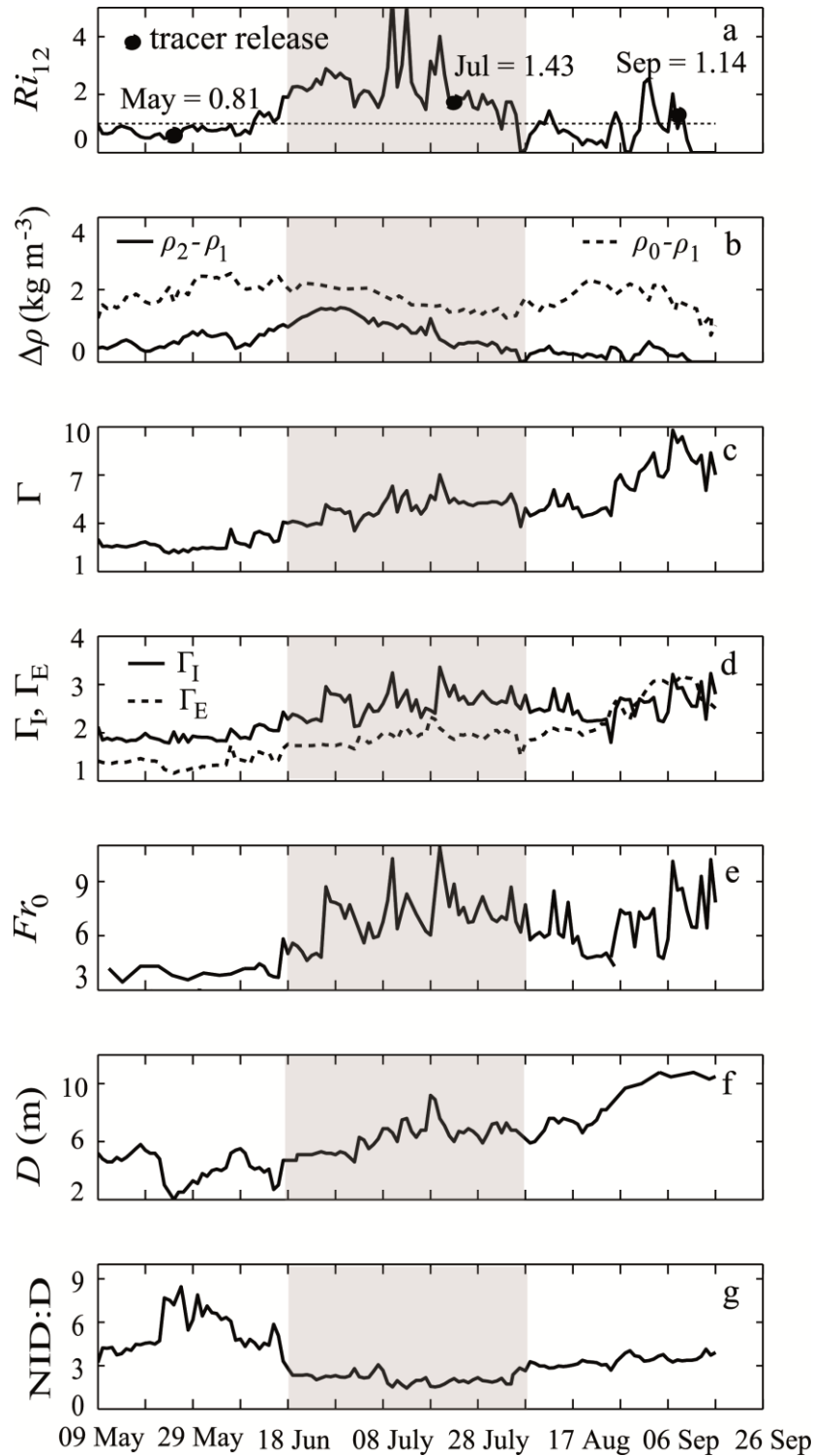


Fig. 1.9. Seasonal estimations of transition Richardson number (Ri_{12}) and its controlling factors, using daily data of 2011 at site-M. In all panels, the shadow region corresponds to the sub-period of maximum stratification. (a) Estimations of Ri_{12} . We include the values of Ri_{12} for the days of the tracer experiments (black dots) according to daily records, independently of the year of the release. (b) Density changes at the base of the SML ($\rho_2 - \rho_1$), and inflow-SML density differences ($\rho_0 - \rho_1$). (c) Total dilution (Γ). (d) Initial dilution (Γ_I), and gravity current dilution (Γ_E). (e) Inflow Froude number (Fr_0). (f) Thickness of the surface mixed layer (D), as the daily maximum from hourly estimates with $\Delta T_{0z} = 0.2^\circ\text{C}$. (g) Ratio of nominal intrusion depth to surface mixed layer thickness, [$\text{NID} : D$].

underflows may or may not be readily incorporated into the SML. If the ratio $[NID : D] > 3$, as is the case in subperiods 1 and 3, one will be able to differentiate between interflows, underflows and split flows. If $[NID : D] \leq 3$, the actual fate of the river inflow into the lake will be difficult to observe in the field. This is the case during subperiod 2 in Fig. 1.9g, when the analysis predicts the occurrence of alternating interflows and split flows.

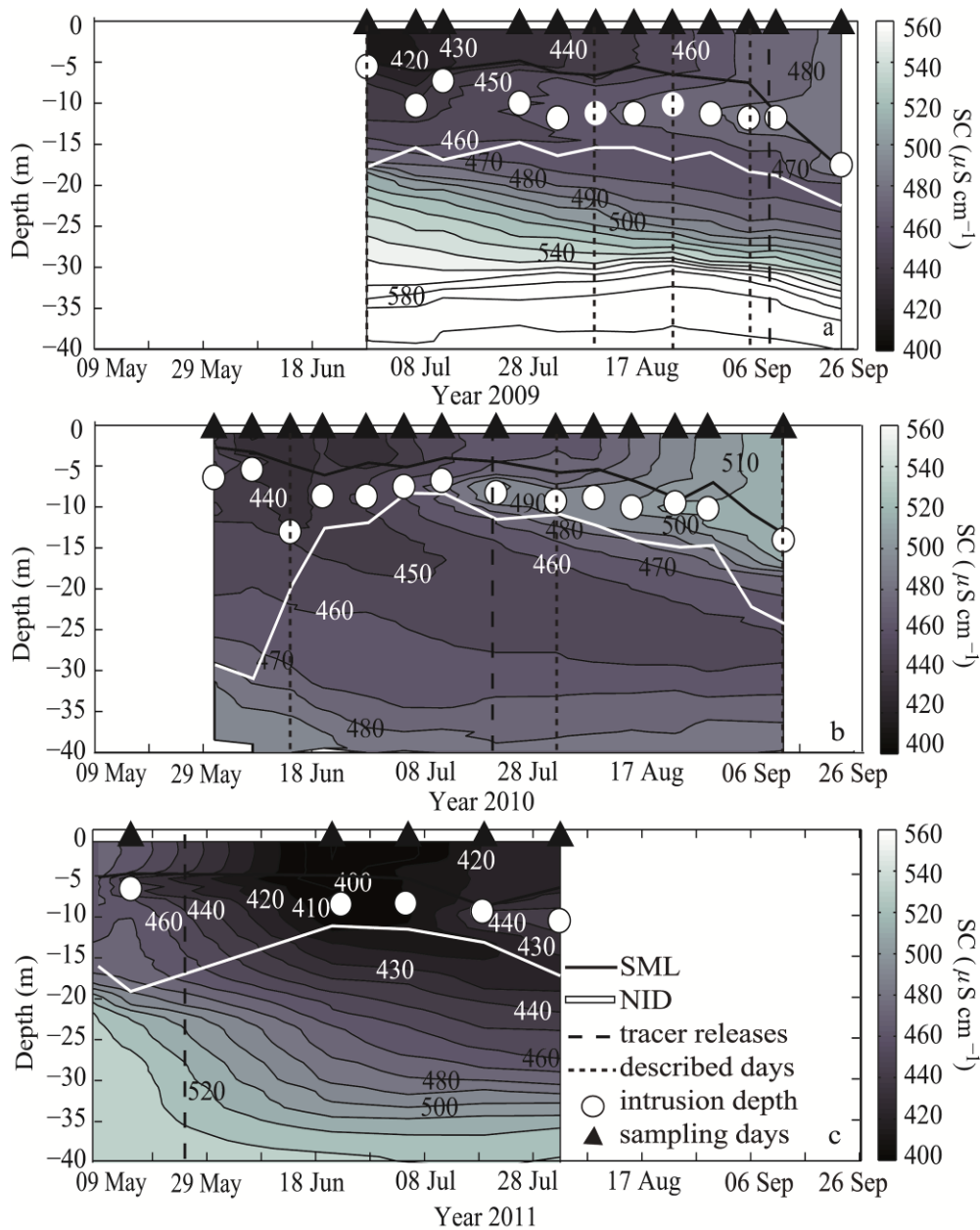


Fig. 1.10. Seasonal evolution of reservoir specific conductance (SC) at site-M in years (a) 2009, (b) 2010, and (c) 2011. Intrusion depths (white dots) are estimated as the average depth where the lake SC equals the SC at the intrusion (SC_m). The former is calculated as $SC_m = SC_1 (\Gamma - 1) + SC_0$, where the subscripts indicate whether the SC is measured at the inflow (0), lake surface (1), and intrusion (m), and Γ is the total dilution at the plunge zone and buoyancy-dominated region.

SC data collected in 2009, 2010, and 2011 at site-M are consistent with our predictions of the fate of the cold inflow as a function of Ri_{12} (Fig. 1.10). SC was assumed a passive tracer of river water. (1) The lowest SC in the reservoir in late spring (May and June) occurred at middepth (*see*, e.g., 14 Jun 2010, in Fig. 1.10b), as a result of river inflows with low SC (the lowest SC values during the year, not shown) forming deep underflows. In late spring, a fraction of low SC inflow water could be found in the surface layers, even when the daily averaged NID was well below the SML (e.g., 28 June 2009, *see* Fig. 1.10a). This could be, at least partly, attributed to hourly scale changes in the intrusion depths. For example, in Fig. 1.3a the changes in NID at that time of the year are very large, leading to the development of shallow intrusions very close to the base of the SML. (2) Under strongly stratified conditions (in July and August) peak values of SC are observed between the SML and the TID, indicative of river intrusions with higher SC (*see*, e.g., 02 August 2010 in Fig. 1.10b). Lower SC values were observed near the surface in this period, but these values increased with time, which can be interpreted as the result of a fraction of the inflows reaching the surface layers (compare, e.g., 09 August 2009 with 23 August 2009, in Fig. 1.10a). (3) In late summer-early fall (September), the highest reservoir SC values, associated with high SC values in the river, occurred again near the surface. They were likely associated with both splitting flows (e.g., 06 September 2009, *see* Fig. 1.10a) and interflows (e.g., 13 September 2010, *see* Fig. 1.10b).

Conclusions

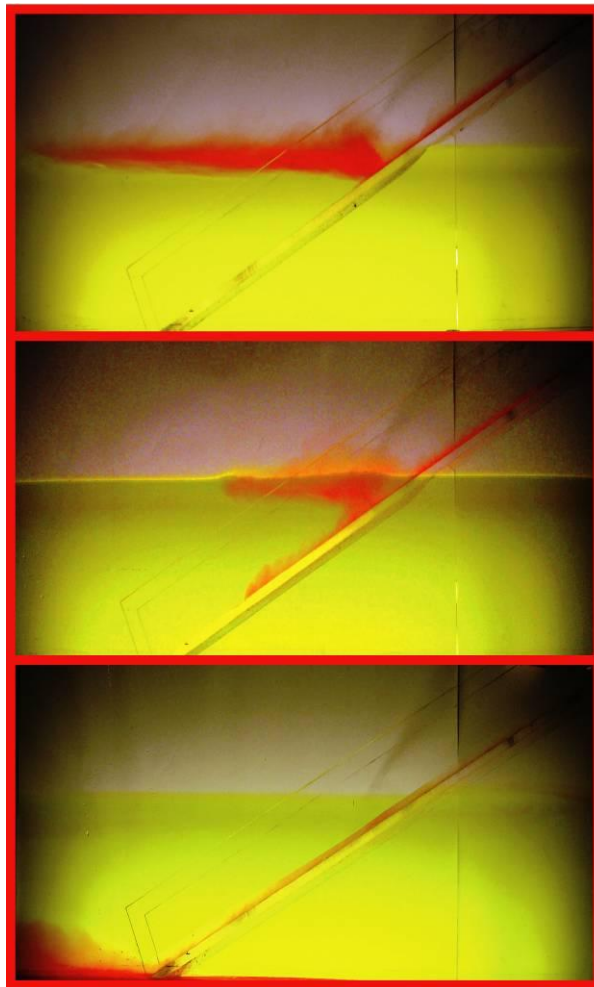
Our field observations indicated that a significant fraction of the cold plunging inflow can be incorporated into the surface layers shortly after entering the stratified reservoir, even if its nominal intrusion depth is well below the SML. This fraction varied, depending on conditions, from 0% at the beginning of the stratification period (May) to nearly 100% at the time of maximum stratification (Jul). In Sep, this fraction (10%) was similar to that reported by Fischer and Smith (1983) in Lake Mead. Depending on conditions at the time of the experiment, a density current was observed either flowing entirely at the base of the SML (interflow), penetrating the thermocline to form an unique and deep metalimnetic intrusion (underflow) or, even splitting to form both an interflow and an underflow. In the late summer-early fall experiment, part of the density current detached at the base of the SML, leading to the development of two intrusions: one near the theoretical intrusion depth (TID) in the metalimnion, and another at the base of the SML. The shallower intrusion was entrained into the surface layers the following night, as a result of convectively-driven deepening of the SML.

The formation of intrusions near the base of the SML and the subsequent entrainment into the SML can result in fluxes of riverborne nutrients added directly to

the surface layers of the reservoir, where they can be readily used for phytoplankton growth. Quantifying these fluxes is needed to assess biological responses to high nutrient pulses introduced by cold river inflows. The fate of these available nutrients influence reservoir ecology and its water quality.

Chapter 2

EXPERIMENTAL OBSERVATIONS OF THE SPLITTING OF A GRAVITY CURRENT AT A DENSITY STEP IN A STRATIFIED WATER BODY



This article is published in the **Journal of Geophysical Research-Oceans** as:

Cortés, A., F. Rueda, and M.G. Wells (2014), Experimental observations of the splitting of a gravity current at a density step in a stratified water body. *J. Geophys. Res.*, 119, 1038–1053, doi:10.1002/2013JC009304

Abstract

When a gravity current reaches the level of neutral buoyancy in a stratified water body it can separate from the sloping boundary as an intrusion. If there is a density gradient within the gravity current, then multiple intrusions can form in the stratified water body. Using a series of laboratory experiments in a two-layered ambient stratification, we document how a gravity current splits in two upon reaching the sharp density step. Our laboratory observations stress the significance of the densimetric Froude number of the gravity current (Fr), as well as a measure of the ambient stratification (density Richardson number, Ri_ρ), on determining how a gravity current intrudes into a two-layered stratified ambient water. Gravity currents are more likely to detrain into two parts at a density step when they have a diffuse density interface ($Fr > 1$). However, gravity currents tend to intrude as a single intrusion when they have a sharp, more step-like density profile ($Fr < 1$). Using details of the internal structure of the gravity current, we develop a theory to predict the partition of the buoyancy flux into the interflow and underflow when the gravity current splits at the density step. Our predictions of buoyancy portions are in agreement with our experimental observations. We discuss when the application of our equations will be relevant for river intrusions into reservoirs, and for gravity currents in the stratified ocean.

Introduction

Gravity currents are central to our understanding of large scale vertical transport in oceans, seas and deep lakes (Peeters and Kipfer 2009). In the ocean, they develop as a result of dense water forming in marginal seas or coastal shelves in response to strong evaporation, heat fluxes, or brine rejection from sea-ice formation (Legg et al. 2009), and tend to sink down the continental slope. In lakes, gravity currents are driven either by external input of cold water, such as cold river inflows (Fischer et al. 1979; Hebbert et al. 1979) and inter-basin exchange (Aeschbach-Hertig et al. 1996; Kipfer and Peeters 2000); or by internal processes, such as differential cooling (Monismith et al., 1990; Wells and Sherman 2001; Fer et al. 2002), thermal-bar mixing (Malm et al. 1994), and even thermobaric instabilities (Hohmann et al. 1997). Their contribution to basin-scale vertical transport, however, largely depends on the rate of mixing with the ambient water and the depth where they intrude laterally in stratified water columns.

A large number of theoretical and experimental studies have been conducted to understand the interaction of gravity currents with the ambient stratification. Some of these studies have dealt with linearly-density stratified basins (Baines 2001; Fernandez and Imberger 2008a; Wells and Nadarajah 2009). A two-layered stratified basin,

though, is a good approximation of a lake with a well-mixed surface layer separated by a sharp density step from the deep and dense waters (Rimoldi et al. 1996; Monaghan et al. 1999; Samothrakis and Cotel, 2006a, 2006b; Wells and Wettlaufer, 2007). Two possible outcomes have been previously described for a gravity current descending into a two-layered stratified basin (Fischer et al. 1979): if the impinging current is lighter than the lower layer, the gravity current will separate from the bottom and will flow laterally along the density step forming an intrusion (Fig. 2.1a); otherwise, it will penetrate the base of the surface layer and it will flow laterally along the bottom of the basin (Fig. 2.1b) (Wells and Wettlaufer 2007). These two possibilities have long been recognized by limnologists who use the terminology of ‘interflow’ for the subsurface intrusion, and ‘underflow’ to refer to a gravity current spreading along the bottom of the water body (Imberger and Hamblin 1982).

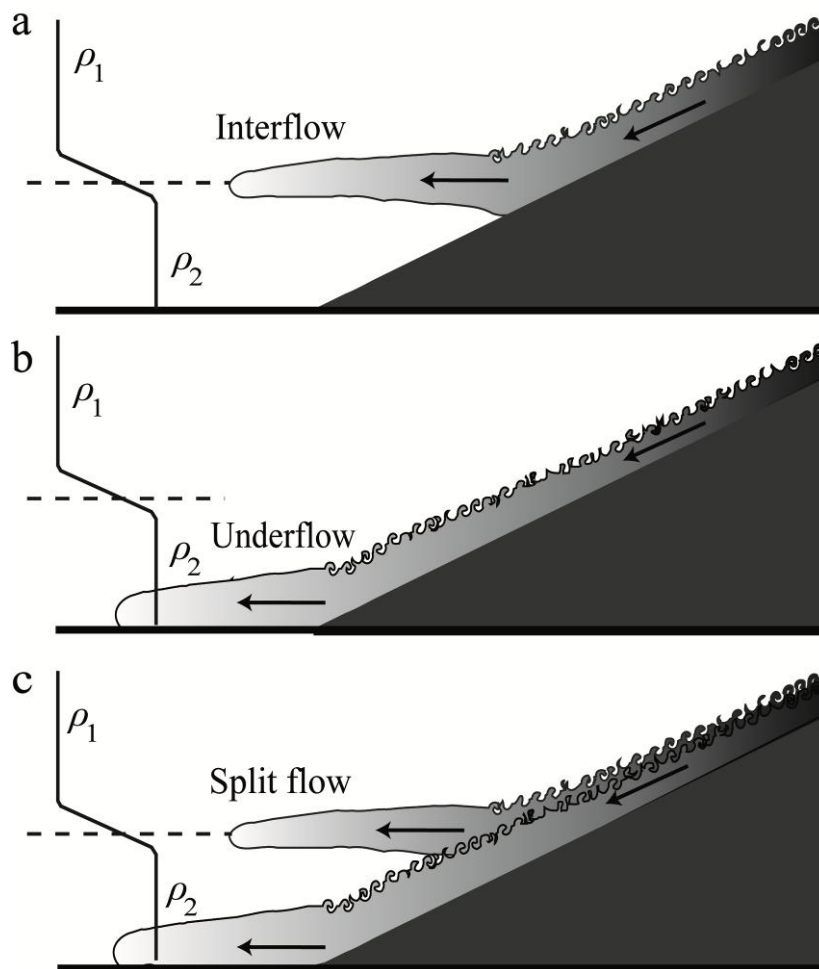


Fig. 2.1. Behavior of a 2D-gravity current of average density ρ_G in a two-layered stratified environment, ρ_1 and ρ_2 . (a) Interflows occur when $\rho_1 < \rho_G < \rho_2$. (b) Underflows occur if $\rho_G > \rho_2$. (c) Split flows form if the gravity current has significant internal density gradients.

Gravity currents can also split as they impinge into a density step to form two intrusions (Fig. 2.1c, see also Monaghan (2007)). This behavior has been previously observed in laboratory experiments with vertical plumes (Kulkarni et al. 1993; Cotel and Breidenthal 1997) and turbidity currents (Rimoldi et al. 1996). Klymak and Gregg (2001) also observed splitting gravity currents in Knight Inlet (British Columbia, Canada) when they report on the existence of a ‘net isopycnal flow of water into the middle layer’, at the time when a dense gravity current spills over a sill flowing into the stratified ocean. De Cesare et al. (2006) present further evidence of splitting gravity currents at the base of the thermocline in a strongly stratified Lake Lugano downstream of Cassarate River, during a flood event when the river was highly loaded with suspended sediments (see their Figs. 7 and 9). However, no indication was given of when splitting gravity currents should occur. More recently, Wobus et al. (2013) conducted a series of simplified numerical experiments of gravity currents in three-layered stratified basins, and reproduced the three behaviors (interflow, underflow and splitting) shown in Fig. 2.1. The authors relate the percentage of passive tracer within a given depth range with the inflow rate and salinity. Recent field observations in a Mediterranean reservoir by Cortés et al. (2014a) showed that a cold river inflow could split at the base of the surface mixed layer (their Fig. 1.5e), and the authors also identified inflow and ambient stratification features that could lead to the development of multiple intrusions. The interpretation of the inflow behavior in the field by Cortés et al. (2014a) is largely based on the results presented here, which were gathered under controlled laboratory settings and aimed at establishing the conditions that need to hold for the splitting of a gravity current at a density step.

Wells and Wettlaufer (2007) proposed that the extent to which a gravity current detaches or penetrates at a density step can be expressed in terms of the density Richardson number (Ri_ρ), which is a function of the density differences across the density step, its depth from the surface, and the inflow buoyancy flux per unit width of the gravity current (see Eq. 2.1). For values of Ri_ρ above a given threshold Ri_ρ^* , the gravity current should form an interflow at the density step (Fig. 2.1a). For $Ri_\rho < Ri_\rho^*$, in turn, it should penetrate through the density step forming an underflow (Fig. 2.1b). For $Ri_\rho \approx Ri_\rho^*$, Wells and Wettlaufer (2007) observed that part of the gravity current flowing into the density step would leak to the bottom, as an underflow, and formed multiple intrusions (Fig. 2.1c). They found that the critical values of Ri_ρ could range from 21 to 27.

We hypothesize that the extent to which a gravity current impinging on a density step in a stratified water column either detaches, penetrates or splits is not only controlled by the density Richardson number (Ri_ρ), but also by the internal velocity and density gradients existing within the gravity current. This hypothesis is partly based on previous simulations of large scales flows conducted by Legg et al. (2006, 2009) and Xu et al. (2007). Their ability to simulate the splitting of gravity currents (our Fig. 2.1c)

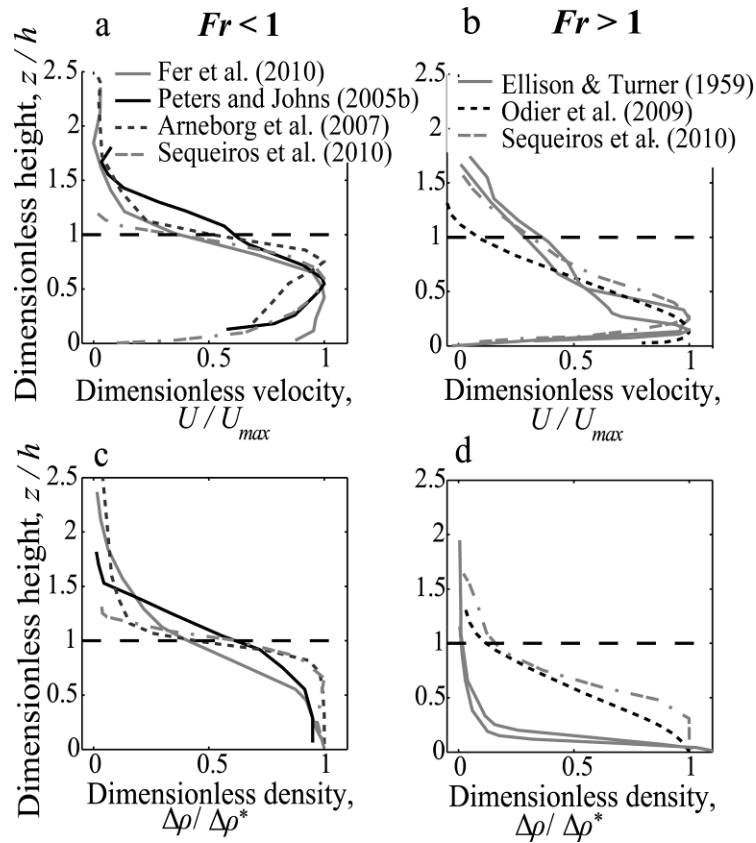


Fig. 2.2. Summary of field and laboratory observations of gravity current profiles: velocity (2a and 2b) and density excess (2c and 2d). Data has been normalized by the average thickness of the gravity currents (h), and by maximum values of velocity and density excess (U_{max} and $\Delta\rho^*$). Subcritical flows ($Fr < 1$) are shown in 2a and 2c, and supercritical flows ($Fr > 1$) in 2b and 2d.

was largely dependent on whether they could resolve the internal density and velocity gradients. Kulkarni et al. (1993) argued that because of the variation in density within turbulent vertical plumes, part of the mixed fluid could detrain at a density step. Many experiments, from the early results of Ellison and Turner (1959) to the more recent of Sequeiros et al. (2010), have shown that density and velocity vary within gravity currents. These variations are largely determined by the intensity of turbulent mixing at the interface layer at the top of the current, parameterized in terms of the densimetric Froude number of the gravity current (Fr , see Eq. 2.2). A series of normalized velocity and density excess profiles from published results are shown in Fig. 2.2. Data is taken from laboratory experiments of Ellison and Turner (1959), Odier et al. (2009), and Sequeiros et al. (2010), and field observations from the Red Sea overflow (Peters and Johns 2005a,b), the Baltic inflow (Arneborg et al. 2007), and the Faroe Bank overflow (Fer et al. 2010). Subcritical ($Fr < 1$, Fig. 2.2a and 2.2c) and supercritical gravity current profiles ($Fr > 1$, Fig. 2.2b and 2.2d) are presented separately. Note that, in general, subcritical gravity currents ($Fr < 1$) tend to exhibit a step-like velocity and density profiles with a sharp interface layer at the top of the current. Supercritical

gravity currents ($Fr > 1$), in turn, tend to have more diffused velocity and density profiles with a thicker interface layer at the top of the current. Hence, one would expect larger volumes of mixed fluid detaching from gravity currents flowing along density steps in the case of supercritical gravity currents.

To test our hypothesis, a series of controlled laboratory experiments of dense inflows in a two-layered stratified tank are conducted, in which we modified some initial conditions to vary the densimetric Froude numbers (Fr) and, the density contrast between the two layers in the tank (hence, Ri_ρ), but the currents have identical buoyancy flux per unit width. We will further propose a theory to quantify the portions of the buoyancy flux that go into each intrusion, based upon the density and velocity profiles of the gravity current and the magnitude of the ambient density step, and will test it with the experimental observations. First, the preliminary definitions and theory are presented. Second, the experimental set up is described, and the observations afterwards. In the following section, the laboratory results are used to test the theory presented. We then assess the relevance of our findings in the interpretation of field observations. Finally, the conclusions are stated.

Theory

In this work, we consider the behavior of a two-dimensional (2D) gravity current flowing down a slope of angle θ in a two-layered stratified tank (Fig. 2.3a). We will use the symbols x and y to refer to the horizontal and vertical coordinates, respectively, relative to the bottom-right corner of the tank, below the gravity current inflow. The along-slope and normal-to-the-slope coordinates will be referred to as S and z , respectively. We will refer to the initial densities of the two ambient layers as ρ_1 in the surface, and ρ_2 in the bottom layer. The later will be denser than the top layer (i.e., $\rho_2 > \rho_1$), and the density step between them is defined as $\Delta\rho_{12} = (\rho_2 - \rho_1)$. We further define H as the vertical distance from the initial depth of the gravity current to the density step, and L as the total length of the tank. The gravity current, in turn, is initially characterized in terms of its inflow rate Q_0 , density ρ_0 , width W , inflow reduced gravity $g'_0 = g (\rho_0 - \rho_1) / \rho_1$, and its inflow buoyancy flux per unit width $B_0 = g'_0 Q_0 / W$ [$\text{m}^3 \text{s}^{-3}$]. The density Richardson number (Ri_ρ) is calculated as,

$$Ri_\rho = \frac{g'_{12} H}{B_0^{2/3}} \quad (2.1)$$

where, $g'_{12} = g \Delta\rho_{12} / \rho_1$ represents the reduced gravity of the ambient water density step, and g is the gravitational acceleration. The densimetric Froude number (Fr) is

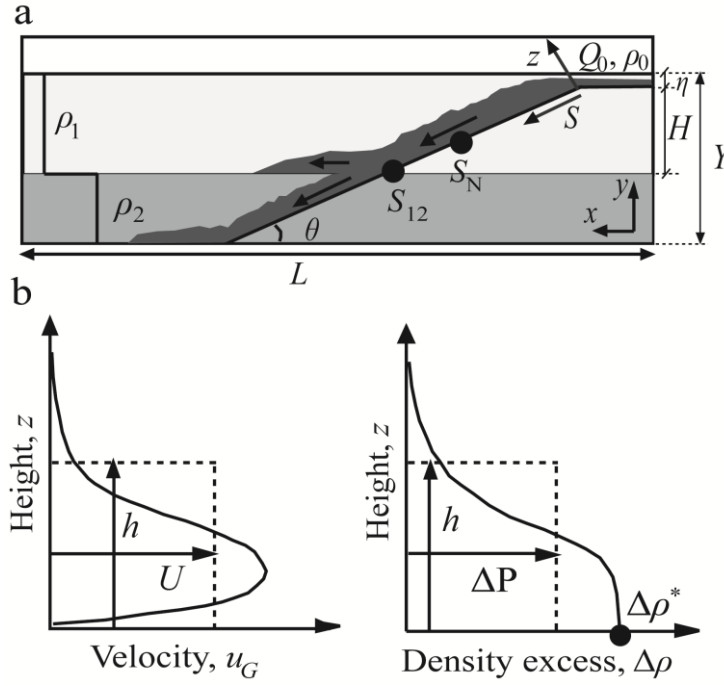


Fig. 2.3. Gravity current entering a two-layered stratified system. (a) Definition of variables in the water body. (b) Velocity $u_G(z)$ and density excess $\Delta\rho(z)$ profiles of the gravity current. The profiles were measured at S_N , before the gravity current reaches the density step $\Delta\rho_{12}$ located at S_{12} . We mark the average variables of the current (h , U , ΔP), and the maximum value of $\Delta\rho(z)$ as $\Delta\rho^*$.

calculated from the average velocity U , thickness h , and reduced gravity G' of the gravity current, as follows,

$$Fr = \frac{U}{(G'h)^{1/2}} \quad (2.2)$$

where $G' = g \Delta P / \rho_1$, and ΔP is the average density excess of the gravity current. If we know the gravity current velocity profile $u_G(z)$ and its density excess profile $\Delta\rho(z)$ ($= \rho(z) - \rho_1$), with maximum value at $z = 0$, i.e., $\Delta\rho^* = \Delta\rho(0)$ (Fig. 2.3b), we can calculate the average thickness h , velocity U and reduced gravity G' as in Ellison and Turner (1959),

$$h = \frac{\left(\int_0^\infty u_G(z) dz \right)^2}{\int_0^\infty u_G^2(z) dz} \quad (2.3)$$

$$U = \frac{\int_0^{\infty} u_G^2(z) dz}{\int_0^{\infty} u_G(z) dz} \quad (2.4)$$

$$G' = \frac{g}{\rho_1} \frac{\int_0^{\infty} \Delta\rho(z) u_G(z) dz}{\int_0^{\infty} u_G(z) dz} \quad (2.5)$$

Observed buoyancy flux portions into the stratified water body - The portion of the buoyancy flux per unit width from a 2D-gravity current that becomes an interflow or an underflow (Fig. 2.1) can be evaluated experimentally from density profiles collected in the tank before, $\rho_{int}(y)$, and after, $\rho_{obs}(y)$, the injection of a given volume of a negatively buoyant fluid in the stratified tank (Fig. 2.4a). The change in ambient buoyancy (g') for a longitudinal area (i.e., $L \times [dy]$) per unit time [$m^3 s^{-3}$] due to an interflow for a specific density step $\Delta\rho_{12}$ will be referred to as $B_1(\Delta\rho_{12})$, and is calculated as,

$$B_1(\Delta\rho_{12}) = \frac{L}{\Delta t} \frac{g}{\rho_1} \int_{[Y-(H+\eta)']}^Y [\rho_{obs}(y) - \rho_{int}(y)] dy = B_0 - B_2(\Delta\rho_{12}) \quad (2.6)$$

In turn, the buoyancy flux per unit width that becomes an underflow, $B_2(\Delta\rho_{12})$, will be calculated as,

$$B_2(\Delta\rho_{12}) = \frac{L}{\Delta t} \frac{g}{\rho_1} \int_0^{[Y-(H+\eta)']} [\rho_{obs}(y) - \rho_{int}(y)] dy = B_0 - B_1(\Delta\rho_{12}) \quad (2.7)$$

Here Y is the total depth of water in the tank, η' is the extra depth from the water surface to the initial depth of the gravity current (Fig. 2.3a), and Δt defines the time interval between the initial and final ambient density profiles (Fig. 2.4a). All other terms have been already defined above. The portions of the inflow buoyancy flux flowing along the density step or along the bottom (b_1 and b_2 , respectively) are given by,

$$b_1(\Delta\rho_{12}) = \frac{B_1(\Delta\rho_{12})}{B_0} \quad (2.8)$$

$$b_2(\Delta\rho_{12}) = \frac{B_2(\Delta\rho_{12})}{B_0} = 1 - b_1(\Delta\rho_{12}) \quad (2.9)$$

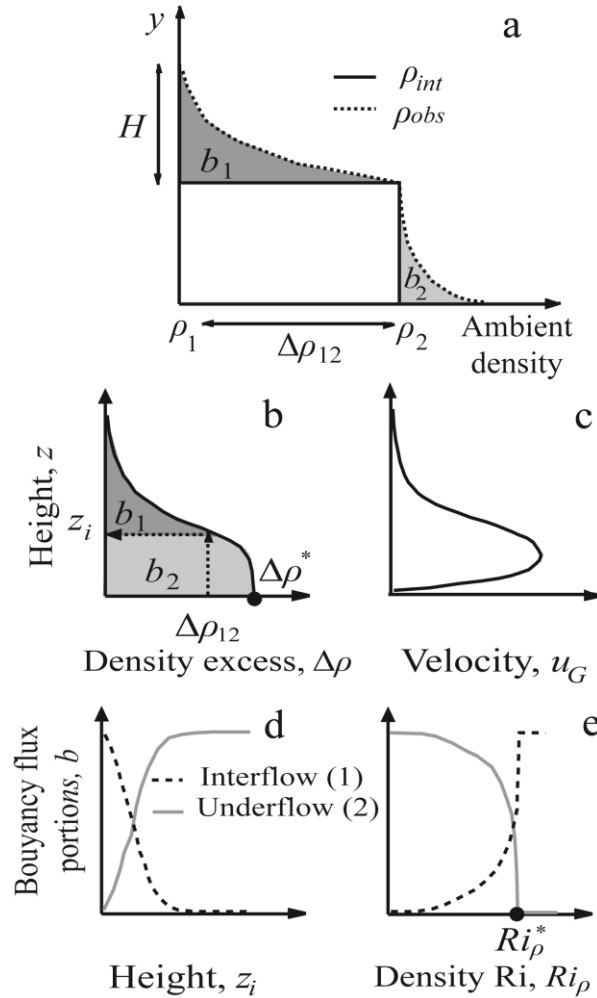


Fig. 2.4. (a) Experimental estimation of buoyancy flux portions at the interflow and the underflow (b_1 and b_2 , respectively) when the gravity current splits due to a density step ($\Delta\rho_{12}$), from the observed initial and final density profiles in the ambient water ($\rho_{int}(y)$ and $\rho_{obs}(y)$, respectively). (b) Density excess profile of the gravity current, $\Delta\rho(z)$. We mark the maximum value, $\Delta\rho^*$. (c) Velocity profile of the gravity current, $u_G(z)$. (d) Predictions of b_1 and b_2 as a function of height, z_i . (e) Predictions of b_1 and b_2 as a function of the density Richardson number, Ri_ρ . We mark the critical value, Ri_ρ^* .

Note that the partitioning of the buoyancy flux between the interflow and the underflow can also be expressed in terms of Ri_ρ , since Ri_ρ is a linear function of $\Delta\rho_{12}$ (Eq. 2.1) when B_0 and H are held constants, as was the case in our experiments.

Predicted buoyancy flux portions from the gravity current profiles - The portions of the inflow buoyancy flux becoming interflows or underflows can be calculated as a function of Ri_ρ and the internal gradients in the gravity current (Fr). Given the velocity and density profiles of the gravity current measured at site S_N (Fig. 2.3b), upstream of the density step located at S_{12} (Fig. 2.3a), the total buoyancy flux per unit width in the gravity current, $B_G(S_N, z)$ [$\text{m}^3 \text{s}^{-3}$], can be calculated as a function of z by integration as,

$$B_G(S_N, z) = \frac{g}{\rho_1} \int_0^z [\rho(S_N, z) - \rho_1] u_G(S_N, z) dz = \frac{g}{\rho_1} \int_0^z \Delta\rho(S_N, z) u_G(S_N, z) dz \quad (2.10)$$

The distance from the sampling site to the density step ($S_{12} - S_N$) is such that: (1) the gravity current develops and reaches normal conditions, with a constant average velocity of the underflow (Ellison and Turner 1959), and (2) the current is not affected by the instabilities created at the density step (Samothrakis and Cotel 2006a). Note that the cumulative buoyancy flux $B_G(S_N, z)$ is maximum, and equal to the inflow buoyancy flux per unit width at the top of the current ($z \rightarrow \infty$), i.e., $B_G(S_N, \infty) = B_0$.

The partition of the buoyancy flux between interflows and underflows can be estimated based upon the density excess $\Delta\rho(z)$ and velocity gradients $u_G(z)$ within the gravity current (Fig. 2.4b,c) as follows. First, we will identify the height z_i within the gravity current profile where its density excess equals to the ambient density step, $\Delta\rho(z_i) = \Delta\rho_{12}$ (Fig. 2.4b). The portion of the buoyancy flux above z_i represents the portion that flows as interflow (b_1) and is calculated as follows,

$$b_1(z_i) = \frac{1}{B_0} \frac{g}{\rho_1} \int_{z_i}^{\infty} \Delta\rho(S_N, z) u_G(S_N, z) dz \quad (2.11)$$

The portion of the buoyancy flux below z_i , in turn, represents the portion that reaches the bottom of the tank and flows as an underflow in layer 2 (i.e., b_2). It is calculated as,

$$b_2(z_i) = \frac{1}{B_0} \frac{g}{\rho_1} \int_0^{z_i} \Delta\rho(S_N, z) u_G(S_N, z) dz = 1 - b_1(z_i) \quad (2.12)$$

Note that the predictions from the integral Eqs. 2.11 and 2.12 require detailed information of density and velocity profiles of the gravity current (Figs. 2.4b,c), and are given in terms of the height z_i (Fig. 2.4d). For any given value of $\Delta\rho_{12}$, one could identify $z = z_i$ such that $\Delta\rho(z) = \Delta\rho_{12}$, and use this procedure to determine the actual portions b_1 and b_2 for that particular scenario. The partitioning of the buoyancy flux (Eqs. 2.11 and 2.12) can also be described in terms of $\Delta\rho(z)$ rather than z_i , given that the density excess profile at the gravity current is a monotonic function of height (Fig. 2.4b). In addition, the non-dimensional number Ri_ρ is a linear function of $\Delta\rho$ (Eq. 2.1), since B_0 and H are considered constant. Hence, we can further express b_1 and b_2 in Eqs. 2.11 and 2.12 as functions of Ri_ρ (Fig. 2.4e). The whole gravity current will penetrate the density step and flow as an underflow (i.e., $b_2=1$) if $Ri_\rho = 0$ (i.e., no density step or homogeneous system). The gravity current will, in turn, become an interflow (i.e., $b_1=1$) when $Ri_\rho > Ri_\rho^*$ (Fig. 2.4e), and thus, when the density step at the ambient water is larger than $\Delta\rho^*$, i.e., $\Delta\rho_{12} > \Delta\rho^*$ (Fig. 2.4b).

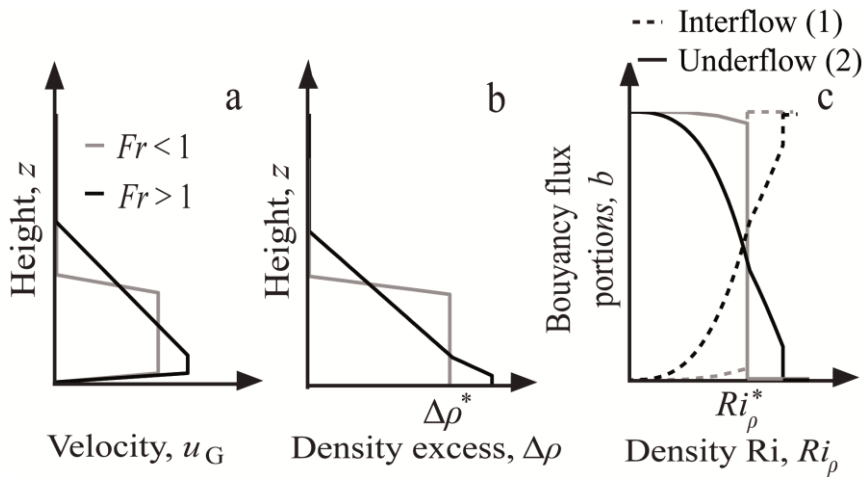


Fig. 2.5. (a) Hypothetical velocity profiles of two gravity currents with different regime: subcritical (gray) and supercritical (black), and (b) the corresponding hypothetical density excess profiles, where the maximum value is $\Delta\rho^*$. (c) Predictions of buoyancy flux portions at the interflow and underflow (b_1 and b_2 , respectively) when the hypothetical gravity currents split at a density step, as a function of the density Richardson number (Ri_ρ). We mark the critical value, Ri_ρ^* .

From Eqs. 2.11 and 2.12, the portion of the buoyancy flux that becomes an interflow or underflow at a sharp density step when the gravity current splits, can be predicted based on the internal gradients within the gravity current. Consider, for example, a subcritical gravity current ($Fr < 1$), with a sharp interface layer and relatively homogenous internal properties (Figs. 2.5a,b – gray lines). In this case, according to Eqs. 2.11 and 2.12, the gravity current would not split (Fig. 2.5c – gray lines). In contrast, one could expect splitting of the gravity current for low values of Ri_ρ if the interface layer at the top of the gravity current is diffuse ($Fr > 1$, Fig. 2.5c – black lines). These results suggest that the portions of the buoyancy flux that flow along or penetrate a density-step (interflow or underflow) are controlled not only by the ambient stratification (Ri_ρ), but also by the internal gradients within the gravity current properties, which in turn, appear controlled by Fr . In the following section we will describe the experiments undertaken to prove this hypothesis.

Methods

Experimental setup - A series of 38 experiments were conducted in a Plexiglas tank, as shown in Fig. 2.6a. The experiments consisted on pumping saline water at a controlled rate down a slope into a two-layered stratified environment. The tank was rectangular in cross section, similar to Wells and Wettlaufer (2007) and Wells and Nadarajah (2009). Inside the tank, an internal channel with side walls was placed at one end. This channel was divided into two parts: first, a horizontal platform, followed by a

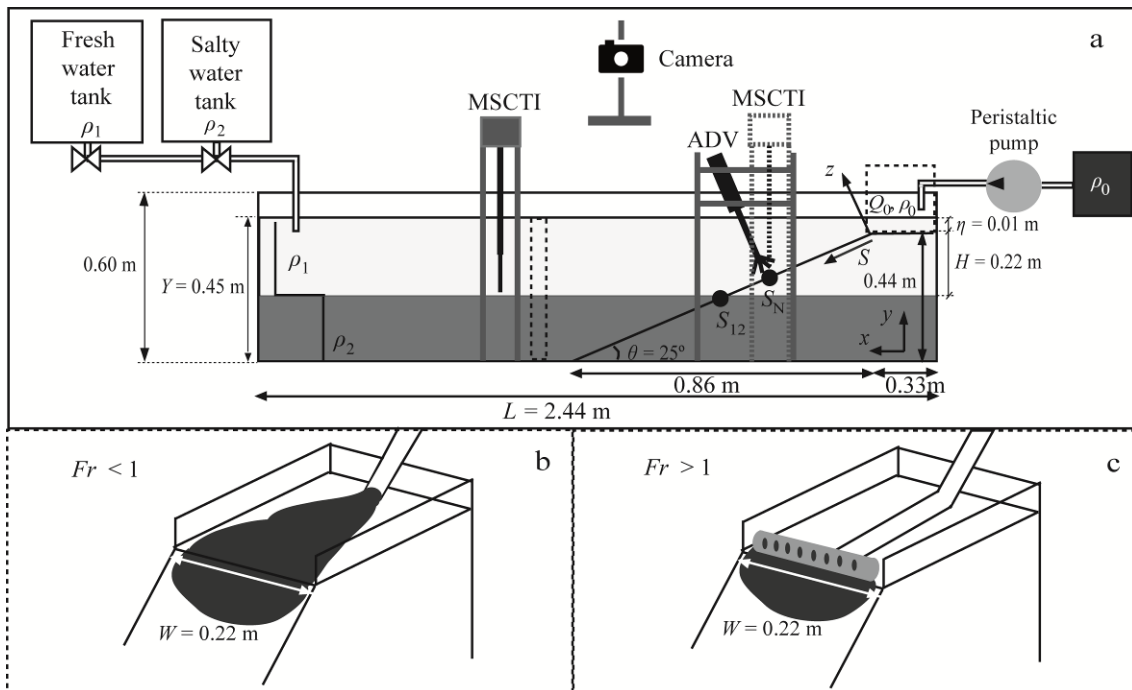


Fig. 2.6. (a) Schematic layout of the experimental setup. The dashed rectangle in the main tank marks the study region to obtain the time slices series. The MSCTI is shown at the two locations where it was placed during the experiments. (b) Releasing mechanism in A-runs (subcritical regime, $Fr < 1$). (c) Releasing mechanism in B-runs (supercritical regime, $Fr > 1$)

sloping section with a slope angle of 25° . Further details of the experimental set up are given in Table 2.1.

The two-layered stratification in the tank was created as follows. Two large containers, of 205-liters each, were initially filled with saline and fresh water (ρ_2 and ρ_1 , respectively) at room temperature of 20°C . To fill the tank, we first added the salty water (ρ_2), and then slowly added the fresh water (ρ_1) on top using a floating diffuser to minimize mixing between the two layers. As a result, the thicknesses of both layers were constant at the beginning of each injection and equal to 0.22 m both at the top layer (H) and at the bottom layer (Table 2.1, Fig. 2.6a). We determined the initial density step at the ambient water $\Delta\rho_{12}$, using a digital MISCO refractometer, model PA202, with a 4 decimal accuracy on the refractive index scales. The refractometer reading was converted to density at 20°C using tabulated data (Weast 1975), also with 4 decimal accuracy in g cm^{-3} .

Once the tank was filled, a 2D-gravity current was created by continuously pumping a saturated saline and dyed solution with a peristaltic pump at the beginning of the internal horizontal platform (Fig. 2.6a). The injection period of each run was ca. 20 minutes. Inflow density (ρ_0), flow rate (Q_0), reduced gravity (g'_0), and buoyancy flux per unit width (B_0) were constant during all the injections (Table 2.1). The density

Table 2.1. Dimensions and initial conditions in the tank, and constant inflow conditions of the experimental two-dimensional gravity currents.

Variable	Units	Value
<i>Tank dimensions</i>		
length	m	2.5
width	m	0.3
depth	m	0.6
<i>Internal channel dimensions</i>		
Horizontal platform		
length	m	0.33
width	m	0.22
depth	m	0.44
Sloping section		
length	m	1.00
width	m	0.22
<i>Initial conditions in the tank</i>		
Density of the fresh water, ρ_1	kg m ⁻³	998
Total water column depth, Y	m	0.45
Extra depth surface-inflow, η'	m	0.01
Thickness of the top layer, H	m	0.22
Thickness of the bottom layer	m	0.22
<i>Inflow conditions (constant)</i>		
Inflow density, ρ_0	kg m ⁻³	1,199
Inflow rate, Q_0	m ³ s ⁻¹	8.57 x 10 ⁻⁶
Inflow reduced gravity, g'_0	m s ⁻²	1.97
Inflow buoyancy flux per unit width, B_0	m ³ s ⁻³	7.68 x 10 ⁻⁵

Richardson number (Ri_ρ , Eq. 2.1), was experimentally varied by changing the density of the lower layer ρ_2 , while fixing the density of the upper layer ρ_1 . The experimental values of $\Delta\rho_{12}$ and Ri_ρ for each run are shown in Table 2.2.

We conducted two sets of experiments (A and B) with similar values of $\Delta\rho_{12}$, but using two different release mechanisms (Figs. 2.6b and 2.6c; Table 2.2). The injection device in the A-experiments consisted of a plastic tube of 5 mm diameter placed at the beginning of the horizontal platform, which allowed the saturated solution to spread uniformly along the internal channel width since the beginning of the slope (Fig. 2.6b). In the B-experiments, the saline solution was injected through a diffuser placed at the beginning of the slope, and covering the whole width of the internal channel (Fig. 2.6c). As a result of the two different injection devices, we were able to generate gravity currents with different velocity and density profiles. Downstream the inflow-section (see *Results*), the gravity current was sub-critical ($Fr < 1$) in the A-experiments, but supercritical ($Fr > 1$) in the B-experiments.

Table 2.2. Experimental specifications of A- (subcritical, $Fr < 1$) and B- (supercritical, $Fr > 1$) runs (Fig. 2.6b, 2.6c). Ambient water density profiles were measured only in the runs marked in bold. Photos were taken in all runs.

Sub-critical, $Fr < 1$			Supercritical, $Fr > 1$		
Run	$\Delta\rho_{12}^a$ (kg m^{-3})	Ri_ρ^b	Run	$\Delta\rho_{12}^a$ (kg m^{-3})	Ri_ρ^b
A-1	64.60	77.34	B-21	66.29	79.36
A-2	56.70	67.88			
A-3	51.93	62.17			
A-4	45.88	54.92	B-22	38.33	45.89
A-5	34.28	41.03	B-23	32.30	38.67
A-6	33.30	39.86	B-24	28.00	33.52
A-7	29.00	34.72	B-25	24.30	29.09
A-8	25.30	30.29	B-26	24.01	28.74
A-9	21.70	25.98	B-27	20.70	24.78
A-10	24.28	29.07	B-28	17.90	21.43
A-11	18.90	22.63	B-29	17.05	20.41
A-12	13.80	16.52	B-30	12.80	15.32
A-13	15.69	18.78	B-31	9.30	11.13
A-14	10.30	12.33	B-32	8.89	10.64
A-15	9.03	10.81	B-33	6.40	7.66
A-16	7.40	8.86	B-34	5.32	6.37
A-17	6.15	7.36	B-35	3.80	4.55
A-18	4.50	5.39	B-36	3.50	4.19
A-19	2.40	2.87	B-37	1.40	1.68
A-20	0.00	0.00	B-38	0.00	0.00

^a $\Delta\rho_{12}$ – Density difference at the density step.

^b Ri_ρ – Density Richardson number.

Instruments - Sequences of photographs of the two-layered tank were taken in each experiment with a frequency of 5 s during the 30 minutes after the beginning of the injection (ca. 360 photos per run), using a digital camera placed on a tripod. From those photographs we extracted vertical image slices at $x = 1.3$ m (Fig. 2.6a, dashed rectangle). We will refer to these montages of image slices as ‘time slices series’, which show the increase in thickness of the intrusion(s) into the stratified system over time.

Velocity profiles within the gravity current were measured at a site 0.20 m upstream of the density step located at $S_{12} = 0.52$ m (i.e., $S_N = 0.32$ m), using a Nortek Vectrino-II Acoustic Doppler Velocimeter (ADV) (Fig. 2.6a). The Vectrino-II ADV consists of one transmitter and four receivers which are slanted at 30° from the axis of the transducer. Unlike older ADV units, this newer unit is able to measure all 3 velocity components at 30 locations simultaneously, at 30-80 mm from the transducer head. The ADV was placed at the center of the slope at S_N and $z = 7$ cm, giving velocity profiles

with 1 mm vertical resolution between $z = 0$ cm and $z = 3$ cm, and a frequency of 50 Hz. To ensure a good data acquisition, the axis of the probe was normal to the slope (Alex Hay, personal communication). Representative velocity values of the downward velocity component (U_S) were obtained after two post-processing tasks undertaken in the following order: first, we filtered the velocity fluctuations of a raw measured time series during a period of 3 minutes (starting when the head of the current passed the instrument) by using windows of 5 s; and then, we averaged the filtered 1800 values to obtain the representative velocity profile.

Vertical density profiles within the gravity current were measured at the same location as the velocity profiles, using a MicroScale Conductivity and Temperature Instrument (MSCTI), model 125 manufactured by PME, Inc (Fig. 2.6a). This instrument is designed to measure two analog voltage outputs (range of ± 5 V) of ionic solutions at a frequency of 20 Hz, which are converted to electrical conductivity ($S\ cm^{-1}$) and temperature ($^{\circ}C$) according to internal calibration equations. The readings of temperature and conductivity were used to estimate density following the polynomial equations described by Ruddick and Shirtcliffe (1979). The MSCTI was attached to a traversing stage which allowed the probe to move vertically with a speed of $1\ cm\ s^{-1}$, which yielded a vertical resolution of 0.05 mm for the resulting density profile over the range from 0.3 cm to 3 cm above the bottom. As a result, vertical density excess profiles at the gravity current in the y -axis $\Delta\rho(y)$ ($=\rho(y) - \rho_1$) were gathered, instead of the z -axis as the velocity profiles. The characteristic density excess profile of each study gravity current was obtained by averaging ca. 9-10 downward profiles measured over a period of ca. 10 minutes after the head of the gravity current passed the instrument. It is important to notice that the characteristic density excess profile in a layer of 3 mm right above the sloping bottom was extrapolated from the observations, given that the density measurements close to the wall were not feasible without destroying the glass conductivity probe. We followed the Ellison and Turner (1959) laboratory observations, and used two different functions to estimate the density profile within these 3 mm. An exponential function was fitted to the observations, and used to extrapolate the density measurements to a height above the bottom where the velocity was about half its maximum value. An error function was then used to fill the data gap between that height of half-maximum velocity and the bottom. The extrapolated density excess profiles were forced to satisfy two conditions. First, the maximum value of the gravity current density excess ($\Delta\rho^*$, at the bottom) should be equal to the density step $\Delta\rho_{12}$ associated with the critical $Ri\rho^*$, for which a pure interflow ($b_1 = 1$) was observed in each set of experiments (Figs. 2.4b,e). Second, the total buoyancy flux per unit width in the gravity current at the measurement site equaled its inflow value at the release point ($B_0 = 7.68 \times 10^{-5}\ m^3\ s^{-3}$), so that buoyancy flux is conserved.

Finally, we measured a set of 30 downward density profiles of the complete (i.e., $Y = 0.45$ m) ambient water column at the end of the slope ($x = 1.5$ m, Fig. 2.6a, probe in

solid line) during the 20 minutes duration of each run. We will use the initial ambient density profile and the one measured after ca. 7 minutes from the beginning of the injection of dyed water ($\rho_{int}(y)$ and $\rho_{obs}(y)$, respectively), to quantify the portions b_1 and b_2 (Eqs. 2.8 and 2.9) when the 2D-gravity current splits at the density step. After that interval $\Delta t = 7$ min, the oscillations in the base of the top layer generated at the time when the gravity current hits the density step had vanished, and the filling box dynamics described by Wells and Wettlaufer (2005) had not significantly changed the initial depth of the top layer, H . Note that the addition of colored dyes to the gravity current showed that the density layers were almost flat during each experiment (Wells and Wettlaufer 2005), so the observed buoyancy flux portions would not have varied if we had measured $\rho_{obs}(y)$ at other location within the tank.

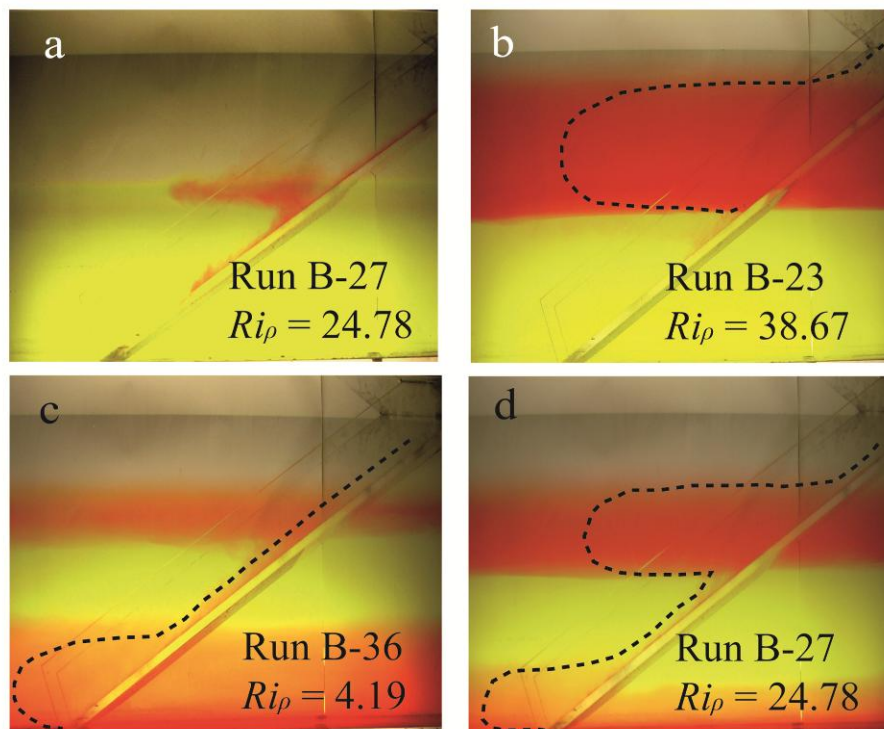


Fig. 2.7. Photographs of the central 1 m-length section of the tank (Fig. 2.6a) during different runs with supercritical regime. Photo (a) was taken after 0.5 min of injection and (b-d) after 7 min. We observe the actual splitting of the gravity current in (a), interflow in (b), underflow in (c) and split flow in (d). The dashed lines mark the predominant pathways of the gravity current.

Results

Fig. 2.7 includes photographs from different experiments, with the gravity current exhibiting the three different behaviors shown in Fig. 2.1. Fig. 2.7a, in particular, shows a gravity current splitting as it reaches the density step. Part of the dyed current flows along the density step, and another part penetrates and flows downwards along the slope on the second bottom layer. The whole gravity current separated from the bottom at the base of the top layer (interflow) when the two-layered system was characterized by high Ri_ρ values (Fig. 2.7b and 2.1a). For low values of Ri_ρ , the majority of the current penetrated the density step and flows along the bottom as an underflow (Fig. 2.7c and 2.1b). Note also that there is a small portion of the gravity current that forms an interflow, even for low Ri_ρ . This could be the result of turbulent motions that develop at the base of the top layer as soon as the gravity current hits the density step (Samothers and Cotel 2006a). Finally, the flow splits for intermediate values of Ri_ρ , so that a portion of the gravity current flowed along the base of the top layer (interflow) and the remaining portion penetrated the density step to flow along the bottom (underflow) (Fig. 2.7d and 2.1c).

Changes in ambient stratification- Time slices series from experiments with different Ri_ρ and Fr are shown in Fig. 2.8. In both set of runs, we observed thicker interflows for larger values of Ri_ρ (compare, for example, Figs. 2.8a and 2.8c). Note that, in general, thicker interflows also developed in response to gravity currents with $Fr > 1$, compared to currents with $Fr < 1$, for similar values of Ri_ρ (compare, for example, Figs. 2.8e and 2.8b). The underflows, in turn, tended to have similar thickness in both regimes. Only for the highest Ri_ρ tested, the underflows generated by subcritical gravity currents were slightly thicker (Figs. 2.8a and 2.8d). Again, a small portion of the gravity current forms an interflow even for low Ri_ρ (Figs. 2.8c and 2.8f). The observed thickness of inter- and underflows can be used to predict the partitioning of the volume flux along the gravity current between the two intrusions at the density step. These results are included in the Appendix (*Volume flux partition*). Here we focus on the partitioning of the buoyancy flux.

In Fig. 2.9 we have plotted ambient water density profiles at the beginning, $\rho_{int}(y, t = 0 \text{ min})$, and at the end, $\rho_{obs}(y, t \sim 7 \text{ min})$, of different experiments. The differences between the two profiles at the density step or the bottom of the tank are indicative of the buoyancy fluxes per unit width flowing as interflow or underflow, $B_1(\Delta\rho_{12})$ and $B_2(\Delta\rho_{12})$ (Eqs. 2.6 and 2.7, respectively). Note that the changes in the ambient density profiles at the density step are more pronounced for larger Ri_ρ (compare Fig. 2.9d with 2.9f). This suggests again that the portion of the inflow buoyancy flux per

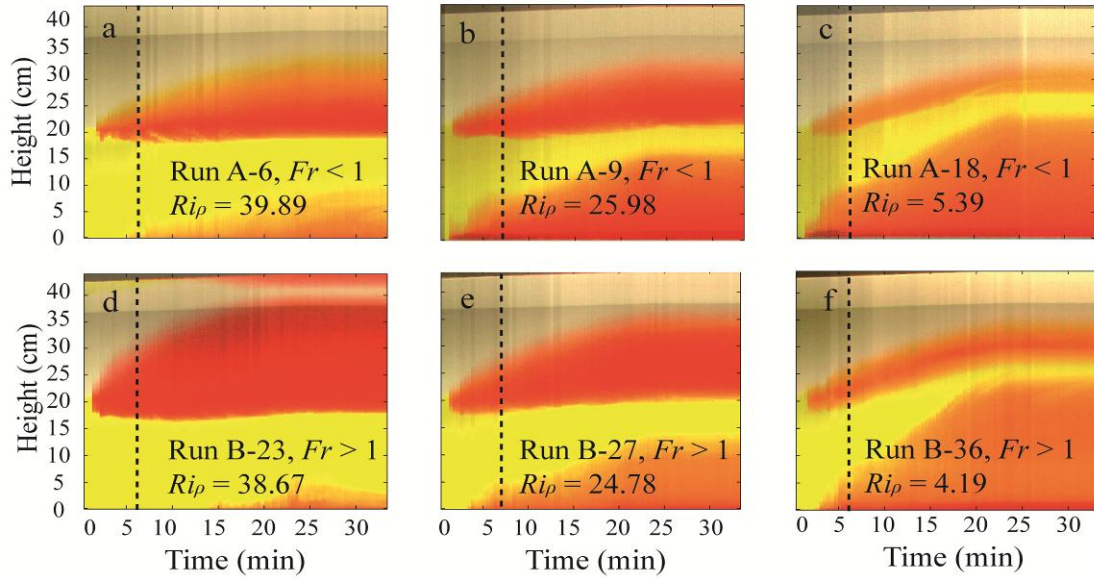


Fig. 2.8. Time slices series during different experiments (Table 2.2). The dashed line marks 7 min after the beginning of the injection

unit width added to the top layer tended to be larger for higher Ri_ρ . As Ri_ρ decreases, in turn, the buoyancy flux flowing into the bottom layer tended to increase (from Fig. 2.9a to 2.9c). The differences between the initial and final density profiles were also sensitive to changes in the release mechanisms, suggesting that the partition of the buoyancy

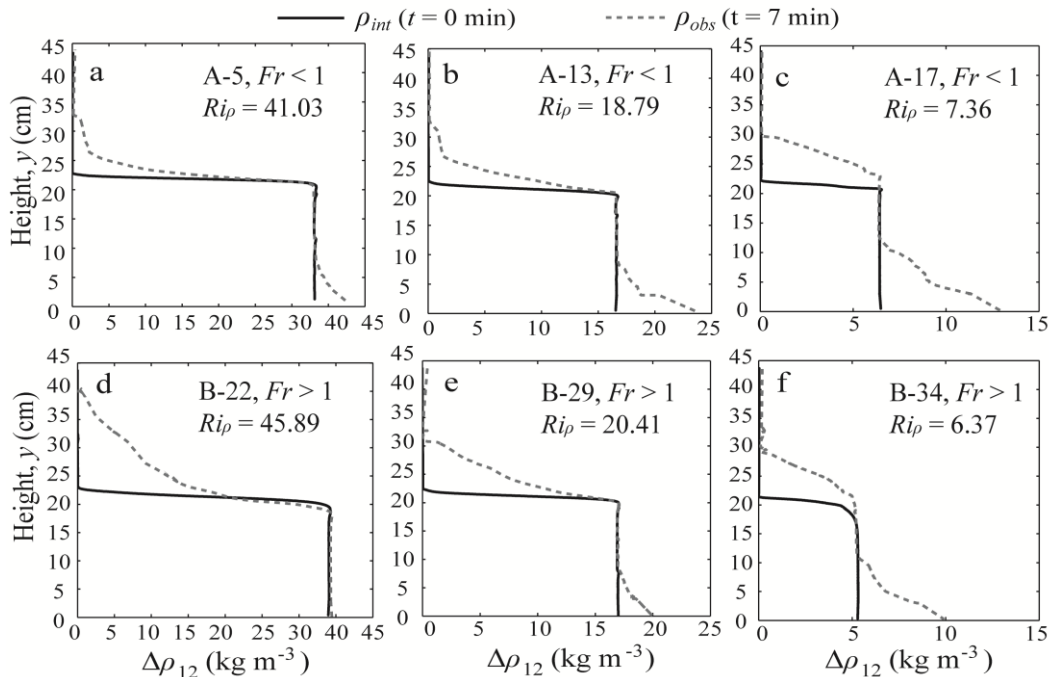


Fig. 2.9. Ambient water density profiles before the gravity current injection (ρ_{int}) and after ca. 7 min since the beginning of the injection (ρ_{obs}), gathered with the MSTCI at $x = 1.5$ m in the experimental tank (Fig. 2.6a) during different experiments (Table 2.2).

fluxes at the density step varied not only as a function of Ri_ρ , but also depending on Fr . In general, the buoyancy flux per unit width added to the top layer (B_1) was larger for gravity currents with $Fr > 1$ compared with gravity currents with $Fr < 1$, for similar values of Ri_ρ (compare Fig. 2.9d and 2.9a, for example).

Velocity and density gradients in the gravity currents - Time-averaged velocity and density excess profiles in the S - z reference system are shown in Fig. 2.10 for the A- and B- series of experiments. The measured vertical density profile $\rho(y)$ was multiplied by the cosine of the bottom slope and converted to $\rho(z)$ in order to use the

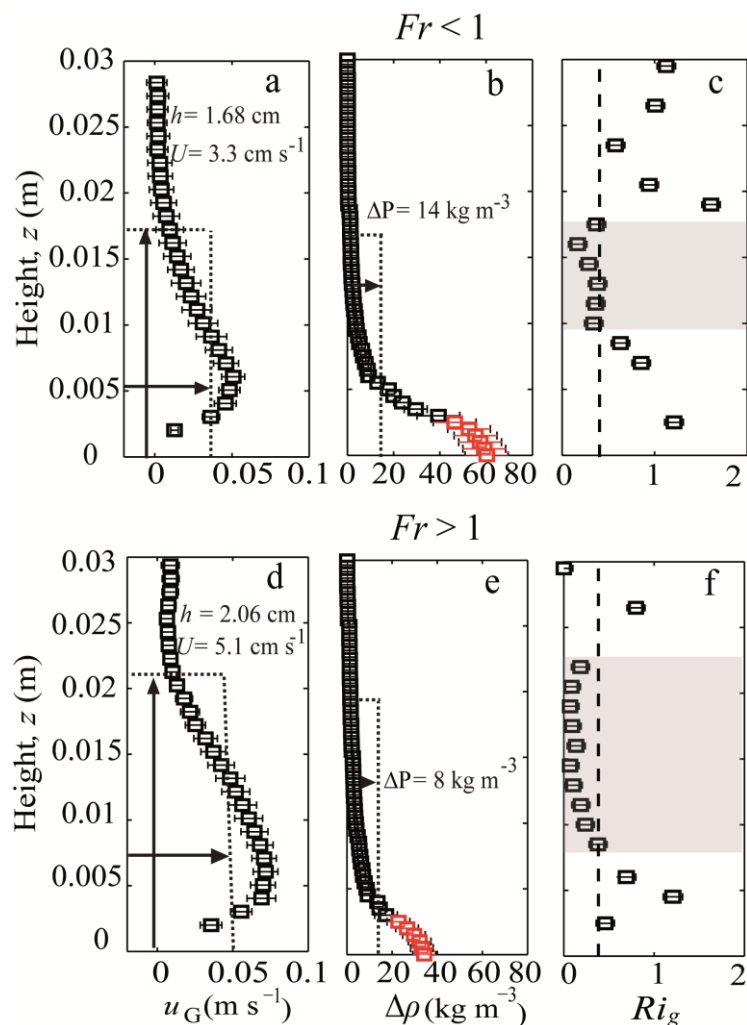


Fig. 2.10. Experimental profiles of the two gravity currents, with subcritical ($Fr < 1$, a-c) and supercritical ($Fr > 1$, d-f) regimes. All profiles are referred to the S - z reference system and measured at S_N (Fig. 2.6a). The average values of thickness, velocity and density excess (h , U , ΔP) are shown above. Error bars mark the standard deviation of the observed variables over the study period. (a, d) Velocity profile, $u_G(z)$. (b, e) Density excess profile, $\Delta\rho(z)$. The red points are an extrapolation of the profile in order to conserve the inflow buoyancy flux per unit width. (c, f) Gradient Richardson number (Ri_g) where the dashed line marks the critical value, $Ri_g = 0.25$, and the shaded rectangle marks interface layer at the top of the current.

same reference system as the velocity measurements (i.e., S - z axis, Fig. 2.6a). Note that we mark in red the extrapolated part of the density excess profiles of the gravity currents in Figs. 2.10b,e. According to our results, the critical Ri_ρ^* values were 75 for the A-experiments and 42 in the B-experiments (see Fig. 2.11 in *Discussion*), which we used in the second criteria of our extrapolation procedure. The resulting velocity and density excess profiles of our observed gravity currents were very similar to those measured by Ellison and Turner (1959) under similar conditions of bottom slope, and current density and velocity (compare their Fig. 4 with our Fig. 2.10).

We estimated that Fr was 0.69 (subcritical) in the A-experiments, and 1.31 (supercritical) in the B-experiments. The time-averaged velocity and density excess profiles in the A- and the B-experiments (Figs. 2.10a,b and 2.10d,e, respectively) exhibited differences, which were consistent with those shown in Fig. 2.2 for $Fr < 1$ and $Fr > 1$. First, the supercritical gravity current exhibited larger values of average thickness h and velocity U , but lower average density excess ΔP . Also, gradients in the density excess profiles tend to be sharper in the A-experiments ($Fr < 1$), while the current-ambient interface layer is more diffuse and thicker for the supercritical flows, consistent with previous reports (Odier et al. 2009).

We estimated the gradient Richardson number, $Ri_g(z)$, from the profiles shown in Fig. 2.10, as $Ri_g(z) = [g (d\rho(z)/ dz)] / [\rho_G (du_G(z)/ dz)^2]$, where ρ_G is the average density of the current. Values of $Ri_g < 0.25$ were observed above the velocity maxima in our profiles (Figs. 2.10c and 2.10f), which suggest the presence of an active mixing layer between the current and the ambient water (Strang and Fernando 2001). This mixing layer at the current-ambient water interface (i.e., interface layer), with $Ri_g < 0.25$, was about twice as thick in the B-experiments, with $Fr > 1$, compared to the interface layer in the A-experiments, with $Fr < 1$ (18 mm and 8 mm, respectively). These results suggest that turbulent mixing is more energetic in supercritical gravity currents, as reported by Turner (1986). No roll waves were observed at the top interface layer of the currents, since Reynolds number in our experiments was $Re > 500$ ($\nu = 10^{-6} \text{ m}^2 \text{ s}^{-1}$), compared to the lower Reynolds number experiments of Cenedese et al. (2004). We calculated the entrainment coefficients at the interface layer from changes in the average gravity current thickness h , between the beginning of the inflow channel and S_N , as $E = \Delta h / \Delta S$ (Ellison and Turner 1959). The average thickness h was 2.06 cm and 1.68 cm in the A- and B-experiments, respectively. Their ratio was 1.22. The entrainment coefficient (E) was 0.0054 in the A-experiments ($Fr < 1$), almost 20% smaller than the same estimates for the B-experiments, with supercritical currents ($E = 0.0066$). These values are in the range of those found by Ellison and Turner (1959) in their experiments with gravity currents of similar densimetric values of Fr and slope angles.

Discussion

Observed and predicted buoyancy flux portions - The partitioning of the buoyancy flux (b_1 and b_2) at the density step estimated from the velocity and density profiles within the gravity current (Fig. 2.10), using Eqs. 2.11 and 2.12, compares well to the portions calculated with Eqs. 2.8 and 2.9 using the observed density profiles in the tank before and after the injection (see Fig. 2.11). The differences can be partly due to the fact that the velocity and density profiles were collected not at the density step but 0.2 m upstream. The gravity current will entrain additional ambient water before reaching the density step, and consequently the profiles at S_{12} will differ from those at the sampling site, S_N . The maximum density excess ($\Delta\rho^*$), for example, will be lower at S_{12} compared to the observed values at S_N . The two profiles, though, can be assumed self-similar in velocity terms, given that the current flows under normal conditions (Sequeiros et al. 2010). Hence, one can estimate the profiles at S_{12} based on the information available at S_N . We used Eqs. 3, 6, and 10 from Wells and Wettlaufer (2007) to estimate the reduction of the gravity current density excess at S_{12} ,

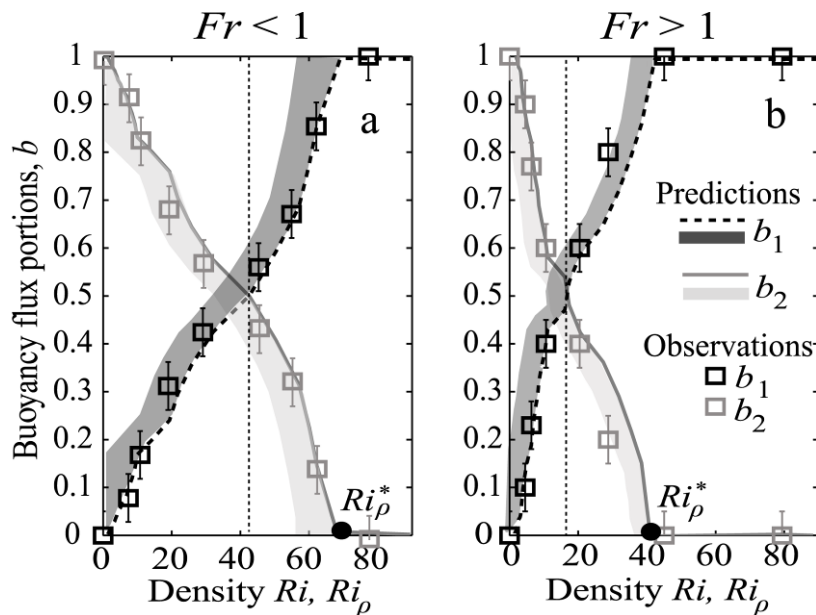


Fig. 2.11. Predictions (lines) and experimental results (symbols) of buoyancy flux portions as a function of the density Richardson number (b versus Ri_ρ), from the experimental (a) subcritical gravity current ($Fr < 1$), and (b) supercritical gravity current ($Fr > 1$) entering the two-layered system (Fig. 2.10). The black dot marks the critical value of Ri_ρ^* and the thin dashed line marks the $Ri_\rho[0.5]$ for each regime. The shaded regions show the range of predicted values of b due to the error introduced by neglecting additional entrainment of ambient water before the gravity current reached the density step (Fig. 2.6a).

using the entrainment coefficients E calculated in the results section and density profiles in Figs. 2.10b, e. As a result, Ri_ρ^* could be ca. 12-15% lower than estimated based on the profiles collected at S_N , and the predictions from Eqs. 2.11 and 2.12 would be still in good agreement with the estimates from Eqs. 2.8 and 2.9 (see shaded black and gray regions in Fig. 2.11).

Note that the value of Ri_ρ for which 50% of the buoyancy flux per unit width in the gravity current becomes an interflow, $Ri_\rho[0.5]$, is lower in the case of supercritical gravity currents, compared to the gravity currents flowing with $Fr < 1$ (Fig. 2.11). This will be also the case for the critical Ri_ρ^* required for a pure interflow (i.e., $b_1(Ri_\rho^*) = 1$). These results suggest that splitting of gravity currents in a two-layered stratified system with a weak density step is more likely to occur for gravity currents exhibiting a diffuse and thick interface layer, associated with larger densimetric Froude number as in the supercritical regime ($Fr > 1$), compared to other gravity currents with a more sharp and thinner interface layer, when $Fr < 1$.

Application to the field - To determine whether the current splits or not into multiple intrusions in field scale settings, it may be more appropriate to analyze the local conditions prevailing at the point where the gravity current meets the sharp density step, rather than by considering the inflow conditions, as in Eq. 2.1. This is because many field gravity currents are not purely two dimensional, and there may be additional mixing at, for example, the initial plunge zone where a cold river enters a stratified lake. Wallace and Sheff (1987) defined the stability of the stratification in terms of local conditions (herein after, transition Richardson number, Ri_{12}) as a density differences ratio between the density step in the ambient water ($\rho_2 - \rho_1$), and the average density excess of the gravity current at the base of the top-layer ($\rho_G - \rho_1$). In a similar way as for Ri_ρ , there exists a critical value of Ri_{12} (Ri_{12c}), for which part of the gravity current flowing into the density step would leak to the bottom, as an underflow (i.e., split flow, Fig. 2.1c). According to our definition of Ri_{12} , we expect $Ri_{12c} \approx 1$, given that the gravity current will only penetrate through a density step (underflow) when it is denser than the underlying fluid, i.e., $(\rho_G - \rho_1) > (\rho_2 - \rho_1)$, or alternatively for $Ri_{12} < 1$. For $Ri_{12} \geq 1$, the gravity current will have entrained sufficient ambient water after falling a depth H , so that its average density ρ_G could be close to ρ_2 , and thus, a portion (or the whole) gravity current will detrain at the base of the top layer (split- or inter-flows, Figs. 2.1c and 2.1a, respectively). This concept of Ri_{12} was recently applied in field observations (Cortés et al. 2014a) and shows good agreement with the regimes illustrated in Fig. 2.1.

As it is often in natural systems, Cortés et al. (2014a) observed field ambient density profiles characterized by thick linearly-density stratified metalimnetic layers (see their Fig. 1.5). Laboratory experiments undertaken by Flynn and Sutherland (2004) and Wells and Nadarajah (2009) identified that the intrusion depth of a current entering

a continuously-density stratified water column is a function of the buoyancy frequency (N) in the ambient water. Therefore, we suggest as a future line of research, to adapt our theory and undertake a similar set of experiments but in linearly-density stratified water columns, in order to evaluate our model under more realistic conditions.

Application of the theory: b_1 as a function of Fr and Ri_ρ - The portion of buoyancy flux that separates from a gravity current at a sharp density step (b_1) can be predicted from Eq. 2.11, if the velocity and density profiles of the current are known. The density and velocity profiles in this work are similar to those of the seminal experiments of Ellison and Turner (1959), but they do not necessarily have the same shape as large field scale gravity currents, where increased turbulence due to enhanced bottom roughness leads to a more highly mixed lower layer (Fig. 2.2). Sequeiros (2012) recently argued that the velocity and density profiles in large scale gravity currents can be estimated from their densimetric Froude numbers. He proposed empirical relationships based on a total of 31 field observations (his Table 1) to estimate the current thickness, maximum velocity and density excess, and other characteristic parameters of the current profiles, based on Fr (see his Eqs. 23 to 27). He further proposed two dimensionless velocity and density excess profiles for subcritical and supercritical gravity currents, which were in good agreement with experimental data

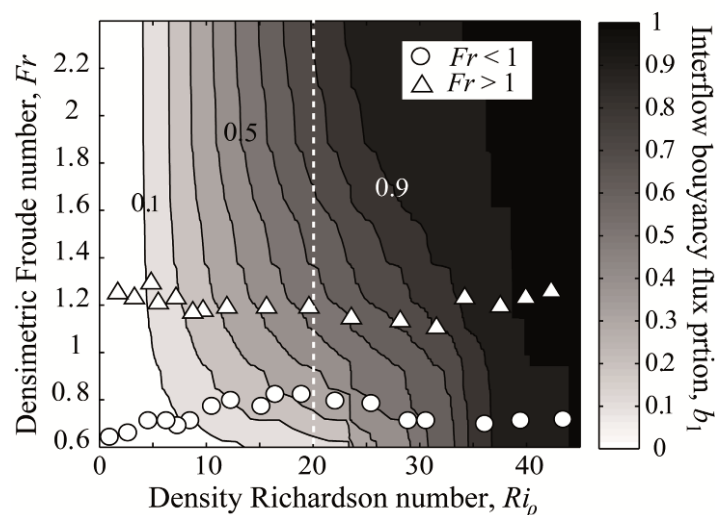


Fig. 2.12. Application results: predicted interflow buoyancy flux portions of the inflowing current (b_1) as a function of the density Richardson number (Ri_ρ) for different densimetric Froude numbers (Fr) of theoretical gravity currents [Sequeiros, 2012]. Values of b_1 along the white dashed line at $Ri_\rho = 20$ are commented in the text. We also mark with symbols (circles and triangles) the predicted portions of b_1 for the two gravity currents observed in our lab experiments.

of saline gravity currents from Sequeiros et al. (2010). Here, we have followed Sequeiros (2012) to build dimensional $u_G(z)$ and $\Delta\rho(z)$ profiles (*see* his Fig. 2.4 and our Fig. 2.3b). Using these theoretical gravity current profiles, the portion of the buoyancy flux separating at a sharp density step (b_1) was estimated following Eq. 2.11. In this exercise, we assumed a depth H ten times higher than the average thickness within the gravity current h , as was the case in our experiments. The results of this exercise are shown in Fig. 2.12 for a range of Fr , close to 1, and a range of Ri_ρ .

For any value of Fr , the results shown in Fig. 2.12 suggest that almost the whole current penetrates the density step to form an underflow when $Ri_\rho < 5$ ($b_1 \sim 0$). For $Ri_\rho > 40$, the whole current flows along the base of the top layer as an interflow ($b_1 = 1$). Hence, the ranges of critical density Richardson numbers (Ri_ρ^*) are similar to the range of critical values encountered in our laboratory experiments ($Ri_\rho^* \sim 5-40$). In addition, our predictions of b_1 for the two laboratory Fr values (i.e., 0.69 and 1.31) are in good agreement with the predictions inferred from the theoretical gravity current profiles that we built from Sequeiros' work (dots and squares in Fig. 2.12). For Ri_ρ in the critical range, the portion of buoyancy flux that flows as interflow appears to vary in Fig. 2.12 depending on the Fr , and thus, the internal gradients within the gravity current. For example, when $Ri_\rho = 20$, b_1 range between 0.3 and 0.8 when the Fr varies between 0.6 and 2.1. These are values of Fr typically found in the field, which suggest that realistic gravity currents could display the dynamic we have sketched in Fig. 2.1c of split flows.

Conclusions and implications

We have demonstrated that the splitting of a gravity current at a density step in a two-layered stratified system depends on two non-dimensional numbers: a Richardson number (Ri_ρ) which represents the effect of the density step in the basin; and the densimetric Froude number (Fr) which controls the internal gradients of the gravity current. The stream-tube paradigm presented in many textbooks and previous studies (Smith 1975; Fischer et al. 1979; Price and Baringer 1994; Dallimore et al. 2001) as a model for gravity currents, which assumes that flow properties are invariant below the interface with the ambient water, cannot explain the process of splitting of negatively buoyant flows in two-layered stratified environments. The splitting process may be more common than single intrusions, but being able to detect them will require the collection of high-resolution field observations, or even using conservative/artificial tracers released during short periods of time to explicitly identify multiple intrusions. Our experiments suggest that an alternative approach could be used to determine whether or not splitting of a gravity current occurs downstream, and to quantify the

partitioning of the buoyancy flux between inter- and under-flows. This approach, though, requires detailed information of the internal structure of the gravity current.

Appendix: Volume flux partition

The field work undertaken by Cortés et al. (2014a) motivated us to quantify the partition of a gravity current at the density step of a stratified water body ($\Delta\rho_{12}$) in terms of the buoyancy flux of the current (B_G). However, there may be other situations in which the volume flux of the current (Q_G) could be the variable of interest. As a result, in this document we again compare our experimental observations with a theory, but now we quantify the portions of the volume flux from the gravity current that go into each layer when it hits the density step of a two-layered system. This work is organized as follows. First, we introduce a theory to describe how a gravity current will be split at a sharp density step, and determine the volume flux portions that intrude into the two layers based upon the density and velocity profiles of the gravity current (Fr) and the strength of the ambient density step (Ri_ρ). We already described the methodology of the experimental runs. Then, we present the main observations regarding inflow/underflow volume fluxes in terms of thickness from time slices series. Finally, we relate our laboratory results with the already presented theory.

Observed volume flux portions into the stratified water body - The volumetric fluxes in the interflow and underflow can be evaluated from measurements taken in the ambient water after the injection of a given volume of negatively buoyant fluid. In this work, these calculations are done from measurements of the thickness of the interflow in the water column (h_1) taken shortly after a traced gravity current has reached the density step and before re-entrainment has become important. In addition, we define h^* as the thickness of the interflow when there is no underflow. As a result, we can define the thickness of the underflow as ($h^* - h_1$) without considering entrainment at the lower layer. According to this, we estimate the corresponding values of volume fluxes at the interflow and underflow for a specific density step ($Q_1(\Delta\rho_{12})$ and $Q_2(\Delta\rho_{12})$, respectively) as follows,

$$Q_1(\Delta\rho_{12}) = \frac{L \times W \times h_1}{\Delta t} \quad (2.A1)$$

$$Q_2(\Delta\rho_{12}) = \frac{L \times W \times (h^* - h_1)}{\Delta t} \quad (2.A2)$$

Note that Δt defines the time after the beginning of the injection when we measured the thickness of the interflows, h_1 . The rest of variables have been already described.

Therefore, volume flux portions which flows as interflow or underflow (q_1 or q_2) are calculated either from the volume flux Q_G in the gravity current (Eq. 2.A5), or from h^* , as follows,

$$q_1(\Delta\rho_{12}) = \frac{Q_1(\Delta\rho_{12})}{Q_G} = \frac{h_1}{h^*} \quad (2.A3)$$

$$q_2(\Delta\rho_{12}) = \frac{Q_2(\Delta\rho_{12})}{Q_G} = 1 - \frac{h_1}{h^*} = 1 - q_1(\Delta\rho_{12}) \quad (2.A4)$$

Note that the partitioning of the volume flux between the interflow and the underflow can also be expressed in terms of Ri_ρ (Eq. 2.1). Our series of experiments with different density steps $\Delta\rho_{12}$ allowed us to determine the functions $q_1(Ri_\rho)$ and $q_2(Ri_\rho)$. We again want to test our hypothesis of that these portions not only depend on the stratification conditions in the ambient water (Ri_ρ), but that they may also change depending on the internal properties of the gravity current (Fr).

Predicted volume flux portions from the gravity current profiles - Similarly to the buoyancy flux in the gravity current, we can define a cumulative volume flux at a given distance S_N from the source line (Fig. 2.3a), and any given distance from the bottom z , as,

$$Q_G(S_N, z) = W \int_0^z u_G(S_N, z) dz \quad (2.A5)$$

Due to entrainment of overlying fluid into the gravity current, the volume flux at the top of the current ($z \rightarrow \infty$), is much larger than the inflow value, i.e., $Q_G(S_N, h) > Q_0$.

The portion of the volume flux in the gravity current becoming an interflow or an underflow (q_1 and q_2 , respectively) can also be calculated from the velocity profile $u_G(S_N, z)$ and the height z_i (Fig. 2.A1a-c) as,

$$q_1(z_i) = \frac{W}{Q_G} \int_{z_i}^{\infty} u_G(S_N, z) dz = 1 - q_2(z_i) \quad (2.A6)$$

$$q_2(z_i) = \frac{W}{Q_G} \int_0^{z_i} u_G(S_N, z) dz \quad (2.A7)$$

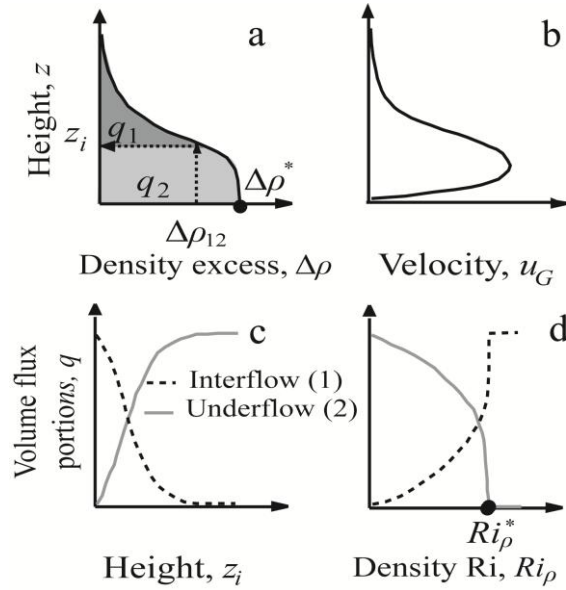


Fig. 2A1. (a) Density excess profile of the gravity current, $\Delta\rho(z)$. We mark the maximum value, $\Delta\rho^*$. (b) Velocity profile of the gravity current, $u_G(z)$. (c) Predictions of the volume flux portions q_1 and q_2 as a function of height, z_i . (d) Predictions of q_1 and q_2 as a function of the density Richardson number, Ri_ρ . We mark the critical value Ri_ρ^* .

Note that the integral Eqs. 2.A6 and 2.A7 are given in terms of the height z_i . One can think of Eqs. 2.A6 and 2.A7 as predictions of the portions q_1 and q_2 calculated from observations (Eqs. 2.A3 and 2.A4), based upon the internal gradients within the gravity current observed before it reaches the density step (Fig. 2.A1c). As a result, these predictions required detailed information of density and velocity profiles of the gravity current (Fig. 2.A1a,b). Those predictions can also be expressed in terms of Ri_ρ , as $q_1(Ri_\rho)$ and $q_2(Ri_\rho)$ (Fig. 2.A1d). The gravity currents will form underflows for $Ri_\rho \sim 0$, (i.e., $q_2(Ri_\rho) = 1$), and they will form interflows as $Ri_\rho \rightarrow \infty$, for which $q_2(Ri_\rho) \rightarrow 0$.

Methods: Intrusion thickness from time slices series - We measured the thickness of the interflow (h_1) at the location where vertical image slices were taken to construct time slices ($x = 1.3$ m, Fig. 2.6a), and after 7 minutes since the beginning of the injection in order to reach the steady state.

Results: Observed interflow and underflow thickness - The thickness of the interflows and underflows, h_1 and $(h^* - h_1)$, are taken as a proxy of the volumetric fluxes at the interflow and underflow intrusions (Q_1 and Q_2), and varied depending on Ri_ρ and Fr . Fig. 2.A2 includes the results of thickness as a function of Ri_ρ , and depending on the regime in terms of Fr (Fig. 2.8, Table 2.2), based on the analysis of changes occurring in the ambient stratification (Eqs. 2.A1 and 2A2). Note that the interflow

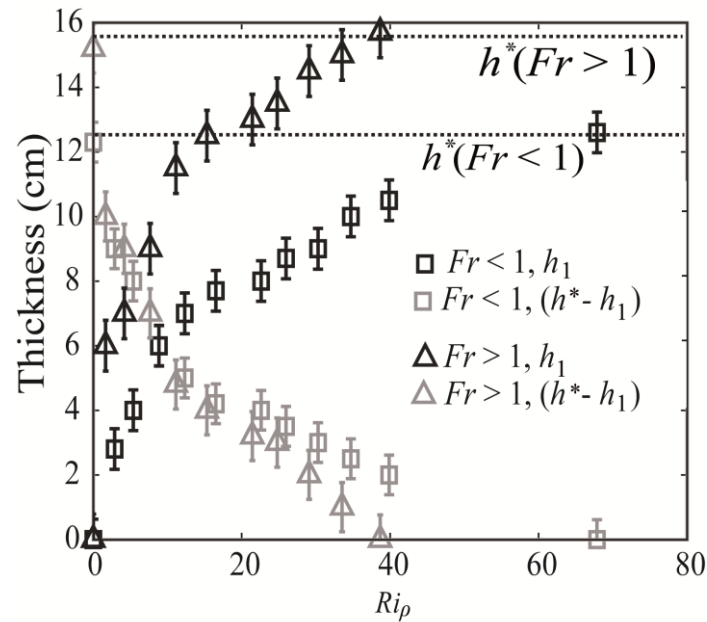


Fig. 2.A2. Experimental observations of interflow and underflow thickness, h_1 and $(h^* - h_1)$, for the two sets of runs: subcritical $Fr < 1$ (squares), and supercritical $Fr > 1$ (triangles). The dashed lines mark h^* for each regime. Black means interflow (1) and gray underflow (2) in all plots.

thickness increased with Ri_ρ and, for any given value of Ri_ρ , it was always larger in the supercritical regime compared to the subcritical regime (Fig. 2.A2). Note that the ratio of the maximum interflow thicknesses in supercritical and subcritical regimes (h^*) is equal to 1.22 (i.e., 15.4 cm and 12.6 cm, respectively), and equal to the ratio of the average thickness of the gravity current (h) in both regimes. This ratio justifies the use of different values of h^* to estimate the portions of volume flux when $Fr > 1$ and $Fr < 1$ as a function of the thickness of the interflow intrusion (Eqs. 2.A3 and 2.A4). Otherwise, q_1 would not be equal to the unity when the density step $\Delta\rho_{12}$ was higher than the maximum density excess of the current, $\Delta\rho^*$. These observations will be used to validate our predictions of volume flux portions based on the gravity current properties.

Discussion: Observed and predicted volume flux portions - The predicted partition of the gravity current volume flux (q_1 and q_2) at the density step from Eqs. 2.A6 and 2.A7 and the two sets of gravity current profiles in Fig. A.10, are compared to the observed portions (from Eqs. 2.A3 and 2.A4) in Fig. 2.A3 (predictions with lines and observations with symbols). Note that the predicted and observed estimates of $q_1(Ri_\rho)$ and $q_2(Ri_\rho)$ exhibit a good correlation, which again support our working hypothesis regarding the importance of the internal gradients in the gravity current properties to determine the portion of the current that splits at a density step.

Note that the critical value of Ri_ρ^* required for a pure interflow to develop ($q_1 = 1$) was ca. $Ri_\rho^* = 72$ in subcritical regime experiments, but $Ri_\rho^* = 40$ for the experiments

with supercritical regime. In addition, the value of $Ri_\rho[0.5]$ is lower than the value of Ri_ρ needed to have equal portions of the buoyancy flux flow as underflows and interflows (compare Fig. 2.A3 and 2.11). This occurs because the velocity profile that determines the volume flux has a different shape to the density profile in a gravity current, and implies that, in general, the volumetric partitioning of the gravity current in inter- and underflows will not coincide with the partition of the buoyancy flux.

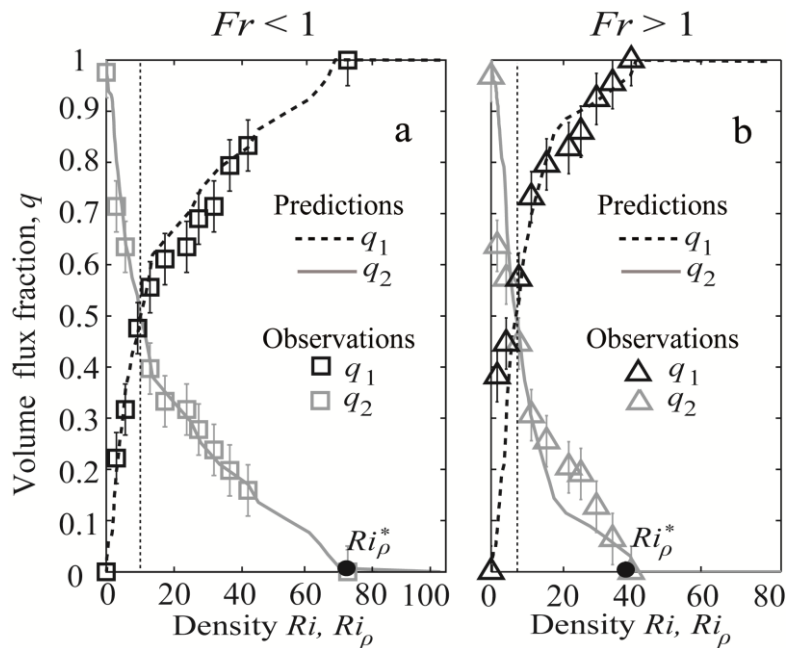
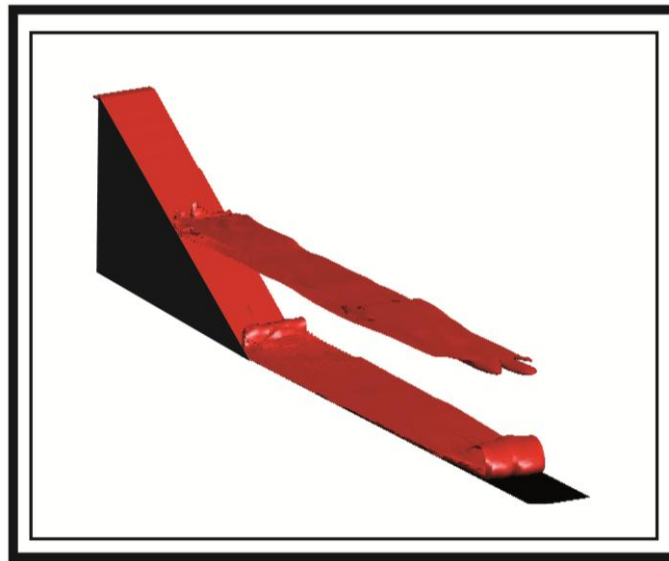


Fig. 2.A3. Predictions (lines) and experimental results (symbols) of volume flux portions as a function of the density Richardson number (q versus Ri_ρ) from experimental profiles of (a) subcritical gravity current ($Fr < 1$), and (b) the supercritical gravity current ($Fr > 1$) entering the two-layered stratified systems. The black dot marks Ri_ρ^* and the thin dashed line marks the $Ri_\rho[0.5]$ for each regime.

Chapter 3

ON THE DEVELOPMENT OF SPLIT FLOWS BY GRAVITY CURRENTS INTO TWO-LAYERED STRATIFIED BASINS



This article is in preparation to be submitted to the **Journal of Geophysical Research-Oceans** as:

Cortés, A., M.G. Wells, O. Fringer, R. Arthur, and F. Rueda. On the development of split flows by gravity currents into two-layered stratified basins, *J. Geophys. Res.*(in preparation)

Abstract

The vertical distribution of gravity currents in stratified systems can affect the ecology of the water body. This study uses numerical simulations to confirm and further extend a recently developed experimental partition theory of a two-dimensional gravity current in two portions (interflow and underflow) when entering a two-layered stratified system. Laboratory and simulation results show good quantitative agreement and stress the significance of the internal gradients within the gravity current (Fr), as well as a measure of the ambient stratification (Ri_ρ), on determining the partition of a gravity current into a stratified system. In general, both settings confirm that more dramatic ambient density changes are expected due to impingement of supercritical currents entering strongly stratified basins. We have used the model results to evaluate the errors in the gravity current partition estimates due to experimental measurements and numerical sources of uncertainty. In addition, new simulation runs have let us to characterize the current partition process of a wider range of gravity current regimes (Fr) and stratification strengths (Ri_ρ) through a forces balance (buoyancy vs. inertia) across the density step, in order to indentify the conditions controlling the splitting behavior of different current regimes to those observed in the laboratory. We also explain the current behavior based on the mixing efficiency, and discuss the implications of our predictions in lakes and the ocean.

Introduction

Gravity currents entering density stratified water bodies frequently introduce suspended and dissolved particles into the system (sediments, pollutants, salt, nutrients), which can affect the bio-geochemical processes undertaken in the water ecosystem. Therefore, both understanding the vertical distribution of the gravity currents in the water column and predict their fate are crucial for managing water quality (An et al. 2014). A large number of theoretical and experimental studies have been conducted to understand mixing in gravity currents and its interaction with ambient stratification in closed basins (Baines 2001; Fernandez and Imberger 2008a; Wells and Nadarajah 2009). Recent findings suggest that gravity currents into linearly density stratified environments not only entrain ambient water, but they also ‘*detrain*’ water from the current as they flow down-slope (Baines 2001). However, in many of those studies about gravity current mixing, the stratification in the basin has been approximated by two-layer stratification, with a well-mixed surface layer separated by a sharp interface from the deep denser waters (Monaghan et al. 1999; Samothrakis and Cotel 2006a,b;

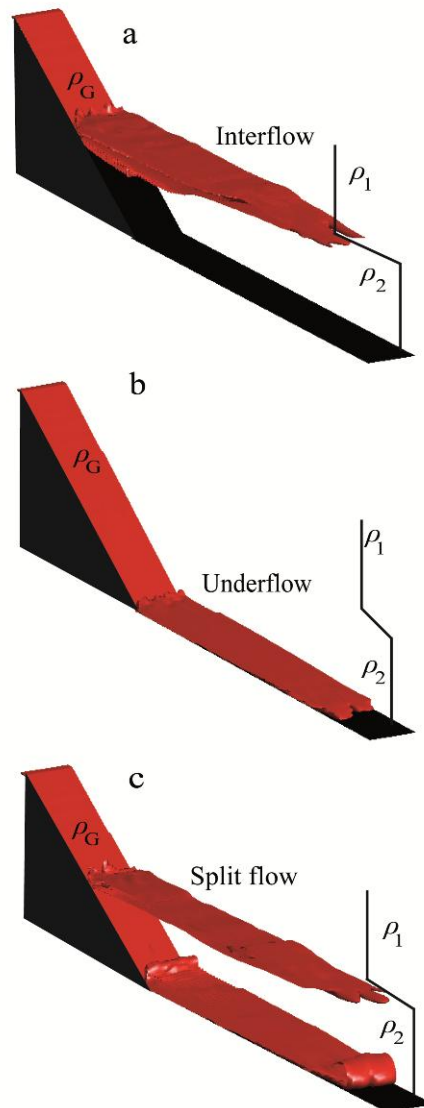


Fig. 3.1. Behavior of a 2D-gravity current of average density ρ_G in a two-layered stratified environment, ρ_1 and ρ_2 . (a) Interflows occur when $\rho_1 < \rho_G < \rho_2$. (b) Underflows occur if $\rho_G > \rho_2$. (c) Split flows form if the gravity current has significant internal density gradients.

Wells and Wettlauffer 2007). When a gravity current enters such a two-layered stratification, two inflow behaviors have been widely study (Fischer et al. 1979): if the impinging current is lighter than the lower layer then an intrusion forms on the thermocline (Fig. 3.1a, ‘interflow’); otherwise, it will intrude at the very base of the basin (Fig. 3.1b, ‘underflow’). However, gravity currents can also split as they impinge into a density step to form two intrusions (Fig. 3.1c, Monaghan (2007)). This behavior has been previously observed in laboratory experiments with vertical plumes (Kulkarni et al. 1993; Cotel and Breidenthal 1997) and turbidity currents (Rimoldi et al. 1996; Cesare et al. 2006). However, no indication was given of when splitting gravity currents should occur. Wobus et al. (2013) showed in their numerical results the three inflow behaviors presented in Fig. 3.1, and characterized them in terms of the increase in

potential energy in the system. Field observations in a Mediterranean reservoir by Cortés et al. (2014a) showed that a cold river inflow could split in two intrusions at the base of the surface mixed layer (SML). The authors stressed the significance of the formation of near surface intrusions at a density step (base of the SML), since their entrainment into the top layers of the reservoir could result in fluxes of river-borne nutrients readily used for phytoplankton growth, and thus, modifying the biochemical response of the ecosystem to inflows. As a result, it is critical to quantify the portion of the gravity currents when entering a stratified system which could reach the surface layers, as well as to understand the conditions controlling the partition of the current at a density step.

Recent laboratory observations (Cortés et al. 2014b) stressed the significance of the gravity current internal properties, as well as the ambient stratification on determining how a gravity current intrudes into a two-layered stratified water body. In their work, they considered the behavior of a two-dimensional (2D) gravity current flowing down a slope of angle $\theta = 25^\circ$ into a rectangular stratified water body, where the initial densities of the two ambient layers are ρ_1 in the surface, and ρ_2 in the bottom layer (Fig. 3.2a). The later was denser than the top layer (i.e., $\rho_2 > \rho_1$), and the density step between them is defined as $\Delta\rho_{12} = (\rho_2 - \rho_1)$. Here, we use two different reference systems referred to the beginning of the ramp: (a) x and y are the horizontal and vertical-

Table 3.1. Tank dimensions and constant inflow conditions of the two-dimensional gravity currents created in the laboratory and simulated in this work.

Variable	Units	Laboratory		Simulations	
		Subcritical	Supercritical	Subcritical	Supercritical
<i>Tank conditions</i>					
Length, L	m		2.5		2.87
Density of the fresh water, ρ_1	kg m ⁻³		998		998 - 1000
Total water column depth, Y	m		0.45		0.48
Thickness of the top layer, H	m		0.22		0.22
Thickness of the bottom layer	m		0.22		0.22
<i>Inflow conditions</i>					
Inflow rate, Q_0	m ³ s ⁻¹	8.57×10^{-6}	8.57×10^{-6}	1.08×10^{-5}	1.68×10^{-5}
Inflow velocity, U_0	m ³ s ⁻¹	-	-	0.016	0.016
Inflow thickness, h_0	m	-	-	3.4×10^{-3}	5.1×10^{-3}
Inflow density, ρ_0	kg m ⁻³	1,199	1,199	1,160	1,103
Inflow reduced gravity, g'_0	m s ⁻²	1.97	1.97	1.568	1.009
Inflow buoyancy flux per unit width, B_0	m ³ s ⁻³	7.68×10^{-5}	7.68×10^{-5}	7.68×10^{-5}	7.68×10^{-5}

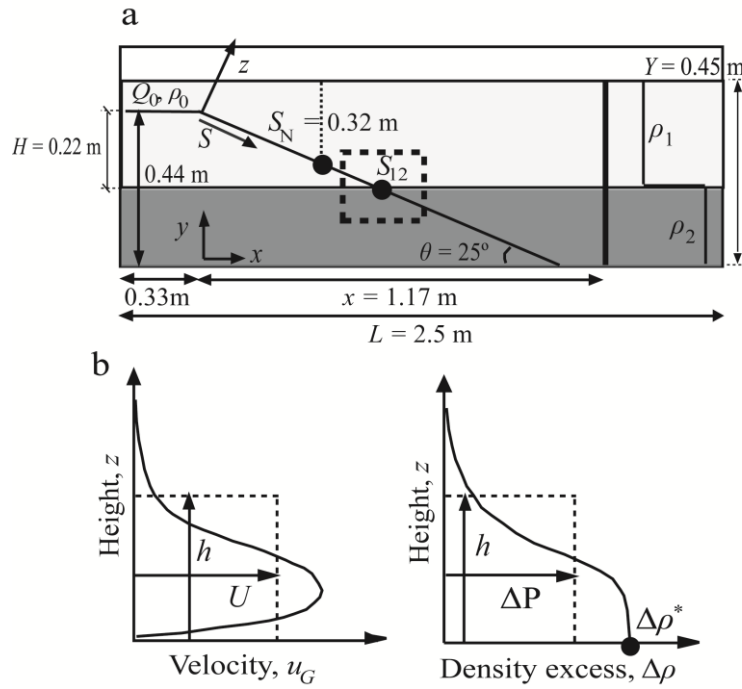


Fig. 3.2. (a) Schematic layout of the experimental setup (not scaled). The vertical solid line ($x = 1.17$ m) marks the location where ambient density profiles were experimentally measured. The vertical dashed line at the slope ($S_N = 0.32$ m) marks the location where gravity current profiles were measured. The region inside the dashed rectangles is study in Fig. 3.10. (b) Theoretical velocity $u_G(z)$ and density excess $\Delta\rho(z)$ profiles of the gravity current measured at S_N . We mark the average variables of the current (h , U , ΔP), and the maximum value of $\Delta\rho(z)$ as $\Delta\rho^*$.

upward coordinates, respectively, and (b) the along-slope and normal-to-the-slope coordinates were referred to as S and z , respectively. They also defined H as the vertical distance from the initial depth of the gravity current to the density step, Y as the total depth of the water column, and L as the total length of the tank. The gravity current, in turn, was initially characterized in terms of its inflow rate Q_0 , density ρ_0 , width W , inflow reduced gravity $g'_0 = g(\rho_0 - \rho_1)/\rho_1$, and its inflow buoyancy flux per unit width $B_0 = g'_0 Q_0 / W$ [$\text{m}^3 \text{s}^{-3}$] ($g =$ gravitational acceleration). Tank dimensions and inflow variables were constant in all the laboratory experiments, and they are summarized in Table 3.1. The authors quantified the strength of the stratification in terms of the density Richardson number (Ri_ρ) (Wells and Wettlaufer 2007), calculated as,

$$Ri_\rho = \frac{g'_{12} H}{B_0^{2/3}} \quad (3.1)$$

where, $g'_{12} = g \Delta\rho_{12} / \rho_1$ represents the reduced gravity of the ambient water density step. For values of Ri_ρ above a given threshold Ri_ρ^* , the gravity current should form an interflow at the density step (Fig. 3.1a). For $Ri_\rho < Ri_\rho^*$, in turn, it should penetrate through the density step forming an underflow (Fig. 3.1b). For $Ri_\rho \approx Ri_\rho^*$, Wells and Wettlaufer (2007) observed that part of the gravity current flowing into the density step

would leak to the bottom, as an underflow, and formed multiple intrusions (Fig. 3.1c). They found that the critical values of Ri_ρ could range from 21 to 27. On the other hand, internal gradients within the gravity currents (due to the turbulent mixing at the interface layer at the top of the current) were characterized in terms of the densimetric Froude number (Fr). This non-dimensional number was calculated from the average velocity U , thickness h , and reduced gravity G' of the current, as follows,

$$Fr = \frac{U}{(G'h)^{1/2}} \quad (3.2)$$

where $G' = g \Delta P / \rho_1$, and ΔP is the average density excess of the gravity current. Average variables of the gravity current (h , U and G') were calculated as in Ellison and Turner (1959) from the gravity current velocity profile $u_G(z)$ and density excess profile $\Delta\rho(z) = (\rho(z) - \rho_1)$ (Fig. 3.2b).

Based on these two non-dimensional numbers (Ri_ρ and Fr) and their laboratory observations at the gravity current and stratified water column, Cortés et al. (2014b) developed an analytical theory to quantify the portions of the buoyancy flux per unit width from the current that become interflow or underflow (named b_1 and b_2 , respectively, Fig. 3.3). They used two different approaches to quantify the current partition at the density step: (1) experimentally from the changes in the ambient density profiles observed in the tank after the gravity current injection (Fig. 3.3a), and (2) theoretically based upon the density excess $\Delta\rho(z)$ and velocity gradients $u_G(z)$ within the gravity current (Figs. 3.3b-e). In their laboratory experiments, they tested for different two-layered ambient stratifications (different $\Delta\rho_{12}$), the inflow behavior of two types of gravity currents: one in the sub-critical regime ($Fr < 1$) and another in the super-critical regime ($Fr > 1$). Despite the good fits between experimental and theoretical estimations of flux partition, there are still sources of uncertainty in their laboratory results, since measuring continuous series of the study variables (velocity and density) in the whole study system was not feasible in the laboratory. In addition, the physical arguments about gravity current partition or wider ranges of current regimes could not be tested experimentally. In this regard, numerical modeling is a powerful tool which, once validated, could be used to perform further measurements in the complete domain as well as new experiments in order to gain insights on the dynamics of gravity currents impinging a density step.

In this study, we use the parallel version of the code developed by Fringer and Street (2003) to confirm, evaluate and further extend the experimental partitioning theory developed by Cortés et al. (2014b), and characterize the impinging process of a gravity current at a density step, which could not be done experimentally. First, the model results are validated against the available experimental data, confirming the partition buoyancy flux theory and the physical arguments suggested by the authors. Then, we used model results to evaluate the uncertainty in both the theoretical and

numerical predictions of flux partition. Finally, we characterize the current partition process through a forces balance (buoyancy vs. inertia) across the density step in order to indentify the conditions controlling the splitting behavior of a wide range of current regimes. This work is organized as follows. First, we present the available laboratory data, numerical model description and simulations set-up. Then, we show, evaluate and discuss the model results in order to provide a better understanding of the gravity current partition at a density step in terms of processes. Finally, we state the conclusions and possible implications of our research about gravity currents entering natural stratified water bodies.

Methods

Available laboratory data and theoretical buoyancy flux partition - Laboratory experiments consisted of two sets of experiments with different gravity current regimes (A-runs with $Fr = 0.69$, and B-runs with $Fr = 1.31$), where density at the bottom layer (ρ_2) was systematically varied in order to attain different $\Delta\rho_{12}$, and thus Ri_ρ , since B_0 and H were held constant (Eq. 3.1). Similar values of Ri_ρ were tested for both subcritical and supercritical gravity currents (Table 3.2). Both types of currents were achieved modifying the initial conditions of the inflowing 2D plume, but conserving the buoyancy flux per unit width at the current.

Table 3.2. Specifications of the experimental A- (subcritical, $Fr < 1$) and B- (supercritical, $Fr > 1$) runs. We mark in bold the runs whose results are shown in Fig. 3.6.

Sub-critical, $Fr < 1$			Supercritical, $Fr > 1$		
Run	$\Delta\rho_{12}$ (kg m^{-3})	Ri_ρ	Run	$\Delta\rho_{12}$ (kg m^{-3})	Ri_ρ
A-1	64.60	77.34	B-21	66.29	79.36
A-3	51.93	62.17			
A-4	45.88	54.92			
A-5	34.28	41.03	B-22	38.33	45.89
A-10	24.28	29.07	B-26	24.01	28.74
A-13	15.69	18.78	B-29	17.05	20.41
A-15	9.03	10.81	B-32	8.89	10.64
A-17	6.15	7.36	B-34	5.32	6.37
			B-35	3.80	4.55

$\Delta\rho_{12}$ – Density difference at the density step
 Ri_ρ - Density Richardson number

The available laboratory data to validate model results consist of: (1) density profiles of the complete (i.e., $Y = 0.45$ m) ambient water column at the end of the slope ($x = 1.17$ m, Fig. 3.2a, solid line) measured before and after the injection of the dense current ($\rho_{int}(y)$ and $\rho_{obs}(y)$, respectively) during ca. 7 min; and (2) velocity $u_G(z)$ and density excess $\Delta\rho(z)$ profiles within the gravity current measured at a site 0.20 m upstream of the density step located at $S_{12} = 0.52$ m (i.e., $S_N = 0.32$ m, Fig. 3.2a, dashed line). Measured gravity current profiles covered a control volume of 3 cm above the bottom slope with a resolution which ranged between 1mm and 0.05 mm for velocity and density, respectively.

The formulation developed by the authors to quantify the portions of the buoyancy flux per unit width from the current that become interflow or underflow (b_1 and b_2 , respectively, Fig. 3.3) use the described available laboratory data as follows. First, the non-dimensional change in ambient buoyancy (g') for a longitudinal area (i.e., $L \times \int dy$) per unit time due to an interflow or an underflow for a specific density step $\Delta\rho_{12}$ was referred to as $b_1(\Delta\rho_{12})$ or $b_2(\Delta\rho_{12})$, respectively, and is calculated as,

$$b_i(\Delta\rho_{12}) = \frac{L}{B_0 \cdot \Delta t} \frac{g}{\rho_1} \int_{lim_1}^{lim_2} [\rho_{obs}(y) - \rho_{int}(y)] dy \quad (3.3)$$

where subscript $i = [1, 2]$ for interflow and underflow, respectively, and integration limits are $lim_1 = [(Y - H), 0]$ and $lim_2 = [Y, (Y - H)]$, respectively (Fig. 3.3a). Furthermore, Δt defines the time interval between the initial and final ambient density profiles (ca. 7 min). All other terms have been already defined above. Note that the partition of buoyancy flux between interflow and underflow can also be expressed in terms of Ri_ρ , since B_0 and H were held constant in their experiments (Eq. 3.1).

Second, the authors estimated the portions of the inflow buoyancy flux becoming interflows or underflows based upon the density excess $\Delta\rho(z)$ and velocity $u_G(z)$ within the gravity currents. For any given value of $\Delta\rho_{12}$, they suggested to identify the height at the current $z = z_i$ such that $\Delta\rho(z) = \Delta\rho_{12}$, and determine the actual portions b_1 and b_2 for that particular scenario (Fig. 3.3b and 3.3c) as follows,

$$b_i(z_i) = \frac{1}{B_0} \frac{g}{\rho_1} \int_{lim_1}^{lim_2} \Delta\rho(S_N, z) u_G(S_N, z) dz \quad (3.4)$$

where integration limits are this time $lim_1 = [z_i, 0]$ and $lim_2 = [\infty, z_i]$, respectively (Fig. 3.3d). Note that this partition of buoyancy flux can also be expressed in terms of $\Delta\rho(z)$, rather than z_i , given that the density excess profile at the gravity current is a monotonic function of height (Fig. 3.3b). Therefore, again, they expressed the partition of buoyancy flux in terms of Ri_ρ , since it is a linear function of $\Delta\rho$ (Eq. 3.1, and Fig. 3.3e).

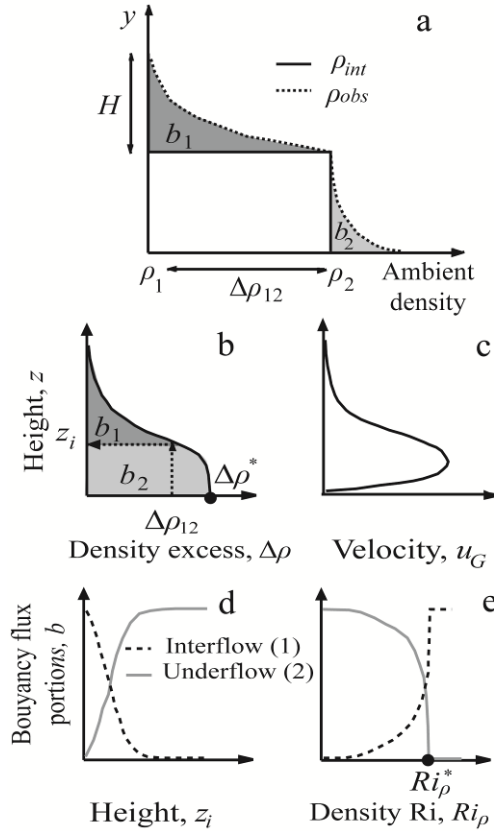


Fig. 3.3. (a) Experimental estimation of buoyancy flux portions at the interflow and the underflow (b_1 and b_2 , respectively) when the gravity current splits due to a density step ($\Delta\rho_{12}$), from the observed initial and final density profiles in the ambient water ($\rho_{int}(y)$ and $\rho_{obs}(y)$, respectively). (b) Density excess profile of the gravity current, $\Delta\rho(z)$. We mark the maximum value, $\Delta\rho^*$. (c) Velocity profile of the gravity current, $u_G(z)$. (d) Predictions of b_1 and b_2 as a function of height, z_i . (e) Predictions of b_1 and b_2 as a function of the density Richardson number, Ri_ρ . We mark the critical value, Ri_ρ^* .

Numerical model - The incompressible Navier-Stokes equations for conservation of momentum with the Boussinesq approximation, the continuity equation for conservation of mass, and the density transport equation were solved using the code developed by Fringer and Street (2003) in the domain shown in Fig. 3.4. This code employs the fractional-step method of Zang et al. (1994) using a finite-volume formulation on a generalized curvilinear coordinate non-staggered grid, which use a semi-implicit time discretization second-order accuracy with Adams-Bashforth scheme for the explicit terms and Crank-Nicholson scheme for the implicit terms. Additionally, the code uses the QUICK and SHARP schemes for advection of momentum and scalars, respectively, and solves the pressure Poisson equation with a multigrid method. This code has been validated with several laboratory-scale studies on geophysical fluid dynamics using its single-processor version (Zedler and Street 2001; Fringer et al. 2005) as well as its parallel version (Cui and Street 2001; Venayagamoorthy and Fringer 2005, 2006, 2007).

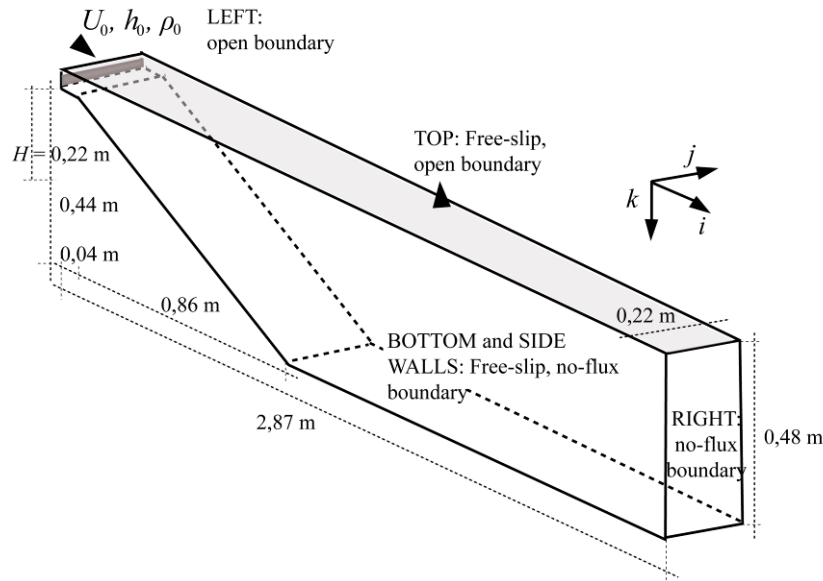


Fig. 3.4. Computational domain depicting the dimensions and boundary conditions for the simulations corresponding to the experimental runs (Fig. 3.2a). Note that in the simulations the vertical coordinate k is referred to the tank surface and down-wards.

Although this code had already implemented as turbulence closure scheme the large-eddy simulation (LES) technique, we have not used this approach in this work due to the high computational resources required to solve the scales of turbulence of our study domain (see *Simulation set-up*). Thus, we have adopted the so called Reynolds-averaged Navier-Stokes (RANS) approach as a closure scheme, in which six extra terms (i.e. Reynolds stresses) are added in the averaged momentum equations, and a turbulent scalar flux term in the scalar transport equation. As a result, additional equations are needed to close the system equations in order to obtain solutions. From the different methods for closing the RANS system of equations, here we model the turbulent flux terms as a linear function of the shear rate (i.e. $S_r = du/dz$) multiplied by a turbulent viscosity, ν_t (i.e., Boussinesq turbulent-viscosity hypothesis). For this study, we have implemented a zero-equation turbulence model in the parallel version of the code of Fringer and Street (2003) to model eddy viscosity, since it can yield accurate results for simple turbulent flows without any additional partial differential equation (Chen and Jaw 1998). In addition, we found good agreement between simulation results using both RANS and LES turbulence closing techniques in scaled-reduced domains (comparison not shown here).

According to the zero-equation turbulence closure scheme, we model a parabolic eddy viscosity ν_t as a function of the flow depth k ($= y - Y$) referred to the tank surface by using a momentum balance between the horizontal pressure gradient and turbulent shear stress (vertical mixing) in conjunction with the Boussinesq turbulent-viscosity hypothesis as (Rodi 1993),

$$v_t(k) = C_\kappa u_\tau \left(\frac{-k}{D_k} \right) (D_k + k) \quad (3.5)$$

where C_κ is the von Karman constant ($= 0.41$), k is a negative downwards distance from the free surface of the domain, D_k is the depth of each domain column, and u_τ is the bottom shear friction velocity, which calculated as a function of the drag coefficient C_D , and the current velocity at the first grid point above the bottom boundary, u_1 , as $u_\tau = C_D u_1^2$ (Fringer et al. 2006). Since the experimental tank surfaces were smooth (acrylic), we assume an average value of $C_D = 0.0015$, from the range reported by Deacon and Webb (2005).

Due to the fact that stable stratification tends to suppress turbulence away from the bottom boundaries, Munk and Anderson (1948) proposed a model to modify the parabolic eddy viscosity from Eq. 3.5, named $v_{t|mod}(k)$, in the presence of strong density gradients, which quantified in terms of the gradient Richardson number Ri_g and the depth of the system k , as follows,

$$v_{t|mod}(k) = v_t(k) \cdot (1 + \beta Ri_g(k))^\alpha \quad (3.6)$$

Here, $Ri_g = N^2 / S^2$, where $N = (-g / \rho_0)(dp / dk)]^{1/2}$, and β and α are experimentally determined constants with given values of 10 and -0.5, respectively (Munk and Anderson 1948). This parameterization has been recently applied to model turbulent channel flows by Elliott and Venayagamoorthy (2011), which allowed modeling significant reduction of the vertical turbulent mixing that occurred at the density step in a two-layered stratified system.

Finally, turbulent diffusion in the scalar transport equation was parameterized through the eddy diffusivity $K_t(k)$, as,

$$K_t(k) = \frac{v_t(k)}{Pr_t} \quad (3.7)$$

where Pr_t is the turbulent Prandtl number. A recent study by Elliott and Venayagamoorthy (2011) evaluated different parameterizations of Pr_t as a direct function of the gradient Richardson number, Ri_g (see their Fig. 3.2). Note that in the laboratory the authors always observed values of $Ri_g > 0.25$ below the current-ambient interface in their characteristic gravity currents profiles (see Fig. 2.10c,f in Cortés et al. (2014b)). Thus, we used in this work the following parameterization of Pr_t (Strang and Fernando 2001; Elliott and Venayagamoorthy 2011),

$$Pr_t = \frac{5 \cdot (1 + 5 \cdot Ri_g)^{-1.5} + 0.2}{5 \cdot (1 + 5 \cdot Ri_g)^{-2.5} + 0.01} \quad (3.8)$$

where depth-average values gradient Richardson numbers below the interface are $Ri_g = [3.85, 0.61]$ in the laboratory subcritical and supercritical gravity currents which we were aiming to reproduce (standard deviation $[1.09, 0.08]$, respectively). As a result, Eq. 3.8 yields average values of turbulent Prandtl number $Pr_t \sim [20, 5]$ for each regime, respectively. According to this parameterization, turbulent scalar mixing is enhanced in supercritical gravity currents (lower Ri_g values).

Simulations set-up - The tank geometry $(l_i, l_j, l_k) = (2.86, 0.22, 0.48)$ m was discretized using a number of grid cells $(n_i, n_j, n_k) = (256, 16, 128)$ in the longitudinal, lateral and vertical direction, respectively (Fig. 3.4). Note that the length and height of the simulated domain was larger than in laboratory experiments, in order to recreate the same volume of receiving ambient water both in simulations and laboratory experiments, since no water existed below the sloping bottom in the simulated runs. Each run reproduced the continuous injection of a traced gravity current during 7 min, using 64 processes (16 and 4 processes in the longitudinal and vertical direction, respectively), 5 sub-grid levels, and a time step of 0.003 s, with a maximum Courant number of ~ 0.16 . Model results consist of time-evolution (saved every 6 seconds) in the whole study domain of the three-component velocity, density and a passive tracer injected by the gravity current.

Prior to the injection of the gravity current, the initial velocity field is quiescent and the initial background two-layered stratification at each domain column is given by,

$$\frac{\rho}{\rho_1}(k) = 1 - \frac{\Delta\rho_{12}}{2\rho_1} \tanh\left[\frac{2(k-H)}{\delta_{12}} \tanh^{-1}(\alpha_{12})\right] \quad (3.9)$$

where $\rho_1 = 1000 \text{ kg m}^{-3}$ is the reference density measured at the top layer with a constant thickness $H = 0.22$ m, $\delta_{12} = 0.03$ m is the interface thickness between the two layers, and $\alpha_{12} = 0.99$ defines the sharpness of the interface. In order to minimize the increase with time of the thickness at the interface between the two layers with different density (ρ_1 and ρ_2), it was chosen a value of interface thickness so that $\delta_{12} \sim 10\Delta k_{Y/2}$, where $\Delta k_{Y/2}$ corresponds to the grid spacing at mid-depths. In each run (a total of 15), we varied $\Delta\rho_{12}/\rho_1$, defined as the non-dimensional density step between the two layers, according to Table 3.2.

At the left-hand boundary of the domain shown in Fig. 3.4, we prescribe a dense inflow with constant inflow velocity U_0 , thickness h_0 , density ρ_0/ρ_1 . We varied those values to obtain subcritical and supercritical gravity currents down-slope (Table 3.1), but with the same buoyancy inflow flux per unit width, $B_0 = g((\rho_0 - \rho_1)/\rho_1) U_0 h_0$. In addition, we simulated the injection in all currents of a passive tracer with an initial concentration of $C_0 = 1 \text{ kg m}^{-3}$. Boundary conditions for the cross-shore (horizontal) velocity u are free-slip at the bottom and top boundary, and no-flux at the right

boundary. The vertical velocity has a no-flux boundary condition at bottom boundary, while these fluxes update based on the inflow west velocity at the top boundary. In addition, vertical velocity has free-slip boundary conditions on all other walls. Finally, density field has a gradient-free boundary condition on all walls.

We use molecular viscosity of $\nu = 10^{-5} \text{ m}^2 \text{ s}^{-1}$, and a molecular diffusivity of $K = 10^{-8} \text{ m}^2 \text{ s}^{-1}$, which ratio is of $O(10^3)$ in this work to account for that fact that density variation in the laboratory experiments was achieved by salinity change (Cui and Street 2003). A rough estimate of the turbulent Reynolds number for these flows, based on an advective length scale of $L_c \sim 0.015 \text{ m}$ and a characteristic velocity of $U \sim 0.05 \text{ m s}^{-1}$, is $Re_T \sim 25$. The corresponding Kolmogorov microscale is then $\eta_k = L_c Re_T^{-3/4} = 1.3 \text{ mm}$. With a longitudinal grid spacing of 1 cm and vertical grid spacing of 3.7 mm in the deep region and 0.3 mm in the shallow region, the longitudinal grid spacing is about 8 times larger than the Kolmogorov microscale and the largest vertical grid spacing is 3 time larger.

Results and discussion

We first present the validation of the numerical model, which we further used to demonstrate the physical arguments about the experimental gravity current partition at a sharp density step. Then, we undertook a sensitivity analysis in order to evaluate model performance. Finally, we used the model results to characterize the impinging process through a forces balance (buoyancy vs. inertia) across the density step in order to identify the conditions controlling the splitting behavior of a wide range of current regimes, which can be observed in the field.

Model validation - The experimental results by Cortés et al. (2014b) showed that gravity currents are more likely to detrain into two parts at a density step when they have a diffuse interface layer at the top of the current (super-critical currents), while they tend to intrude as a single intrusion when the current have a sharp, more step-like density profile (sub-critical currents). We have successfully reproduced these gravity current behavior patterns though numerical experiments. Velocity $u_G(z)$ and density excess $\Delta\rho(z)$ profiles within the gravity current measured at a S_N (Fig. 3.2a, dashed line) in our simulations shown good qualitative agreement with the profiles measured in the laboratory at the same location (Fig. 3.5). Simulated gravity current profiles exhibited differences which were consistent with those observed in the laboratory. The supercritical gravity currents had larger values of h and U , but lower ΔP (Figs. 3.5a,b). Also, gradients in the density excess profiles tend to be sharper in the subcritical currents, while the current-ambient interface layer was more diffuse and thicker for the

supercritical flows (Figs. 3.5c,d). Our runs were able to reproduce a subcritical gravity current ($Fr < 1$) of similar average thickness h and velocity U as in the laboratory, but 31% lower average density excess ΔP , which yields values of densimetric Froude numbers Fr slightly higher ($= 0.86$) in our simulation results (Table 3.3). On the other hand, simulated supercritical currents ($Fr > 1$) were 5.3% thinner and with 14.9% lower velocity than in the laboratory, but they had similar density excess, resulting in simulated Fr smaller ($= 1.10$) than the experimental values (Table 3.3). Finally, our simulated profiles for both regimes are also comparable to analytical profiles of velocity and density excess determined from the empirical relationships proposed by Sequeiros (2012) (Fig. 3.5, dashed lines). His equations estimate current thickness, maximum velocity, and density excess (among others) based on the densimetric Froude number (see his Eqs. 23 – 27). Again, patterns of average current properties in both experimental regimes were reproduced with the analytical gravity current profiles estimated as Sequeiros (2012).

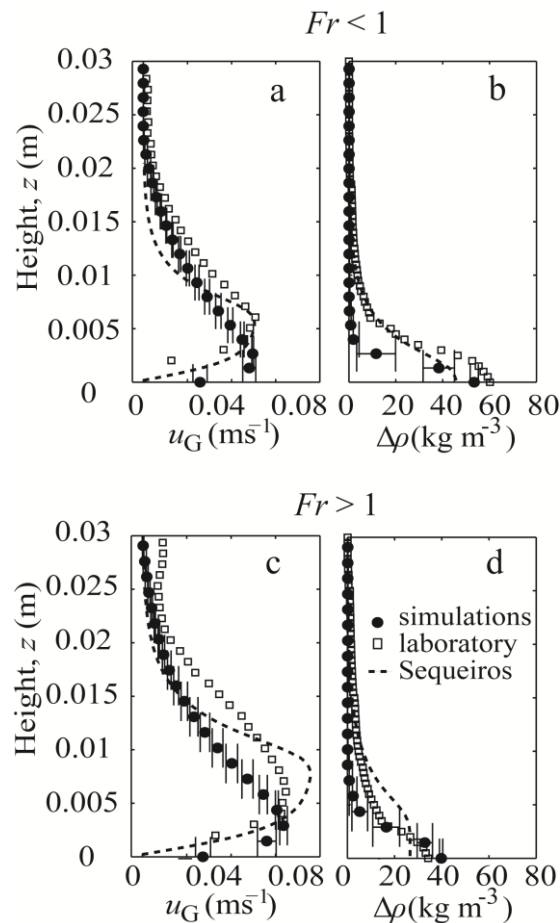


Fig. 3.5. Simulated, experimental and analytical (Sequeiros 2012) profiles of the two gravity currents gathered at the slope before the current hits the density step (S_N), with subcritical ($Fr < 1$, a,b) and supercritical ($Fr > 1$, c,d) regimes, where (a, c) are velocity profile, $u_G(z)$, and (b, d) density excess profile, $\Delta\rho(z)$. Error bars mark the standard deviation of the simulated profiles due to the point of measurement at the slope.

Table 3.3. Average gravity current properties from laboratory experiments and simulations results for the two current regimes (subcritical $Fr < 1$, and supercritical $Fr > 1$). We use the same values as in the simulations to dimensionalize analytical profiles by Sequerios (2012).

		h (cm)	U (cm s ⁻¹)	ΔP (kg m ⁻³)	Fr
Laboratory	Sub-critical	1.68	3.3	14	0.69
	Super-critical	2.06	5.1	8	1.31
Simulations and analytical	Sub-critical	1.61	3.36	9.5	0.86
	Super-critical	1.95	4.34	8.1	1.1

h - Average thickness of the gravity current (g.c.)

U - Average velocity of the g.c.

ΔP - Average density excess of the g.c.

Fr - Densimetric Froude number of the g.c.

Regarding the ambient water density changes, simulated profiles measured at $x = 1.17$ m at the beginning $\rho_{int}(y, t = 0 \text{ min})$, and at the end $\rho_{obs}(y, t = 7 \text{ min})$ of a set of numerical experiments show good agreement with experimental results (Fig. 3.6). As in the laboratory, interflows are thicker for larger Ri_ρ , since a higher fraction of current flux has been added to the top layer, while for lower values of Ri_ρ underflows tend to increase (for example, Figs. 3.6d and 6f). Furthermore, different gravity current regimes resulted in different initial and final density profiles for similar Ri_ρ , observing larger portions of the inflow current added to the top layer when $Fr > 1$ at the current compared to $Fr < 1$ (for example, Figs. 3.6d and 3.6a). The major differences between simulation and experimental ambient water density profiles are observed near the density step, likely associated to the numerical diffusion. We quantified the error in the simulated profiles by normalizing the root mean square error ($RMSE$, Jin et al. 2000) by the maximum density value (i.e., $nRMSE = [RMSE / \max(\Delta\rho)] \times 100$), which yields maximum values of $nRMSE \sim 16.6\%$. Note that the normalized $RMSE$ ($nRMSE$) was larger for smaller $\Delta\rho_{12}$ (e.g., A17 and B34, Fig. 3.6). In summary, the successful comparison of numerical and experimental measurements justifies the further use of the numerical model to confirm the experimental buoyancy flux partition theory.

Buoyancy flux partition from experimental and simulated results - We have also found reasonable agreement between the simulated and experimental vertical distribution of the material injected by the gravity current as presented in the laboratory. Fig. 3.7 shows the simulated spatial distribution of the tracer concentration in the tank after 7 min injection of the two experimental gravity currents ($Fr < 1$ in Figs. 3.7a,c and $Fr > 1$ in Figs. 3.7b,d) into a two-layered stratified system with different density step ($Ri_\rho \sim 42$ in Figs. 3.7a,b and $Ri_\rho \sim 7$ in Figs. 3.7c,d). As in the laboratory experiments, we observed thicker interflows for larger values of Ri_ρ (compare Figs. 3.7a and 3.7c), and also in response to supercritical currents (compare Figs. 3.7b and 3.7a). Note also that in all plots the most diluted material is retained at the density step, and thus the less

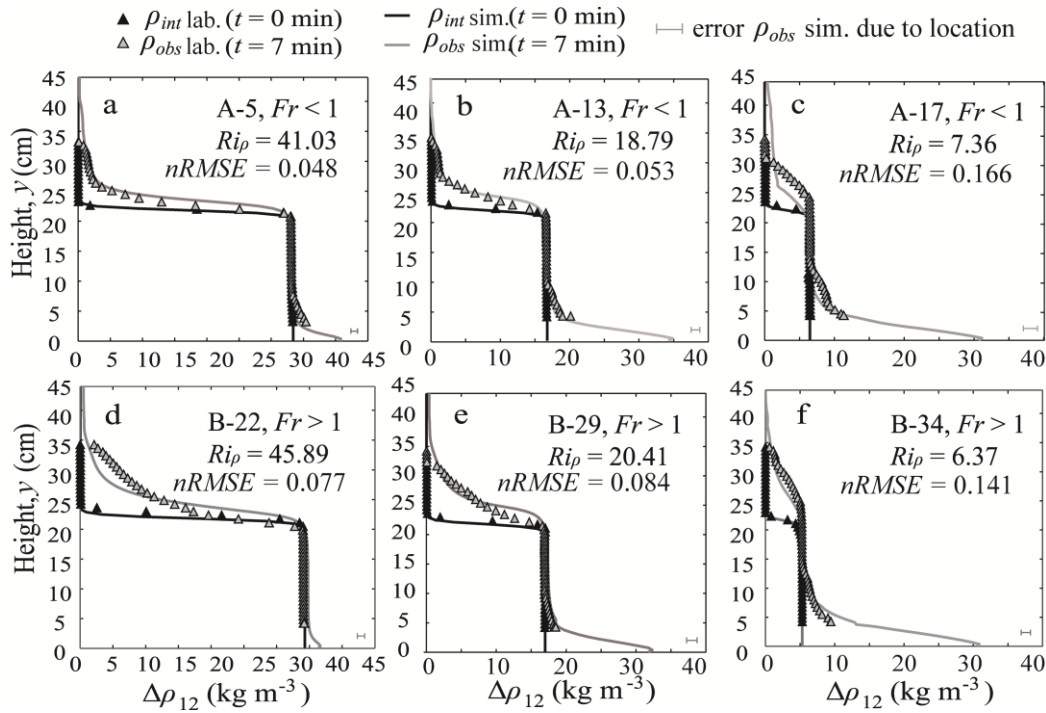


Fig. 3.6. Experimental (lab.) and simulated (sim.) ambient water density profiles before the gravity current injection (ρ_{int}) and after ca. 7 min since the beginning of the injection (ρ_{obs}), gathered at $x = 1.17$ m in the tank from the beginning of the ramp (Fig. 3.2a) during the experiments mark in bold in Table 3.2. Maximum standard deviations in the simulated profiles (due to the point of measurement in the tank) are marked in the lower right corner of the graph with horizontal bars. Values of the normalized *RMSE* (*nRMSE*) are also included in each subplot.

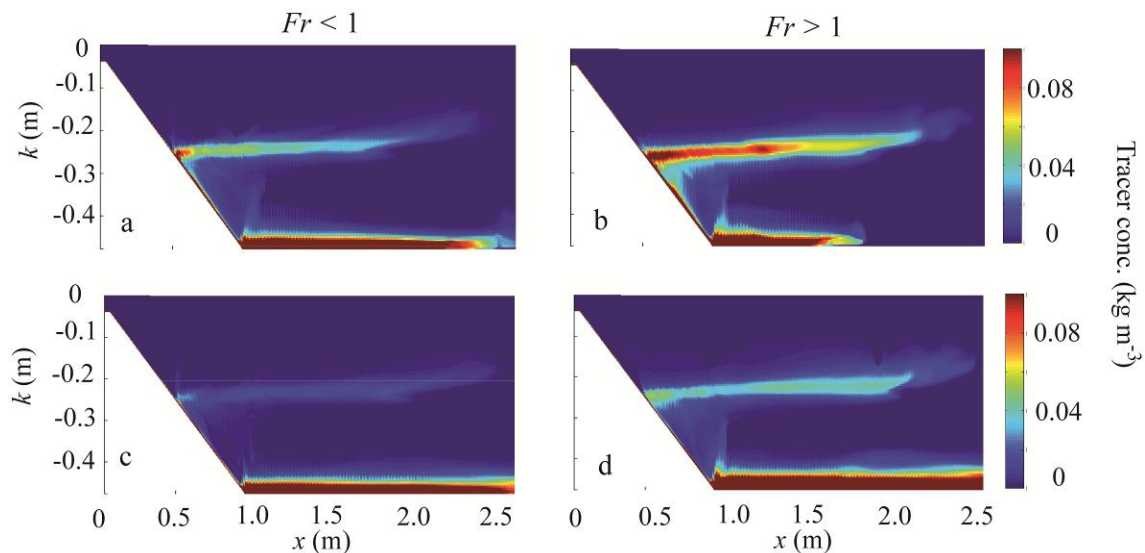


Fig. 3.7. Simulated spatial distribution of the tracer concentration (conc.) in the tank after 7 min of injection of the two experimental gravity currents (a,c) subcritical, and (b,d) supercritical, into a stratified system with different density step (a,b) $Ri_\rho \sim 42$, and (c, d) $Ri_\rho \sim 7$.

dense, while more concentrated material (more dense) can be observed at the bottom of the tank.

Regarding the partition of the current material, Fig. 3.8 shows in (a, b) the laboratory and in (c, d) the simulated buoyancy flux portions as a function of the density Richardson number (b versus Ri_ρ) for the two types of gravity current: (a, c) subcritical, and (b, d) supercritical. Note that simulation results yielded estimations of flux portions from ambient density changes (Eq. 3.3) consistent with the theoretical predictions of b associated to the corresponding simulated gravity current profiles (Eq. 3.4). Nevertheless, simulated and experimental results associated to similar values of Fr and Ri_ρ may present maximum differences of 16.8%. These differences are more obvious in

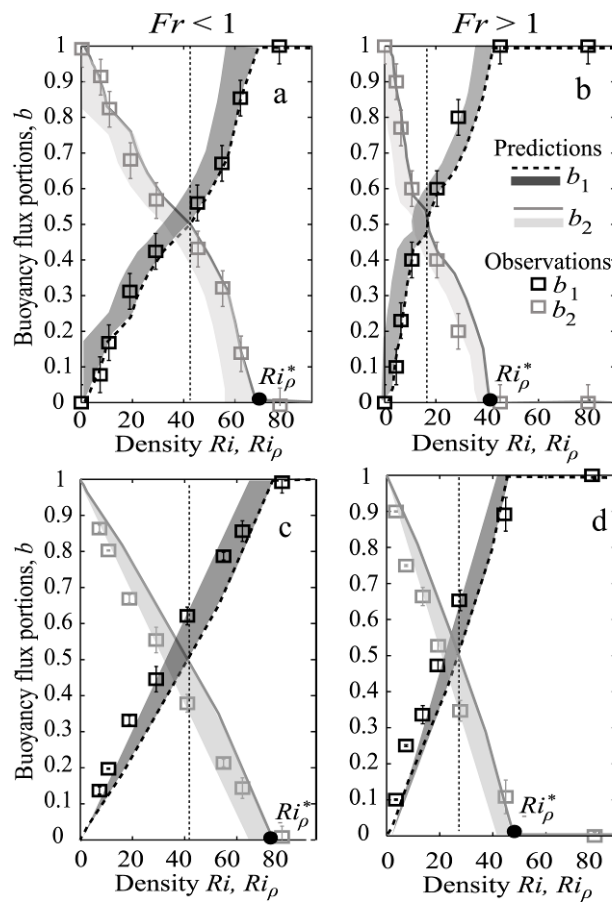


Fig. 3.8. Laboratory (a, b) and simulated (c, d) buoyancy flux portions as a function of the density Richardson number (b versus Ri_ρ) for the two types of gravity current: (a, c) subcritical gravity current ($Fr < 1$), and (b, d) supercritical gravity current ($Fr > 1$). Portions from current profiles are marked with lines, while portions from density changes in the tank are represented by symbols. The black dot marks the critical value of Ri_ρ^* and the thin dashed line marks the $Ri_\rho[0.5]$ for each regime. The shaded regions show the range of predicted values of b due to the error introduced by neglecting additional entrainment of ambient water before the gravity current reached the density step (Fig. 3.2a). Vertical lines represent the maximum standard deviation in the portion values due to errors association to the measurements point of the density changes in the tank.

the supercritical current regime. For instance, the value of Ri_ρ for which 50% of the buoyancy flux in the gravity current becomes an interflow, $Ri_\rho[0.5]$, was 16.2% larger in simulations with supercritical current, while experimental and simulated value of $Ri_\rho[0.5]$ is nearly the same when analyzing results from the injection of the subcritical current. In addition, the maximum Ri_ρ value required for a pure interflow, named Ri_ρ^* (i.e., $b_1(Ri_\rho^*) = 1$), is 12.5% larger in our supercritical simulations, while it was the same both in laboratory and simulated results in the subcritical regime. These differences may be likely due to the fact that we could not reproduce with the model a more accurate representation of the internal gradients of the gravity currents observed in the laboratory (i.e., different Fr). However, simulation results provided complete time and spatial series of velocity and density excess, which allowed us to confirm the physical arguments of buoyancy flux partition of the gravity current suggested experimentally, which could not be demonstrated in the laboratory.

We have simulated the injection of different tracers within the vertical profile of the gravity current in order to demonstrate that there is a height at the current $z = z_i$ such that $\Delta\rho(z) = \Delta\rho_{12}$, which divided the injected current buoyancy flux in two portions (b_1 and b_2) for that particular scenario (Figs. 3.3b and 3.3c). Thus, after 2 min since the beginning of each run (mark in bold in Table 3.2), we simulated the injection of two pulses of different tracers (named, C_1 and C_2) with the same concentration ($= 2 \text{ kg m}^{-3}$) during a period of 1 min. Both tracers were injected through the complete lateral cross-section and at the same longitudinal location ($S_N = 0.32 \text{ m}$), but throughout a different range of cells in the vertical direction: C_2 from the bottom to z_i , and C_1 between z_i and the top of the current (defined by h). Fig. 3.9 shows the simulated tracer concentration distribution of C_1 and C_2 by the end of the pulse injections ($t \sim 3 \text{ min}$), for the two studied gravity currents (subcritical in Figs. 3.9a,c, and supercritical in Figs. 3.9b,d) and similar density steps, $Ri_\rho \sim 20$. For both current regimes, higher concentrations of C_1 are observed flowing along the density step (Figs. 3.9a,b), while C_2 values are larger along the bottom of the system (Figs. 3.9c,d). As a result, we observed by the end of the pulse injections a maximum of 81% of the injected mass by tracer 1 retained at the density step (C_1 , standard deviation of 9%), while we measured up to 89% of the injected mass by tracer 2 flowing along the bottom of the tank (C_2 , standard deviation of 5%). Thus, we could assume that the experimental partition theory based on the internal gravity current gradients could be considered as physically possible. However, errors in buoyancy flux partition estimations due to measurement point should be quantified.

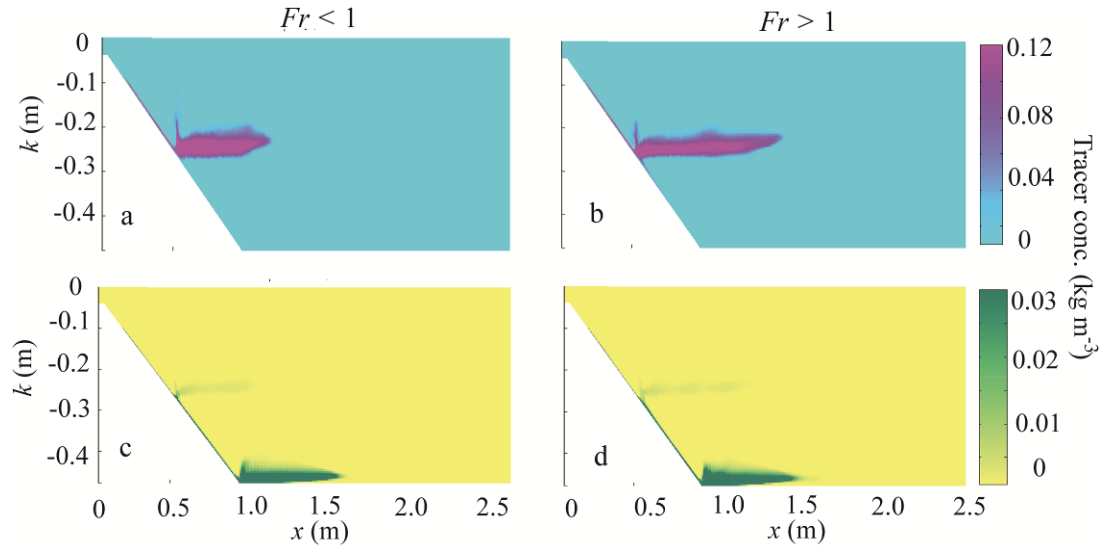


Fig. 3.9. Simulated spatial distribution of the two pulses of different tracer concentrations (C_1 and C_2) in the tank after 3 min release of the two experimental gravity currents (a,c) subcritical, and (b,d) supercritical, into a stratified system with a density step $Ri_\rho \sim 20$. Concentration of the tracer injected at the top of the current (C_1) is shown in a,b, while concentration of the tracer injected at the bottom of the current (C_2) is shown in c,d.

Two sources of error in buoyancy flux portion estimations were identified in the laboratory: (1) the measurement point of the density excess $\Delta\rho(z)$ and velocity $u_G(z)$ profiles within gravity current at the slope (S_N) before reaching the density step (S_{12} , Fig. 3.2a), and (2) the location within the tank where the ambient density changes where measured. In the laboratory, the authors showed only characteristic profiles at each location. However, in this work, we have used simulation results to evaluate the possible standard deviation in the laboratory buoyancy flux portion estimations when wider spatial ranges are considered. First, horizontal error bars in Fig. 3.5 mark the standard deviation of the simulated gravity current profiles measured over a slope range which varied $S = [0.32 - 0.5]$ m. As a result, theoretical buoyancy flux portions based on current properties (lines, Eq. 3.3) in Figs. 3.8c,d are calculated from the simulated profiles measured at $S_N = 0.32$ m, while the shaded region covers the range of predicted b values considering additional entrainment of ambient water before the gravity current reached S_{12} . We have found smaller uncertainties in predicted b values from simulated gravity current profiles ($\sim 4\text{-}10\%$) than in the laboratory ($\sim 12\text{-}15\%$). Second, horizontal error bars in the lower right corner of Fig. 3.6 show maximum standard deviation of simulated ambient density profiles by the end of the injection $\rho_{obs}(y)$ when profiles were gathered in the tank over a spatial range $x = [1.17 - 1.67]$ m. These errors in ambient density profiles were not larger than 11.4% of the maximum density values. In this case, predictions of buoyancy flux portions (symbols, Eq. 3.4) in Figs. 3.8c,d are calculated from the simulated ambient profiles measured at $x = 1.17$ m, and the vertical error bars represent the standard deviation of b values considering ambient profiles

gathered 0.5 m further in the tank. As a result, the errors in buoyancy portions due to the measurement location in the tank are of only 0.1-3.6%. Besides of evaluating the error sources due to the measurement points, simulation results have inherent errors or uncertainties, and thus, model performance evaluation is crucial in assessing modeling efficacy (Bennett et al. 2013).

Uncertainty in the numerical results - Numerical simulations have let us to gain a better understanding about the partition of a 2D gravity current entering a two-layered stratified water body. However, here we evaluate uncertainty in the modeling process from three sources of error (Ayyub 1998): (1) parametric, associated to the values of the constants used in the implemented zero-equation turbulence closure model; (2) uncertainty related with the vertical resolution of the numerical domain, and (3) uncertainty due to the boundary configuration of the inflowing current. Here, we have quantified the errors associated with the different sources.

Table 3.4. Results of buoyancy flux portions at the inflow (b_1), average gravity current properties (h , U , ΔP), and $RMSE$ from vertical profiles of two reference runs (A13 and B29, mark in bold) and a new sets of runs (a-d) to evaluate the parametric uncertainty of model results.

Variables		b_1	h (cm)	U (cm s ⁻¹)	ΔP (kg m ⁻³)	Fr	$u_G(z)$	$\Delta\rho(z)$	$\rho_{obs}(y)$
Run	Parameters	Value	Value	Value	Value	Value	$RMSE$ (cm s ⁻¹)	$RMSE$ (kg m ⁻³)	$RMSE$ (kg m ⁻³)
A13	Reference	0.43	1.61	3.36	9.50	0.86	0.850	9.869	0.827
A13a	$C_D = 0.003$	0.45	1.60	3.38	9.60	0.87	0.910	9.891	0.845
A13b	$\alpha, \beta = -1.5; 5$	0.46	1.59	3.29	9.68	0.84	0.900	10.030	0.912
A13c	$Pr_t = 20.8$	0.45	1.57	3.37	9.65	0.87	0.920	9.912	0.903
A13d	$= 18$	0.44	1.60	3.37	9.58	0.87	0.910	9.911	0.918
B29	Reference	0.53	1.95	4.34	8.10	1.10	1.550	3.812	1.427
B29a	$C_D = 0.003$	0.52	1.94	4.36	8.16	1.11	1.640	3.915	1.524
B29b	$\alpha, \beta = -1.5; 5$	0.49	1.94	4.28	8.15	1.09	1.670	3.857	1.572
B29c	$Pr_t = 5.6$	0.54	1.93	4.30	8.22	1.09	1.660	3.935	1.462
B29d	$= 4.4$	0.50	1.92	4.28	8.06	1.10	2.620	3.966	1.492

C_D - Drag coefficient

α, β - Constants of correction of the turbulent viscosity

Pr_t - Turbulent Prandtl number

h - Average thickness of the gravity current (g.c.)

U - Average velocity of the g.c.

ΔP - Average density excess of the g.c.

Fr - Densimetric Froude number of the g.

$RMSE$ - Root mean square error

$u_G(z)$ - Velocity profile of the g.c.

$\Delta\rho(z)$ - Density excess profile of the g.c.

$\rho_{obs}(y)$ - Final ambient density profile in the tank

Parametric uncertainty - A number of three parameters ($m = 3$) described when presenting the implementation of the RANS zero-equation turbulence model were considered as sources of uncertainty in the results of different modeled variables: buoyancy flux portions at the interflow (b_1), average gravity current properties (h , U , ΔP , Fr), gravity current profiles ($u_G(z)$ and $\Delta\rho(z)$), and final ambient density profile ($\rho_{obs}(y)$). The uncertainty parameters include the drag coefficient C_D (Eq. 3.5), the constants of correction of the turbulent viscosity ν_t (i.e., α and β , Eq. 3.6), and the turbulent Prandtl number Pr_t (Eq. 3.8).

The reference run was characterized by the set of values of the three parameters already described (see *Numerical model*). Then, we run new sets of cases where only one parameter value was changed in each run, in relation with the reference case. In this exercise, we have selected only two reference runs from Table 3.2 with similar Ri_p (~ 20) and different current regime (i.e., runs A13 and B29, with $Fr < 1$ and $Fr > 1$, respectively). Using the experimental and simulated values, we calculated the *RMSE* to quantitatively evaluate model performance in the new numerical cases (Table 3.4).

The ranges of the uncertainty parameters are based on values found at the literature. We selected the averaged value of C_D for smooth surfaces in the reference run ($= 0.0015$), but according to Deacon and Webb (2005) we could have chosen values up to 0.003 (runs *a* in Table 3.4). The constants of correction of ν_t chosen in the reference run were equal to $\alpha = 10$ and $\beta = -0.5$ according to Munk and Anderson (1948). However, Strang and Fernando (2001) proposed different values for the parameters, as $\alpha = -1.5$ and $\beta = 5$ (runs *b* in Table 3.4). Finally, we have already characterized the standard deviation of Ri_g below the experimental current-ambient interface, which yielded ranges of $Ri_g = [2.76-4.95]$ and $Ri_g = [0.53-0.69]$ in subcritical and supercritical regimes, respectively. Thus, we calculated (Eq. 3.8) averaged values of turbulent Prandtl number $Pr_t \sim [20, 5]$ for each regime in the reference runs, and ranges of $Pr_t = [18-20.8]$ and $Pr_t = [4.4-5.6]$ in subcritical and supercritical current regimes (runs *c* and *d* in Table 3.4).

We quantified the differences in the simulation results from the reference case and the new set of runs for each regime (where uncertainty parameters were systematically changed) in terms of the maximum relative difference, *MRD*, (La Rocca et al. 2008) as follows,

$$MRD = \max \left| \frac{S_{unc} - S_{ref}}{S_{ref}} \right| \times 100 \quad (3.10)$$

where S_{unc} is the simulated result of the study variable in the uncertainty runs (*a-d* in Table 3.4) and S_{ref} represents the value of the study variable in the reference run. Simulation results showed *MRD* in b_1 portions of $\sim 6.5\%$ for both regimes, associated with the constants of correction of ν_t (runs *b*, Table 3.4). In addition, *MRD* in average values of h , U , ΔP and Fr were found to be 2.5% and 1.5% in subcritical and

supercritical regimes, respectively, due to values of α , β and Pr_t (runs *b-d*, Table 3.4). Comparison between *RMSE* values yielded *MRD* in terms of current velocity $u_G(z)$ of 8.2%, while these differences in terms of current density excess $\Delta\rho(z)$ were about half of this value ($\sim 4\%$). When comparing the *RMSE* in terms of the final ambient density profile $\rho_{obs}(y)$, we observed *MRD* of $\sim 11\%$ in both regimes. *MRD* in all vertical profiles were linked to values of α , β and Pr_t (runs *b-d*, Table 3.4). Thus, simulation results seem not being sensitive to C_D values. Furthermore, the described ranges of the uncertainty parameters did not significantly change simulation results in relation with the reference case, according to recent numerical simulations of gravity currents (La Rocca et al. 2008; Tan et al. 2011). However, the *RMSE* between observed and simulated profiles in the new uncertainty runs was in all cases larger than the *RMSE* estimated for reference case in both regimes (Table 3.4). As a result, new values of the uncertainty parameters with respect to the reference case, (1) did not significantly change simulation results of the study variables ($< 11\%$), and (2) they did not yield better agreement between experimental and simulated results.

Vertical resolution uncertainty - Previous simulations of large scale flows conducted by Legg et al. (2006, 2009) and Xu et al. (2007) show that their ability to reproduce the splitting of gravity currents (our Fig. 3.1c) was largely dependent on whether they could resolve the internal density and velocity gradients. Thus, we evaluate the vertical resolution of the study domain as another possible source of uncertainty in our simulation results. We evaluate the error for the same modeled variables mentioned in the parametric uncertainty analysis.

We run two new sets of two-layered experiments of a 2D gravity current of constant B_0 (Table 3.2) with the values of Fr and Ri_ρ shown in Fig. 3.6, but considering two new vertical resolutions of the domain for each set of runs ($n_k = 64$ and $n_k = 32$). Note that the new 12 runs had the same number of cells in the horizontal (i) and lateral (j) direction as in the reference cases shown in Fig. 3.6 (i.e. $n_i = 256$ and $n_j = 16$). We use subscripts *f* (fine), *d* (medium) and *c* (coarse) to refer to the three study vertical resolutions, where the number of grid cells in the vertical direction n_k varied 128, 64, and 32, respectively.

According to the simulation results, higher fractions of buoyancy flux were retained at the density step for the same pair of Fr and Ri_ρ values at coarser resolutions (Table 3.5). We estimated maximum increments of simulated b_1 portions of $\sim 35\%$ when resolution was reduced from fine to medium, while this increment in b_1 reached values of 47% when the vertical discretization changed from fine to coarse. Simulation results of runs with larger values of Ri_ρ yielded pure interflows ($b_1 = 1$) as soon as the vertical resolution was reduced (e.g., B22_{f_2D} and B22_{d_2D}, in Table 3.5). Numerical simulations by Legg et al. (2006) suggested that coarse resolutions could cause excessive mixing

Table 3.5. Results of buoyancy flux portions at the inflow (b_1), average gravity current properties (h , U , ΔP), and errors ($RMSE$) from a new sets of runs (reference in Fig. 3.6) to evaluate the uncertainty of model results due to vertical resolution of inflow configuration.

Run	Variables			b_1	h (cm)	U (cm s ⁻¹)	ΔP (kg m ⁻³)	Fr	$u_G(z)$	$\Delta\rho(z)$	$\rho_{obs}(y)$
	Vert. n_k	Inflow config	$\Delta\rho_{12}$ (kg m ⁻³)	Value	Value	Value	Value	Value	$RMSE$ (cm s ⁻¹)	$RMSE$ (kg m ⁻³)	$nRMSE$ %
A5_{f,2D}	128	2D	34.28	0.62							4.8
A5 _{d,2D}	64	2D	34.28	0.87							11.1
A5 _{c,2D}	32	2D	34.28	1.00							17.2
A5 _{f,3D}	128	3D	34.28	0.65							5.5
A13_{f,2D}	128	2D	15.69	0.43	1.61	3.3	9.5	0.86	0.850	9.869	5.3
A13 _{d,2D}	64	2D	15.69	0.74	1.72	3.73	8.6	0.98	0.960	13.069	10.4
A13 _{c,2D}	32	2D	15.69	0.88	2.4	5.8	7.3	1.4	1.570	16.847	23.4
A13 _{f,3D}	128	3D	15.69	0.46	1.66	3.6	10.8	0.90	0.980	9.44	6.2
A17_{f,2D}	128	2D	6.15	0.14							16.6
A17 _{d,2D}	64	2D	6.15	0.34							19.8
A17 _{c,2D}	32	2D	6.15	0.46							28.4
A17 _{f,3D}	128	3D	6.15	0.17							20.0
B22_{f,2D}	128	2D	38.33	0.71							7.7
B22 _{d,2D}	64	2D	38.33	1.00							8.3
B22 _{c,2D}	32	2D	38.33	1.00							10.8
B22 _{f,3D}	128	3D	38.33	0.74							9.0
B29_{f,2D}	128	2D	17.05	0.53	1.95	4.34	8.1	1.1	1.550	3.812	8.4
B29 _{d,2D}	64	2D	17.05	0.89	2.83	5.2	7.7	1.23	1.900	4.406	13.1
B29 _{c,2D}	32	2D	17.05	1.00	3.7	5.4	4.2	1.37	2.550	9.476	16.3
B29 _{f,3D}	128	3D	17.05	0.56	2.05	4.86	9.2	1.20	1.440	4.218	11.3
B34_{f,2D}	128	2D	6.37	0.25							14.1
B34 _{d,2D}	64	2D	6.37	0.48							21.4
B34 _{c,2D}	32	2D	6.37	0.66							24.4
B34 _{f,3D}	128	3D	6.37	0.29							20.3

f - Fine vertical resolution
 d - Medium vertical resolution
 c - Coarse vertical resolution
 h - Average thickness of the gravity current (g.c.)
 2D - Two-dimensional inflow (confined)
 3D - Three-dimensional inflow (unconfined)
 U - Average velocity of the g.c.
 ΔP - Average density excess of the g.c.
 Fr - Densimetric Froude number of the g.c.
 $RMSE$ - Root mean square error
 $u_G(z)$ - Velocity profile of the g.c.
 $\Delta\rho(z)$ - Density excess profile of the g.c.
 $\rho_{obs}(y)$ - Final ambient density profile in the tank
 $\Delta\rho_{12}$ - Density step at the two-layered system

within the down-slope current. We confirm their hypothesis when comparing the average gravity current properties resulting from the three study vertical resolutions, since thicker, faster and less dense currents were simulated in runs where coarser resolutions were used (Table 3.5). These changes were, on average, more dramatic for the supercritical runs. In addition, runs with coarser resolutions provided worse fits between experimental and numerical results ($RMSE$ in Table 3.5). Note that the $RMSE$

at the ambient water has been normalized by the maximum density value of each run. As a result, the weaker the stratification at the density step, the larger the $nRMSE$ at the ambient water. For instance, simulations with $Fr < 1$ and $Ri_\rho = [34.28, 6.15]$ (A5 and A17, respectively, in Table 3.5) yielded $nRMSE$ at the ambient water of [4.8, 16.6] %, respectively. These results lead us to consider the vertical resolution as a possible limitation to correctly reproduce the partition (or even the splitting) of the inflow current in two intrusions (especially in supercritical regimes) when weak stratification is present.

Inflow configuration uncertainty - Although the laboratory results considered a laterally confined current, the inflow boundary configuration can be considered as another source of uncertainty in our simulation results. Laboratory experiments by Johnson et al. (1989) stressed the significance of considering the unbounded nature of the inflows ('diffusers') on determining entrainment and dilution. Furthermore, Kassem et al. (2003) used a numerical model to simulated 3D negatively buoyant flows and provided insight into processes like mixing at the plunge zone.

To test the influence of the inflow configuration in our work, we run a new set of two-layered experiments of constant B_0 (Table 3.2) with the values of Fr and Ri_ρ shown in Fig. 3.6, but with an unconfined inflow plume of 5 cm width located on the west boundary and centered within the 22 cm tank width. In this case, simulation results from unconfined plumes entering a two-layered system yielded larger fractions of buoyancy flux retained at the density step than the confined currents for the same Fr and Ri_ρ values (compare, for example, B29_{f_2D} and B29_{f_3D}, with b_1 equal to 0.53 and 0.56, respectively, Table 3.5). We estimated maximum increments of simulated b_1 portions of ~3.47% considering unconfined current with respect to confined inflows. In addition, gravity currents resulting from 3D plumes were thicker, faster and denser than when a confined plume entered the water body (Table 3.5). Also, values of densimetric Froude number Fr increase ca. 5-8% in unconfined currents, likely as a result of stronger significance of inertia forces than in the confined currents. As expected, simulated final ambient density profile ($\rho_{obs}(y)$) from 2D plumes provided better fits with laboratory results (i.e., smaller $RMSE$) than 3D plumes. In addition, simulations of unconfined currents entering the two-layered system yielded larger $nRMSE$ at the ambient water for smaller density steps (small Ri_ρ). Also, the error was larger when unconfined currents entering weakly stratified systems present supercritical regimes ($Fr > 1$), than when the 3D current had $Fr < 1$ (Table 3.5).

As a result, the arguments presented here suggest that we should carefully define the vertical resolution of the simulated domain and the inflow configuration (bounded or unbounded) in order to provide a correct representation of the inflow behavior and its partition when entering a two-layered system. In addition, special attention should be

taken for the case of supercritical currents into weakly stratified systems. Assuming that simulation results yield the sort of errors described in this section, we will use now the model to characterize the current partition process of a wider range of gravity current regimes (Fr) and stratification strengths (Ri_ρ) in terms of the changes in the internal gradients of the current due to its impingement with a density step.

Behavior of gravity currents with extreme regimes - A wide range of published field measurements (Peters and Johns 2005a; Arneborg et al. 2007; Fer et al. 2010) have shown more dramatic velocity and density vertical gradients within gravity currents than those shown in the laboratory currents studied by Cortés et al. (2014b). Thus, we have run new sets of simulations where we varied the inflow conditions (inflow thickness h_0 , velocity U_0 , and density ρ_0) but keeping the inflow B_0 as in the laboratory, in order to create gravity currents with more extreme regimes entering different two-layered stratified systems. As a result, we are going to characterize the effects of the impingement on the vertical distribution of five different gravity currents ($Fr = [0.61, 0.78, 0.86, 1.1, 1.22]$) when inflowing water bodies where the density strength varied according to five different values of $Ri_\rho \sim [5, 20, 30, 40, 60]$.

Spatial variation of the internal gradients within the currents – We observed different downstream evolution of the average vertical velocity $u_G(z)$ and density excess $\Delta\rho(z)$ along different cross-sections of the tank for the two simulated extreme current regimes (Figs. 3.10a,c with $Fr = 0.61$, and Figs. 3.10b,d with $Fr = 1.22$) entering a stratified tank with $Ri_\rho \sim 20$. In addition to the different spatial evolution of the average properties of the current (U and ΔP) depending on the current regimes (Figs. 3.10e,g subcritical, and Figs. 3.10f,h supercritical), we identified different trends in those characteristic values when we varied the density strength in the stratification (Ri_ρ). Note that the average thickness of the current h is drawn over the vertical profiles in Figs. 3.10a-d. In general for the two regimes, the current loses velocity and density but gets thicker from the inflow to a section before the density step ($x_b = 0.4$ m). After the impingement of the gravity current ($x_a = 0.6$ m), it always reduces its thickness and velocity, but either a denser or lighter current than before the density step can be formed depending on the regime (Fr) and the value of Ri_ρ (Figs. 3.10g,h). The gravity current conserves its modified average properties after the impingement until it starts flowing along the flat bottom of the tank ($x \sim 1.0$ m), where we observe a dramatic reduction of the current velocity and density but larger average current thickness than before its impingement. The reader should note that the current velocity reduction across the density step is more significant for supercritical currents and large density steps ($Ri_\rho \sim 40$, at $x_a = 0.6$ m, Figs. 3.10e,f). Similarly, density reduction due to the impingement is

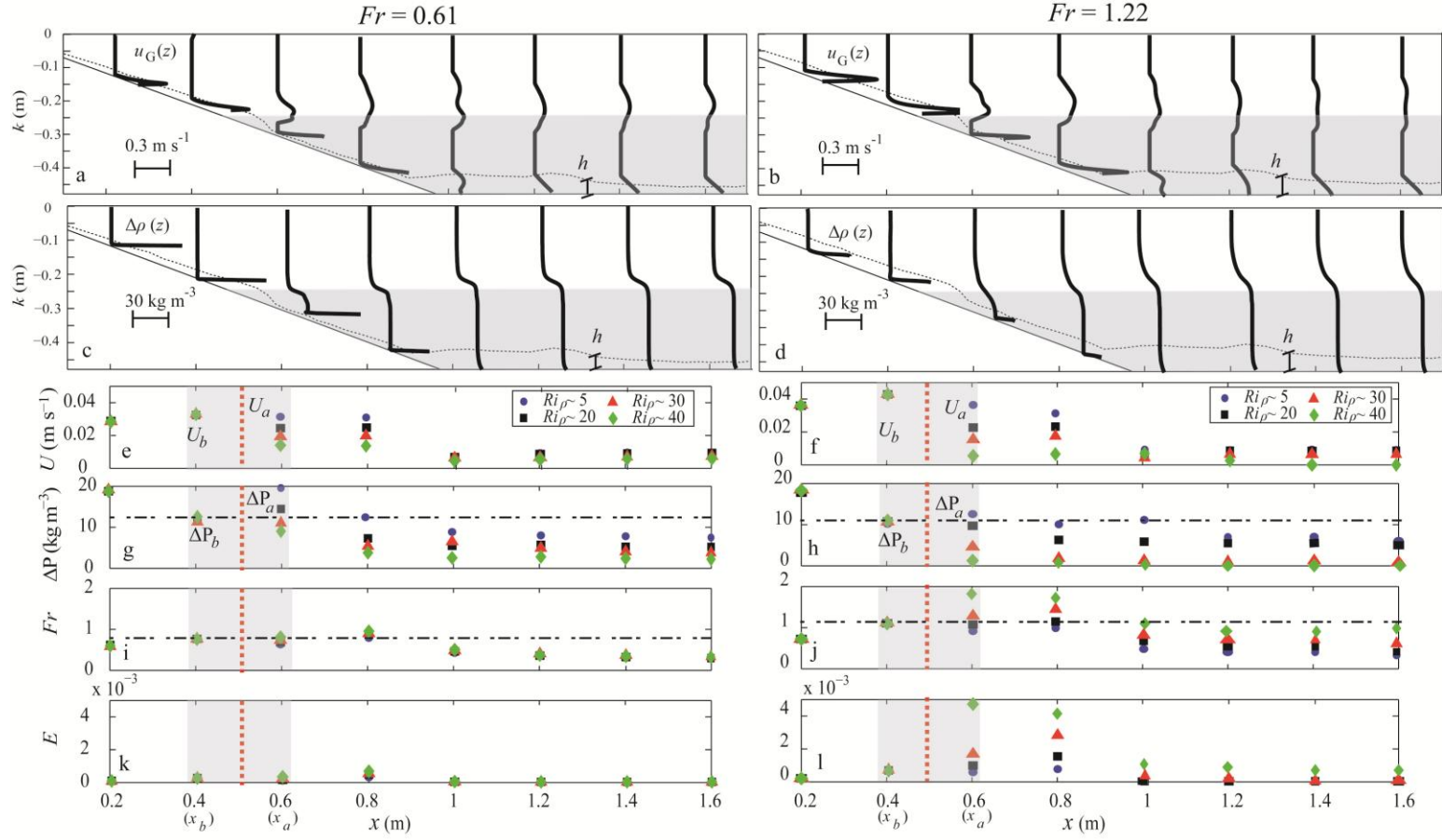


Fig. 3.10. (a-d) Downstream variation of (a,b) velocity $u_G(z)$, and (c,d) density excess $\Delta\rho(z)$ gravity current profiles along the x-direction, for the two extreme regimes study: (a,c) $Fr = 0.61$ (subcritical) and (b,d) $Fr = 1.22$ (supercritical). We mark the average current thickness, h . (e-l) Spatial variation of average properties: (e,f) average velocity, U ; (g,h) average density excess, ΔP ; (i,j) densimetric Froude number, Fr ; (k,l) entrainment coefficient, E . Different colors and symbols correspond to experiments with different density strength (Ri_ρ). We mark properties before (subscript b) and after (subscript a), the density step at S_{12} , which is represented by the red dashed line. Black dashed-dotted lines are discussed in the text.

more obvious in supercritical currents (Fig. 3.10h), since subcritical currents right after weak density steps can even become more dense (Fig. 3.10g). Hence, we are interested in parameterizations which characterize the level of internal gravity current restructuring due to the impingement of the different gravity current regimes with different stratification strengths.

Changes of average current properties due to the impingement – Recent laboratory experiments in two-layered systems have quantified the effect of the impingement on the internal structure of the gravity current (Samothrakis and Cotel 2006a,b), and proposed empirical relationships between the velocity differences across the density step against the density Richardson number (they called it ‘bottom-top’ Richardson number). Here, we have applied their procedure to our simulated velocity and density excess profiles with different Fr and Ri_ρ , as follows. We first measured simulated $u_G(z)$ and $\Delta\rho(z)$ profiles at two different locations, before ($x_b = 0.4$ m) and after ($x_a = 0.6$ m) the intersection of the density step with the slope at S_{12} (Figs. 3.2a and 3.10e-h, dashed region). Then, we evaluated the normalized change in the average velocity at the two locations as $dU_{ba}/U = (U_b - U_a)/U_b$, where U_b and U_a represent the average current velocity before and after it hits the density step, respectively. We also assessed the normalized change in the average density excess of the current in a similar manner, as $d\Delta P_{ba}/\Delta P = (\Delta P_b - \Delta P_a)/\Delta P_b$. As a result, we quantified maximum reductions of the average current velocity after the impingement from 45% to 100% when extreme current regimes ($Fr = 0.61$ and 1.22 , respectively, Fig. 3.11b) enter strongly density stratified water bodies ($Ri_\rho \sim 40$). The velocity reduction due to weak density steps of extreme current regimes is less significant (maximum of 16%), and with smaller differences depending on Fr values (ca. 10%) (Fig. 3.11b, $Ri_\rho \sim 5$). In addition, we observed that average current density can increase up to 79% after the impingement of subcritical currents with weak density steps ($Fr = 0.61$, $Ri_\rho \sim 5$), while ΔP can also decrease to minimum values when supercritical currents enter systems with large density steps, $Fr = 1.22$, $Ri_\rho \sim 60$ (Fig. 3.11c).

We found linear dependence between both normalized changes of average velocity and density excess across the density step and the stratification strength, i.e. dU_{ba}/U vs. Ri_ρ , and $d\Delta P_{ba}/\Delta P$ vs. Ri_ρ (i.e., $y = M \cdot x + J$). In addition, we have expressed the coefficients of the linear relationships (M and J) as functions of Fr , in order to generalize our equations of velocity changes across the density step for different values of both Fr and Ri_ρ , as follows,

$$\begin{aligned} \frac{dU_{ba}}{U_b} &= M_1 \cdot Ri_\rho + J_1, & \text{if } Ri_\rho < Ri_\rho^* \\ \frac{dU_{ba}}{U_b} &= -1 & , \text{if } Ri_\rho > Ri_\rho^* \end{aligned} \quad (3.11)$$

where $M_1 = -0.01613 Fr - 0.002313$, and $J_1 = -0.01538 Fr - 0.01637$ (minimum $R^2 = 0.93$, Fig. 3.11b). Furthermore, in terms of the density changes,

$$\begin{aligned} \frac{d\Delta P_{ba}}{\Delta P_b} &= M_2 \cdot Ri_\rho + J_2, \quad \text{if } Ri_\rho < Ri_\rho^* \\ \frac{d\Delta P_{ba}}{\Delta P_b} &= -1, \quad \text{if } Ri_\rho > Ri_\rho^* \end{aligned} \quad (3.12)$$

where $M_2 = -0.002213 Fr - 0.02512$, and $J_2 = -1.08 Fr + 1.565$ (minimum $R^2 = 0.90$, Fig. 3.11c). Note that the linear relationships presented above can be only applied to

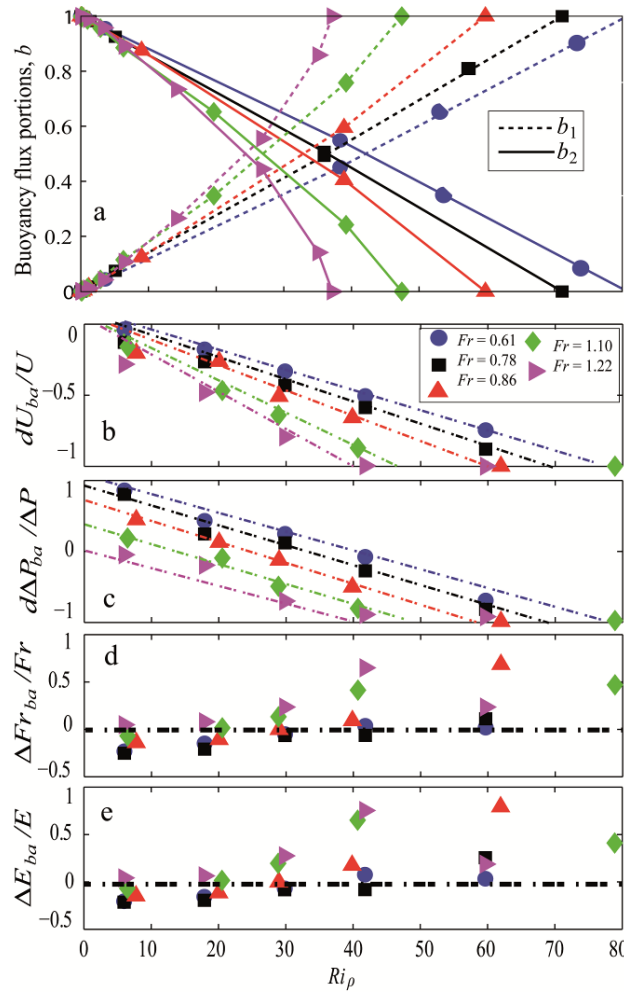


Fig. 3.11. (a) Theoretical prediction of buoyancy flux portions flowing as interflow (b_1) and underflow (b_2) of five current regimes studied through simulations. (b-e) Normalized changes of different variables across the density step against the stratification strength, Ri_ρ , for different current regimes, Fr : (b) changes of average velocity dU_{ba}/U , (c) changes of average density excess $d\Delta P_{ba}/\Delta P$, (d) changes of the densimetric Froude number $\Delta Fr_{ba}/Fr$, and (e) changes of the entrainment coefficient $\Delta E_{ba}/E$. Color dashed lines in (b) and (c) were used to estimate Eqs. 3.11 and 3.12. Black dashed-dotted lines in (d) and (e) are used in the discussion of the results.

values of Ri_ρ which yield normalized velocity changes between $[-1, 0]$, and normalized density changes from $[-1, 1]$. The value of Ri_ρ for which these changes are equal to -1 (i.e., maximum reduction of the underflow), corresponds to the critical value Ri_ρ^* above which all the current flows as an interflow (i.e., no underflow). As a result, Eqs. 3.11 and 3.12 could be used to predict the critical value Ri_ρ^* for a specific current regimen (i.e., $dU_{ba}/U = -1$ and $d\Delta P_{ba}/\Delta P = -1$), and thus, the minimum stratification strength required to observe pure interflows ($b_1 = 1$). However, we are interested in understanding the responsible processes of the different current behaviors depending on Fr and Ri_ρ . Thus, we propose a balance of forces across the density step, in order to evaluate the conditions which control the formation of interflows, underflows or split flows in our simulated experiments (Fig. 3.1).

Balance of inertial and buoyancy forces across the density step – Many field, laboratory and numerical studies of gravity currents have used the densimetric Froude number (or its inverse-related Richardson number, $Ri = Fr^{-2}$) as a measure of the importance of inertial forces to buoyancy forces (Dallimore et al. 2001; Sequeiros et al. 2010; Venayagamoorthy and Fringer 2012, among others). Here, we quantified the normalized change in Fr before and after the density step (Figs. 3.10i-j), as $\Delta Fr_{ba}/Fr = (Fr_b - Fr_a)/Fr_b$, to evaluate the driving forces of the different inflow behaviors (Fig. 3.1) depending on the current regime and stratification strengths (Fig. 3.11d). In addition, we used the predicted partition of the inflowing buoyancy flux (b portions) yielded by the different simulated current profiles (Eq. 3.4) to confirm our hypothesis about the different gravity current behaviors (Fig. 3.11a).

First, both underflows and split flows could be formed when currents enter weakly stratified systems ($Ri_\rho \sim 5-20$) depending on density and Fr changes across the density step. We consider that underflows are formed when the predicted b_1 is only $\sim 5-10\%$, while split flows could be observed if $b_1 \sim 40-50\%$ (Fig. 3.11a). Thus, when $Ri_\rho \sim 5-20$, underflows are related with $d\Delta P_{ba}/\Delta P > 0$ and $\Delta Fr_{ba}/Fr < 0$ (subcritical currents), while split flows will likely occur when $d\Delta P_{ba}/\Delta P < 0$ and $\Delta Fr_{ba}/Fr \approx 0$ (supercritical currents), (Figs. 3.11c,d). Thus, predominant buoyancy forces within the current after crossing the density step could be considered as the leading force of underflows formation. Second, we could observed both split flows and interflows for intermediate values of $Ri_\rho \sim 30-40$, when $d\Delta P_{ba}/\Delta P < 0$ and $\Delta Fr_{ba}/Fr \geq 0$ (Figs. 3.11c,d). According to the predicted current partition when $Ri_\rho \sim 30-40$, we observed that $b_1 \sim 40-50\%$ (split flows) for near zero normalized Fr changes across the density step, while $b_1 \sim 80\%$ when normalized Fr changes are above one (interflows) (Figs. 3.11a,d). Thus, the larger the increase in $\Delta Fr_{ba}/Fr$ values across the density step, the more likely the formation of interflows (supercritical currents). These results also suggest that the compensation in the reduction in both forces (inertial and buoyancy) across the density step may be a

characteristic feature of the split flow regime. Finally, only interflows are expected for large $Ri_\rho > 60$ and any current regime, since $d\Delta P_{ba}/\Delta P < 0$ and $\Delta Fr_{ba}/Fr \gg 0$. For this range of Ri_ρ , b_1 is always above 80%, confirming the predominant interflows formation (Fig. 3.11a). Thus, despite of the reduction of the current velocity, inertial forces within the current after the density step may dominate the formation of interflows. In general, the described differences in $\Delta Fr_{ba}/Fr$ can be associated with different mixing rates expressed in terms of entrainment.

The parameterization of Cenedese and Adduce (2010) used a function of the densimetric Froude number to estimate the entrainment coefficient E in gravity currents flowing downslope, as follows,

$$E = \frac{4 \times 10^{-5} + 3.4 \times 10^{-3} Fr^{7.18}}{1 + 3.4 \times 10^{-3} C_2 (Fr + 0.51)^{7.18}}, \quad \text{where } C_2 = 1 + \left(\frac{243.52}{Re^{7.18}} \right) \quad (3.13)$$

where Re is the Reynolds number (~ 25 , see *Simulations set-up*). Results of E for two extreme current regimes are presented in Figs. 3.10k,l and normalized changes of E across the density step for five different regimes are quantified as, $\Delta E_{ba}/E = (E_b - E_a)/E_b$ and shown in Fig. 3.11e. As a result, reductions in $\Delta E_{ba}/E$ are associated with underflows, while increments of this variable can be associated with split flows and interflows. Thus, higher levels of mixing between current-ambient water cause that part of (or maybe all) the current material detaches from the down-slope bottom at the density step and flows along the base of the top layer. The formation of these near surface intrusions are more likely when supercritical currents enter strongly stratified systems than when a subcritical current impact with a weakly stratified water column.

Mixing and efficiency - To properly quantify the energetic of mixing in a stratified system due to an external source (e.g., an inflowing gravity current), Winters et al. (1995) stated that simply comparing total potential energy of the fluid between the initial and final state is insufficient. They identified two possible mechanisms of energy transformation as a result of an external source of energy: diabatic and adiabatic. They further classified them depending on the nature of the total potential energy (PE) conversion: (1) irreversible, when energy is lost through viscous dissipation (diabatic), or (2) reversible, when the added energy is back into the kinetic energy budget of the fluid (adiabatic). As a result, the authors split the PE of the system into the background potential energy (PE_b), which is a measure of the potential energy from which no useful work can be derived, and the available potential energy (PE_a), which can transfer energy back into kinetic energy. In addition, Winters et al. (1995) shown in their work that the available potential energy PE_a is lost to the kinetic energy of the flow, which in turn loses its energy to dissipation. The background potential energy PE_b rises irreversibly in due to mixing is favored by turbulent motion (in our case, due to the

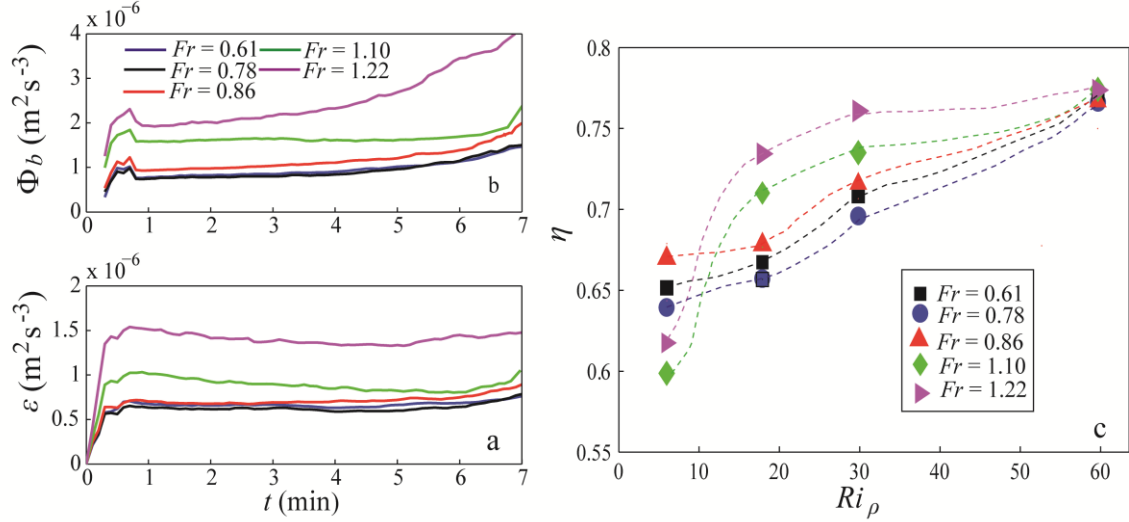


Fig. 3.12. Energy budgets. (a-b) Time-series of: (a) the rate of change of the background potential energy ($\Phi_b = \Delta PE_b / \Delta t$), and (b) dissipation ε , during the injection of different current regimes (Fr) into a two-layered system with similar $Ri_\rho \sim 20$. (c) Mixing efficiency by the end of the injection for different current regimes (Fr) and density steps (Ri_ρ).

impingement of the current with the density step). Note that in our runs we always observe a final raise of the total potential energy PE of the system ($\Delta PE / \Delta t > 0$, $\Delta t \sim 7$ min) due to the current injection. To obtain a better understanding of the mixing and dissipation of the impingement process, it is useful to analyze the instantaneous rate of change of the background potential energy ($\Phi_b = \Delta PE_b / \Delta t$) as well as the dissipation (ε). Based on these arguments, several studies (Fringer and Street 2003; Rueda and Schladow 2009) used the mixing efficiency (η) as a measure of how efficiently the PE_b rises at the expense of the PE_a of the system, which is computed as follows,

$$\eta = \frac{\Phi_b}{\Phi_b + \varepsilon} \quad (3.14)$$

where dissipation (ε) is calculated as in Fringer and Street (2003) (see their Eq. 5.5). Figs. 3.12a,b shown the time-series of Φ_b and ε for different current regimes entering a stratified system with the same density stratification ($Ri_\rho \sim 20$). On average, Φ_b tends to be twice higher than ε for any Fr and instant of time. However, values of both variables increase significantly when Fr becomes larger than one. As a result, values of mixing efficiency by the end of the injection ($t \sim 7$ min) when $Fr < 1$ are larger for higher values of both Fr and Ri_ρ according to linear-like relationships, with values of η which range between 0.64 to 0.78 (Fig. 3.12c). Nevertheless, currents with $Fr > 1$ yield the lowest values of mixing efficiency ($Ri_\rho \sim 5$), but values of η suffer a dramatic increase when $Ri_\rho > 20$, reaching the maximum mixing efficiency when $Ri_\rho \sim 60$ ($\eta \sim 0.78$). The reader should note that all our results converge to the same maximum value of mixing efficiency ($\eta \sim 0.78$) for any current regime entering the strongest stratified system. Our

values of mixing efficient are in the upper range of the values found in the literature, as summarized by Fringer and Street (2003) in Table 1 (maximum $\eta \sim 0.5$). As result, the predominant mechanism causing energy transformation in our system is through mixing (raise of PE_b) instead of viscous dissipation. These results suggest that energy introduced through gravity currents into stratified systems tend to be stored irreversibly in the PE_b , causing significant changes in the ambient stratification of the ambient water (as observed in Fig. 3.6). As shown both laboratory observations (Fig. 3.6) and energy budgets (Fig. 3.12c), the ambient density changes are more obvious for larger values of Fr (supercritical) and Ri_ρ . As a result, the scaling arguments presented here can be taken as evidence that the application of the partition theory developed in the laboratory as a function of both Ri_ρ and Fr values could be successfully extended to a wider range of gravity current regimes, which can be more easily observed in natural systems.

Conclusions and remarks

In this work we have aimed to gain a better understanding of the vertical distribution of a gravity current entering a stratified system, which can be of special interest for the biochemical processes undertaken in water ecosystems. First, we have reproduced, through numerical simulations, a recent experimental buoyancy flux partition theory based on laboratory experiments, which quantify the portion of a gravity current which flows as interflow and/or underflow after its impingement with a sharp density step. Our simulation results show good agreement with laboratory data on reproducing both: (1) the internal gradients of the two study gravity current regimes (characterized by the densimetric Froude number, Fr , as subcritical and supercritical), and (2) the change in the ambient stratification of the two-layered system (with different stratification strengths or density Richardson number, Ri_ρ) after the injection of the dense inflow. The physical validation of the modified parallel code of Fringer and Street (2003) by the implementation of a zero-equation turbulence model, allowed us to (1) successfully confirm, through tracer experiments, the physical arguments of buoyancy flux partition of the gravity current suggested in the laboratory, and (2) evaluate errors in the analytical partition theory due to both the measurement location of the available laboratory data, and numerical uncertainties associated with parameters values, vertical resolution of the numerical domain, and configuration of the inflow at the boundary (confined or unconfined). According to simulation results, changes in the locations where laboratory data were gathered did not significantly modify the predicted portions of the current that flows as interflow or/and underflow after impinging a sharp density step. Regarding numerical uncertainties, the study ranges of parameters values did not significantly change simulation results, while special care should be taken when defining the vertical resolution of the simulated domain and the inflow configuration in

order to achieve an appropriate representation of the inflow behavior entering a stratified system. In addition, particular attention should be taken for the simulation of supercritical currents into weakly stratified systems. These sources of error should be carefully studied when aiming to reproduce through simulations multiple intrusions in field scale settings. Many field gravity currents are not purely two dimensional (Alavian et al. 1992) and they are also likely to develop supercritical regimes due to a more highly mixed lower layer (Johnson et al. 1994; Xu et al. 2004). In addition, weak density steps can be developed, for example, in Mediterranean stratified reservoirs during the late summer-early fall. For instance, in the field tracer release experiments undertaken by Cortés et al. (2014a) in September 2009, stratification in Lake Bézna (Spain) presented the smallest density step ($\Delta\rho_{12} = 0.07 \text{ kg m}^{-3}$) of the observed lake stratification season (see their Figs. 1.8b,d,f), which was also the time when they observed the formation of split flows (see their Fig. 1.5).

In addition, we have further used the numerical model to characterize the current partition process of a wide range of gravity current regimes (Fr) and stratification strengths (Ri_ρ) in terms of both (1) the changes in the internal gradients of the current due to its impingement with a density step, and (2) the predominant mechanism causing the energy transformation within the stratified system due to the current injection. First, we have parameterized the level of internal gravity current restructuring due to its impingement through linear relationships between normalized changes of average properties at the current (velocity and density excess) across the density step, and the two non-dimensional numbers (Fr and Ri_ρ). In general, we observe larger variable reductions across the density step when supercritical currents enter strongly density stratified systems. Then, we have used a forces balance (buoyancy vs. inertia) in order to identify the conditions controlling the different current behavior (interflow, underflow, split flow) for the range of simulated current regimes. More significant buoyancy forces within the current after its impingement have been identified as leading forces of underflows, while predominant inertial forces after the current hits the density step may be the driver of interflows. We observed split flows when the reduction in both inertial and buoyancy forces were compensated after the current crossed the density step. Finally, we have used the mixing efficiency to properly identify the predominant energy transformation mechanism due to the injection of different gravity currents into two-layered stratified systems. Our results show larger values of mixing efficiency for higher values of Fr (supercritical) and Ri_ρ . In addition, the large values of mixing efficiency calculated suggested that energy introduced through the gravity currents into the stratified systems tend to be stored irreversibly in the PE_b , being mixing the predominant mechanism of energy transformation (instead of viscous dissipation). According to mixing efficiency trends, the ambient density changes are more obvious for larger values of Fr (supercritical) and Ri_ρ . As a result, the numerical model presented here could be taken as a tool to predict the partition of a wide range of

gravity current regimes entering different stratified systems (e.g. linearly-density stratified). However, simulation of excessive mixing could be responsible of the failure in a correct prediction of the river inflow partition in a field stratified water column. Therefore, this could lead to a wrong characterization of the fate of dissolved substance (e.g. nutrients) in the river water entering natural water bodies, which can affect the lake ecology.

GENERAL CONCLUSIONS

By means of field, laboratory and numerical experiments, we have characterized the fate of gravity currents water entering water bodies under different stratification conditions. We have demonstrated that the splitting behaviour is controlled by the presence of internal gradients within the gravity current, as well as the density change at the base of the surface-mixed layer (SML). In addition, we have described and confirm (through experimental and numerical experiments) a partition theory of the current buoyancy in two parts when it splits at a density step. These are some of the specific conclusions:

1. Results from field tracer experiments under different stratification conditions in a stratified Mediterranean reservoir (Lake Bézinar, Spain) shown that gravity currents can either penetrating the SML to form a deep metalimnetic intrusion (underflow), flowing entirely at the base of the SML (interflow), or even splitting in two parts. Our field observations also shown that a fraction (and possibly all) of river inflow entrains into the SML shortly after entering the stratified reservoir when the gravity current forms intrusions at the top of the metalimnetic layer, as a result of convectively-driven deepening of the SML. This fraction varied from 0% at the beginning of the stratification period (May) to nearly 100% at the time of maximum stratification (July). In September (late summer-early fall), this fraction (10%) was similar to that reported by Fischer and Smith (1983) in Lake Mead.
2. Under field settings, we parameterized the three behaviours of a gravity current in terms of the transition Richardson number, Ri_{12} , defined as a ratio of density step in the ambient water, and the density excess of the current at the base of the SML. The gravity current detached (at least partly) and form intrusions at the base of the SML if $Ri_{12} \geq 1$. It penetrated the base of the SML and formed intrusions only in the metalimnion, for $Ri_{12} \ll 1$. In Lake Bézinar, shallow intrusions near the base of the SML more likely occurred during strong stratification in mid-summer, but also occurred in late summer-early fall at the onset of seasonal cooling.
3. Our laboratory observations stress the significance of the internal gradients within the gravity current (quantified by the densimetric Froude number of the gravity current, Fr), as well as the ambient stratification strength (measured by the density Richardson number, Ri_ρ), on determining how a gravity current intrudes into a two-layered stratified ambient water. Gravity currents are more likely to detrain into two

parts at a density step when they have a diffuse density interface ($Fr > 1$). However, gravity currents tend to intrude as a single intrusion when they have a sharp, more step-like density profile ($Fr < 1$). According to field experiments, the formation of a diffuse interface layer at the top of the current is linked to: (1) the existence of deep surface mixed layers; (2) large initial dilutions in the plunge zone; and (3) strong mixing rates occurring at the interface layer between lake water and supercritical gravity current.

4. Using details of the internal structure of the gravity current, we developed an analytical theory to predict the partition of the inflowing buoyancy flux into the interflow and underflow when the gravity current splits at the density step. Our predictions of buoyancy portions are in agreement with the observed density changes in the laboratory stratified system.
5. Numerical experiments have let us to characterize the current partition process of a wider range of gravity current regimes (Fr) and stratification strengths (Ri_ρ) than those studied in the laboratory. We have proposed a forces balance (buoyancy vs. inertia) across the density step in order to indentify the conditions controlling the splitting behavior of the new set of current regimes. More significant buoyancy forces within the current after its impingement have been identified as leading forces of underflows, while predominant inertial forces after the current hits the density step may be the driver of interflows. We observed split flows when the reduction in both inertial and buoyancy forces were compensated after the current crossed the density step.
6. Finally, we suggest the use of a combination of the analytical buoyancy flux partition theory with the numerical model as a tool to predict and quantify the fluxes of river-borne nutrients from cold plunging inflows that could be retained at the base of the SML. Therefore, this portion of the river water, and thus its dissolved nutrients, may be available into the top layers, where they can be used for phytoplankton growth. The fate of the river-borne nutrients may influence reservoir ecology and its water quality.

CONCLUSIONES GENERALES

A través de experimentos de campo, laboratorio y simulaciones numéricas, hemos caracterizado la distribución vertical del agua introducida mediante corrientes de gravedad en sistemas acuáticos bajo diferentes condiciones de estratificación. Hemos demostrado que el comportamiento denominado *split flow* (división de la corriente en dos partes) está controlado tanto por la presencia de gradientes internos en la estructura la corriente de gravedad, como por el cambio de densidad en la base de la capa superficial de mezcla (SML). Además, hemos descrito y confirmado (de forma experimental y numérica), un teoría de partición del flujo de flotabilidad de la corriente de gravedad en dos partes cuando encuentra un salto de densidad. A continuación enumeramos una serie de conclusiones específicas:

1. Resultados de experimentos de trazadores realizados en campo bajo diferentes condiciones de estratificación en un embalse estratificado del Mediterráneo (Embalse de Béznar, Granada, España) muestran que una corriente de gravedad puede penetrar la SML para formar intrusiones en el metalimnion (*underflow*), fluir a lo largo de la base de la capa superficial de mezcla (*interflow*), o dividirse en dos partes (*split flow*). Nuestras observaciones de campo también muestran que la fracción (y posiblemente toda) del agua del río se fluye en la SML puede incorporarse en las capas superficiales del embalse en cortas escalas de tiempo debido al engrosamiento de la SML por mezcla convectiva. La fracción de agua del río incorporada en superficie varió entre 0% al comienzo del período de estratificación (Mayo) hasta casi el 100% durante el período de máxima estratificación (Julio). En Septiembre (comienzo del otoño), esta fracción (10%) fue similar a la encontrada por Fischer and Smith (1983) en el Lago Mead.
2. Bajo condiciones de campo, hemos parametrizado los tres comportamientos de una corriente de gravedad en función de un número adimensional que hemos denominado ‘*número de Richardson en la transición*’, Ri_{12} , y que cuantificamos como el cociente entre el salto de densidad en la columna de agua que observamos en la base de la SML, y la diferencia de densidad entre la corriente de gravedad y dicha capa superficial. Según nuestros resultados, la corriente de gravedad se separa del fondo (al menos parcialmente) y forma intrusiones en la base de la SML cuando $Ri_{12} \geq 1$. Por otra parte, la corriente penetra dicha capa superficial y forma intrusiones solo en el metalimnion si $Ri_{12} \ll 1$. En el Embalse de Béznar, la formación de intrusiones en la base de la capa de mezcla ocurre más

frecuentemente durante periodos de máxima estratificación (verano), pero también se observa al comienzo del otoño cuando comienza el enfriamiento de la columna de agua.

3. Nuestras observaciones de laboratorio destacan la importancia de la presencia de gradientes internos en la corriente de gravedad (cuantificados mediante el ‘*número de Froude densimétrico*’, Fr), además de la intensidad de la estratificación en la columna de agua (medida a través del ‘*número de Richardson densimétrico*’, Ri_ρ), en la caracterización del comportamiento de una corriente de gravedad cuando entra en un sistema estratificado en doble capa. Observamos que la corriente de gravedad tienen a dividirse en dos partes al chocar con un salto de densidad cuando la capa interfacial entre la corriente y el agua ambiental es difusa (corrientes con régimen supercrítico, $Fr > 1$). Sin embargo, es más probable que la corriente de gravedad forme una única intrusión cuando la capa interfacial corriente-agua ambiental es de menor espesor (corrientes con régimen sub-crítico, $Fr < 1$). Según resultado de campo, la formación de capa interfacial de mayor espesor está relacionada con: (1) la existencia de una capa superficial de mezcla profunda, (2) diluciones iniciales significativas en la zona de hundimiento; y (3) mezcla intensa en la capa interfacial entre corrientes de gravedad supercríticas y el agua ambiental.
4. Usando los perfiles verticales que caracterizan los gradientes internos de una corriente de gravedad, hemos desarrollado una teoría que predice la partición del flujo de flotabilidad inicial de la corriente de gravedad que fluye como *interflow* y *underflow* cuando dicha corriente se divide al encontrar un salto de densidad. Además, hemos confirmado nuestras predicciones sobre las fracciones en las que se divide la corriente de gravedad mediante la información de los cambios de densidad observados en el sistema estratificado debido a la entrada de dicha corriente.
5. Resultados de las simulaciones numéricas nos han permitido caracterizar el proceso de partición del flujo de flotabilidad de la corriente de gravedad con regímenes (Fr) e intensidad de la estratificación (Ri_ρ) diferentes a los estudiados en laboratorio. Hemos usado un balance de fuerzas (flotabilidad vs. inercia) a ambos lados del salto de densidad para identificar las condiciones que controlan los diferentes comportamientos de la corriente de gravedad (*interflow*, *underflow*, *split flow*) para un conjunto de nuevos regímenes. En general, nuestros resultados indican que un predominio de las fuerzas de flotabilidad en la corriente de gravedad formada tras el salto de densidad da lugar a la formación de *underflows* fluyendo por el fondo del sistema, mientras que la formación de *interflows* a lo largo del salto de densidad está asociado con una mayor importancia relativa de las fuerzas de inercia en la corriente de gravedad formada tras su impacto con $\Delta\rho_{12}$. Además, observamos *split flows* cuando la reducción de tanto las fuerzas de inercia como de flotabilidad se

compensaron tras el paso de la corriente de gravedad a través del salto de densidad del sistema estratificado en doble capa.

6. Finalmente, proponemos el uso combinado de la teoría analítica presentada sobre la partición del flujo de flotabilidad de la corriente de gravedad junto con simulaciones numéricas como una herramienta para predecir y cuantificar los flujos de nutrientes disueltos en el agua del río que pueden quedar retenidos en la base de la SML. Por tanto, esta fracción de agua del río, y sus nutrientes disueltos, podrán estar disponible en las capas superficiales donde serán utilizados para el crecimiento la comunidad fitoplanctónica. La distribución de estos nutrientes disueltos en el agua fluvial en capas superficiales puede influir en la ecología del sistema acuático natural y, por tanto, en su calidad del agua.

SCIENTIFIC PRODUCTION AND ACTIVITY

- **PUBLICATIONS**

Cortés, A., W. Fleenor, M. Wells, I. de Vicente, and F. Rueda. (2014), Pathways of river water to the surface layers of stratified reservoirs. *Limnol. and Oceanogr.*, 59(1), 233-250, doi: 10.4319/lo.2014.59.1.0233. Impact factor: 3.405

Cortés, A., F. Rueda, and M. Wells (2014), Experimental observations of the splitting of a gravity current at a density step in a stratified water body. *J. Geophys. Res.,-Oceans*. 119, 1038–1053, doi:10.1002/2013JC009304. Impact factor: 3.174

Ayala, A.I., **Cortés, A.**, W. Fleenor, F. Rueda. Seasonal scale modeling of river inflows in stratified reservoirs: structural vs. parametric uncertainty in inflow mixing, *Environ. Modell. Softw.* (in press). Impact factor: 3.476

Ramón, C., **A. Cortés**, and F. Rueda. Flow boundaries along arbitrary directions in Cartesian models, *Comput. Geosci.*, (under review). Impact factor: 1.834

Cortés, A., M. Wells, O. Fringer, R. Arthur, and F. Rueda. On the development of split flows by gravity currents into two-layered stratified basins, (under preparation to be submitted to *J. Geophys. Res.,-Oceans*)

- **NATIONAL AND INTERNATIONAL CONFERENCES**

Title: Observations and modeling of river intrusions into a stratified reservoir

Authors: **A. Cortés**, and M. Wells

Name of the Conference: 56th Annual Conference of the International Association for Great Lakes Research (IAGLR 2013)

Location: West Lafayette, Indiana, USA

Dates: 02/06/2013 to 06/06/2013

Title: Prediction of the pathways of river water entering a Mediterranean stratified reservoir (Béznar, Spain).

Authors: A. Cortés, M. Acosta, and F. Rueda

Name of the Conference: 5th International Conference of Approximation Methods and Numerical Modeling in Environment and Natural Resources (MAMERN 2013)

Location: Granada, Spain

Dates: 22/04/2013 to 25/04/2013

Title: Mixing of Density Currents Inflowing a Mediterranean Stratified Reservoir (Spain)

Authors: A. Cortés, M. Acosta, and F. Rueda

Name of the Conference: 55th Annual Conference of the International Association for Great Lakes Research (IAGLR 2012)

Location: Cornwall, Ontario, Canada

Dates: 13/05/2012 to 17/05/2012

Title: River inflow mixing in a stratified Mediterranean reservoir (Béznar, Spain)

Authors: A. Cortés, I. de Vicente, M.A. Escobar, A. Hoyer, W. Fleenor, E. Moreno and F. Rueda

Name of the Conference: 7th Symposium for European Freshwater Sciences (SEFS 2011)

Location: Girona, Spain

Dates: 21/06/2011 to 01/07/2011

Title: River inflow mixing in stratified reservoirs

Authors: A. Cortés; I. de Vicente; M.A. Escobar; A. Hoyer; W. Fleenor; E. Moreno, and F. Rueda;

Name of the Conference: 2nd International Water Association Symposium on Lake and Reservoir Management

Location: Granada, Spain

Dates: 13/06/2011 to 17/06/2011

- **CO-DIRECTION OF FINAL DEGREE PROJECTS**

Title: Control of primary production in Mediterranean stratified reservoirs: Numerical predictions of the effects of river-borne nutrients into the systems.

Student: Carlos Esteban

Degree: Civil Engineering

University: University of Granada (Spain)

End of the project: June 2014

Title: Seasonal distribution of river nutrients in Mediterranean reservoirs

Student: Ana Isabel Ayala

Degree: Civil Engineering

University: University of Granada (Spain)

End of the project: January 2013

- **RESEARCH VISITS**

Host University: University of Toronto Scarborough

Tutor: Mathew Wells

Department: Physical and Environmental Sciences

Location: Toronto, Canada

Dates: 15/05/2012 to 15/08/2012

- **GRANTS**

Name: FPI BES-2009-016091

Objective: Pre-doctoral

Organization: Ministry of Science and Innovation. Spain

Dates: 01/09/2009 to 01/09/2013

Name: EEBB-I-12-04210

Objective: Research Visit

Organization: Ministry of Science and Innovation. Spain

Dates: 15/05/2012 to 15/08/2012

REFERENCES

- Ahlfeld, D., A. Joaqui, J. Tobiasson, and D. Mas (2003), Case study: Impact of reservoir stratification on interflow travel time, *J. Hydraul. Eng.*, 129, 966–975, doi: 10.1061/~ASCE!0733-9429~2003!129:12~966
- Alavian, V., G. H. Jirka, R. A. Denton, M. C. Johnson, and H. G. Stefan (1992), Density currents entering lakes and reservoirs, *J. Hydraul. Eng.*, 118, 1464-1489, doi: 10.1061/(ASCE)0733-9429(1992)118:11(1464)
- An, S., P.Y. Julien, and S.K. Venayagamoorthy (2012), Numerical simulations of particle-driven gravity currents, *Environ. Fluid Mech.*, 12, 495-513, doi: 10.1007%2Fs10652-012-9251-6
- Arneborg, L., V. Fiekas, L. Umlauf, and H. Burchard (2007), Gravity current dynamics and entrainment: A process study based on observations in the Arkona basin, *J. Phys. Oceanogr.*, 37, 2094-2113, doi: 10.1175/JPO3110.1
- Ayyub, B. M. (1998), Uncertainty modeling and analysis in civil engineering, CRC Press.
- Baines, P. G. (2001) Mixing in flows down gentle slopes into stratified environments, *J. Fluid Mech.*, 443, 237-270, doi: 10.1017/S0022112001005250
- Baines, P. G. (2005), Mixing regimes for the flow of dense fluid down slopes into stratified environments, *J. Fluid Mech.*, 538, 245-267, doi: 10.1017/S0022112005005434
- Baines, P. G. (2008), Mixing in downslope flows in the ocean - plumes versus gravity currents, *Atmos.-Ocean.*, 46, 405-419, doi: 10.3137/ao.460402
- Bennett, N.D., B.F.W. Croke, G. Guariso, J.H.A. Guillaume, S.H. Hamilton, A.J. Jakeman, S. Marsili-Lielli, L.T.H. Newham, J.P. Norton, C. Perrin, S.A. Pierce, B. Robson, R. Seppelt, A.A.Voinov, B.D. Fath, V. Andreassian (2013), Characterising performance of environmental models, *Environ. Modell. Softw.* 40, 1-20, doi: 10.1016/j.envsoft.2012.09.011

- Botelho, D.A., and J. Imberger (2007), Dissolved oxygen response to wind-inflow interactions in a stratified reservoir, *Limnol. Oceanogr.*, 52, 2027–2052, doi: 10.4319/lo.2007.52.5.2027
- Bournet, P. E., D. Dartus, B. Tassin, and B. Vincon-Leite (1999), Numerical investigation of plunging density current, *J. Hydraul. Eng.*, 125, 584-594, doi: 10.1061/(ASCE)0733-9429(1999)125:6(584)
- Brookes, J.D., J.P. Antenucci, M. Hipsey, M.D. Burch, N.J. Ashbolt, and C. Ferguson (2004), Fate and transport of pathogens in lakes and reservoirs, *Environ. Int.*, 30, 741–759, doi:10.1016/j.envint.2003.11.006
- Casamitjana, X., T. Serra, C. Baserba, and J. Pérez (2003), Effects of the water withdrawal in the stratification patterns of a reservoir, *Hydrobiologia*, 504, 21-28, doi: 10.1023/B:HYDR.0000008504.61773.77
- Cenedese, C., J. A. Whitehead, T. A. Ascarelli, and M. Ohiwa (2004), A dense current flowing down a sloping bottom in a rotating fluid, *J. Phys. Oceanogr.*, 34, 188-203, doi: 10.1175/1520-0485(2004)034<0188:ADCFDA>2.0.CO;2
- Cenedese, C., and C. Adduce (2010), A new parameterization for entrainment in overflows, *J. Phys. Oceanogr.*, 40, 1835–1850, doi: 10.1175/2010JPO4374.1
- Chen, C. T., and F. J. Millero (1986) Precise thermodynamic properties for natural waters covering only the limnological range, *Limnol. Oceanogr.*, 31, 657-662, doi: 10.4319/lo.1986.31.3.0657
- Chen, C.J, and S.Y. Jaw (1998), Fundamentals of turbulence modeling, Taylor & Francis, New York.
- Chung, S., and R. Gu (1998), Two-dimensional simulations of contaminant currents in stratified reservoir, *J. Hydraul. Eng.*, 124, 704-711, doi: 10.1061/(ASCE)0733-9429(1998)124:7(704)
- Cortés, A., M.G. Wells, W.E. Flenoor, I. de Vicente, and F.J. Rueda (2014a), Pathways of river water to the surface layers of stratified reservoirs, *Limnol. Oceanogr.*, 59, 233-250 doi: 10.4319/lo.2014.59.1.0233
- Cortés, A., F.J. Rueda, and M.G. Wells (2014b), Experimental observations of the splitting of a gravity current at a density step in a stratified water body, *J. Geophys. Res.*, 119, doi: 10.1002/2013JC009304
- Cotel, A. J., and R. E. Breidenthal (1997), Jet detrainment at a stratified interface, *J. Geophys. Res.*, 102, 23813–23818, doi: 10.1029/97JD01695

- Cui, A. and R.L. Street (2001), Large-eddy simulation of turbulent rotation convective flow development, *J. Fluid Mech.*, 447, 53–84, doi: 10.1017/S0022112001006073
- Cui, A. and R.L. Street (2003), Large-eddy simulation of coastal upwelling flow, *J. Env. Fluid Mech.*, 4, 197-223, doi: 10.1023/B:EFMC.0000016610.05554.0f
- Dallimore, C.J., J. Imberger, and T. Ishikawa (2001), Entrainment and turbulence in a saline underflow in Lake Ogawara, *J. Hydraul. Eng.*, 127, 937–948, doi: 10.1061/(ASCE)0733-9429(2001)127:11(937)
- De Cesare, G., J. L. Boillat, and A. J. Schleiss (2006), Circulation in stratified lakes due to flood-induced turbidity currents, *J. Environ. Eng.*, 132, 1508-1517, doi: 10.1061/(ASCE)0733-9372(2006)132:11(1508)
- Deacon, E.L., and Webb, E.K., (2005), Small-scale interactions, in *Physical Oceanography*, edited by M.N. Hill, and A.R. Robinson, Harvard University Press, USA
- Elder, R. A., and W. O. Wunderlich (1972), Inflow density currents in TVA reservoirs. International Symposium on Stratified Flows, Novosibirsk, ASCE.
- Elliot, Z.A, and S.K. Venayagamoorthy (2011), Evaluation of turbulent Prandtl (Schmidt) number parameterizations for stably stratified environmental flows, *Dynam. Atmos. Ocean*, 51, 137-150, doi: 10.1016/j.dynatmoce.2011.02.003
- Ellison, T. H., and J. S. Turner (1959), Turbulent entrainment in stratified flows, *J. Fluid Mech.*, 6, 423–448, doi: 10.1017/S0022112059000738
- Fairall, C. W., E. F. Bradley, D. P. Rogers, J. Edson, and G. Young (1996), Bulk parameterization of air-sea fluxes for tropical ocean global atmosphere response experiment, *J. Geophys. Res.*, 101, 3747-3764, doi: 10.1029/95JC03205
- Fer, I., U. Lemmin, and S. A. Thorpe (2002), Observations of mixing near the sides of a deep lake in winter, *Limnol. Oceanogr.*, 47, 535-544, doi: 10.4319/lo.2002.47.2.0535
- Fer, I., G. Voet, K. S. Seim, B. Rudels, and K. Latarius (2010), Intense mixing of the Faroe Bank Channel overflow, *Geophys. Res. Lett.*, 37, L02604, doi: 10.1029/2009GL041924
- Fernandez, R., and J. Imberger (2008a), Time-varying underflow into a continuous stratification with bottom slope, *J. Hydraul. Eng.*, 134, 1191-1198, doi: 10.1061/(ASCE)0733-9429(2008)134:9(1191)

- Fernandez, R., and J. Imberger (2008b), Relative buoyancy dominated thermal-like flow interacion along an incline, *J. Hydraul. Eng.*, 134, 636-643, doi: 10.1061/(ASCE)0733-9429(2008)134:5(636)
- Fischer, H. B., E. J. List, R. C. Y. Koh, J. Imberger, and N. H. Brooks (1979), *Mixing in coastal and inland waters*, Academic, 2nd ed., London, 483 pp.
- Fischer, H. B., and R. D. Smith (1983), Observations of transport to surface waters from plunging inflow to Lake Mead, *Limnol. Oceanogr.*, 28, 258-272, doi: 10.4319/lo.1983.28.2.0258
- Fleenor, W. E. (2001), Effects and control of plunging inflows on reservoir hydrodynamics and downstream releases, Ph.D. thesis, Univ. of California, Davis.
- Flynn, M. R., and B. R. Sutherland (2004), Intrusive gravity currents and internal gravity wave generation in stratified fluid, *J. Fluid Mech.*, 514, 355-383, doi: 10.1017/S0022112004000400
- Ford, D. E., and M. C. Johnson (1983), An assessment of reservoir density currents and inflow processes, U.S. Army Corps of Engineers Waterwasy Experiment Station, Rep. 83-7. Online at dtic.mil/cgi-bin/GetTRDoc?AD=ADA137303
- Forrest, A. L., B. E. Laval, R. Pieters, and D. S. Lim (2008), Convectively driven transport in temperate lakes, *Limnol Oceanogr.*, 53, 2321-2332, doi: 10.4319/lo.2008.53.5_part_2.2321
- Freitas, C. (2002), The issue of numerical uncertainty, *Appl. Math. Model.*, 26, 237-248, doi: 10.1016/S0307-904X(01)00058-0
- Fringer, O. B. and Street, R. L. (2003), The dynamics of breaking progressive interfacial waves, *J. Fluid Mech.*, 494, 319-353, doi:10.1017/S0022112003006189
- Fringer, O. B., Armfield, S. W. and Street, R. L. (2005), Reducing numerical diffusion in interfacial gravity wave simulations, *Int. J. Numer. Meth. Fluids*, 49: 301-329. doi: 10.1002/fld.993
- Fringer, O.B., M. Gerritsen, and R.L. Street (2006), An unstructured-grid, finite-volume, nonhydrostatic, parallel costal ocean simulator, *Ocean Modell.*, 14, 139-173, doi: 10.1016/j.ocemod.2006.03.006
- Hallworth, M. A., E. H. Herbert, J. C. Phillips, and R. S. Sparks (1996), Entrainment into two-dimensional and axisymmetric turbulent gravity currents, *J. Fluid Mech.*, 308, 289-312, doi: 10.1017/S0022112096001486

- Hauenstein, W., and T. H. Dracos (1984), Investigation of plunging density currents generated by inflows in lakes, *J. Hydraul. Res.*, 22, 157-179, doi: 10.1080/00221688409499404
- Hebbert, B., J. Imberger, I. Loh, and J. Patterson (1979), Collie river underflow into the Wellington reservoir, *J. Hydraul. Div. ASCE.*, 105, 533–545.
- Herschy, R. W. (2009), *Streamflow measurements*, 2nd ed., CRC Press.
- Hohmann, R., R. Kipfer, F. Peeters, G. Piepke, D. M. Imboden, and M. N. Shimarawe (1997), Processes of deep water renewal in Lake Baikal, *Limnol. Oceanogr.*, 42, 841-855, online at: http://aslo.net/lo/toc/vol_42/issue_5/0841.pdf
- Imberger, J., and P. F. Hamblin (1982), Dynamics of lakes, reservoirs and cooling ponds, *Ann. Rev. Fluid Mech.*, 14, 153-187, doi: 10.1146/annurev.fl.14.010182.001101
- Imberger, J. (1985), The diurnal mixed layer, *Limnol. Oceanogr.*, 30, 737–770.
- Jellison, R., and J. M. Melack (1993), Algal photosynthetic activity and its response to meromixis in hypersaline Mono Lake, California, *Limnol. Oceanogr.*, 38, 818–837, doi: 10.4319/lo.1993.38.4.0818
- Jin, K.-R., J. H. Hamrick, and T. Tisdale (2000), Application of three-dimensional hydrodynamic model for Lake Okeechobee, *J. Hydraul. Eng.*, 126(10), 758-771, doi: 10.1061/(ASCE)0733-9429(2000)126:10(758)
- Johnson, T. R., and H. G. Stefan (1988), Experimental study of density induced plunging into reservoirs and coastal regions, St. Anthony Falls Hydraulics Laboratory, Rep. 245. Online at <http://conservancy.umn.edu/bitstream/113542/1/pr245.pdf>
- Johnson, T., C. Ellis, and H. Stefan (1989), Negatively buoyant flow in diverging channel, IV: Entrainment and dilution, *J. Hydraul. Eng.*, 115(4), 437–456, doi: 10.1061/(ASCE)0733-9429(1989)115:4(437)
- Johnson, G. C., R. G. Lueck, and T. B. Sanford (1994) Stress on the Mediterranean outflow plume. Part II: Turbulent dissipation and shear measurements, *J. Phys. Oceanogr.*, 24, 2084–2092.
- Kassem, A., J. Imran, and J.A. Khan (2003), Three-dimensional modeling of negatively buoyancy flow in diverging channels, *J. Hydraul. Eng.*, 129, 936-947, doi: 10.1061/(ASCE)0733-9429(2003)129:12(936)

- Kennedy, R. H. (1999), Reservoir design and operation: Limnological implications and management opportunities, p. 1-28. *In* J. G. Tundishi and M. Straskraba [eds.], Theoretical reservoir ecology and its applications. Backhuys Publishers.
- Kipfer, R, and F. Peeters (2000), Some speculations on the possibility of changes in deep-water renewal in Lake Baikal and their consequences, in *Lake Baikal*, edited by Koji Minoura, pp. 273-280, Elsevier, Amsterdam, The Netherlands.
- Klymak, J.M., and M.C. Gregg (2001), Three-dimensional nature of flow near a sill, *J. Geophys. Res.*, 106, 22295-22311, doi: 10.1029/2001JC000933
- Kulkarni, A. C., F. Murphy, and S. S. Manohar (1993), Interaction of buoyant plumes with two-layer stably stratified media, *Exp. Therm. Fluid Sci.*, 7, 241–248, doi: 10.1016/0894-1777(93)90007-6
- La Rocca, M., C. Adduce, G. Sciortino, and A.B. Pinzon (2008), Experimental and numerical simulation of three-dimensional gravity currents on smooth and rough bottom, *Phys. Fluids*, 20, 106603, doi: 10.1063/1.3002381
- Legg, S., R. W. Hallberg, and J. B. Girton (2006), Comparison of entrainment in overflows simulated by z-coordinate, isopycnal and non-hydrostatic models, *Ocean Model.*, 11, 69-97, doi: 10.1016/j.ocemod.2004.11.006
- Legg, S., B. Briegleb, Y. Chang, E.P. Chassignet, G. Danabasoglu, T. Ezer, A.L. Gordon, S. Griffies, R. Hallberg, L. Jackson, W. Large, T.M. Özgökmen, H. Peters, J. Price, U. Riemenschneider, W. Wu, X. Xu, and J. Yang (2009), Improving oceanic overflow representation in climate models: The gravity current entrainment climate process team, *Bull. Amer. Meteor. Soc.*, 90, 657–670, doi: 10.1175/2008BAMS2667.1
- MacIntyre, S., K. M. Flynn, R. Jellison, and J. R. Romero (1999), Boundary mixing and nutrient flux in Mono Lake, California, *Limnol. Oceanogr.*, 44, 512–529, doi: 10.4319/lo.1999.44.3.0512
- MacIntyre, S., J. R. Romero, and G. W. Kling (2002), Spatial-temporal variability in surface layer deepening and lateral advection in an embayment of Lake Victoria, East Africa, *Limnol. Oceanogr.*, 47, 656–671, doi: 10.4319/lo.2002.47.3.0656
- Malm, J., D. Mironov, A. Terzhevik, and L. Jönsson (1994), Investigation of the spring thermal regime in Ladoga using field satellite data, *Limnol. Oceanogr.*, 39, 1333-1348, doi: 10.4319/lo.1994.39.6.1333

- Marti, C. L., R. Mills, and J. Imberger (2011), Pathways of multiple inflows into a stratified reservoir: Thomson Reservoir, Australia, *Adv. Water Resour.*, 34, 551-561, doi: 10.1016/j.advwatres.2011.01.003
- Monaghan, J. J., R. A. F. Cas, A. M. Kos, and M. A. Hallworth (1999), Gravity currents descending a ramp in a stratified tank, *J. Fluid Mech.*, 379, 39–69, doi: 10.1017/S0022112098003280
- Monaghan, J. J. (2007), Gravity current interaction with interfaces, *Ann. Rev. Fluid. Mech.*, 39, 245–261, doi: 10.1146/annurev.fluid.39.050905.110218
- Monismith, S.G., A. Genin, M.A. Reidenbach, G. Yahel, and J.R. Koseff (1990), Thermally driven exchanges between a coral reef and the Adjoining Ocean, *J. Phys. Oceanogr.*, 36, 1332-1347, doi: 10.1175/JPO2916.1
- Morillo, S., J. Imberger, J.P. Antenucci, and D. Copetti (2009), Using impellers to distribute local nutrient loadings in a stratified lake: Lake Como, Italy, *J. Hydraul. Eng.*, 135, 564–574, doi:10.1061/(ASCE)HY.1943-7900.0000048
- Munk, W.H. and E.R. Anderson (1948), Notes on a theory of the thermocline, *J. Mar. Res.*, 7, 276-295.
- Odier, P., J. Chen, M. K. Rivera, and R. E. Ecke (2009), Fluid mixing in stratified gravity currents: The Prandtl mixing length, *Phys. Rev. Lett.*, 102, 134504, doi: 10.1103/PhysRevLett.102.134504
- Pawlowicz, R. (2008), Calculating the conductivity of natural waters, *Limnol. Oceanogr.*, 6, 489-501, doi: 10.4319/lom.2008.6.489
- Peeters, F., and R. Kipfer (2009), Currents in stratified water bodies 1: Density- driven flows, in *Encyclopedia of Inland Waters*, vol. 1, edited by Gene E. Likens, pp. 530-538, Oxford, Elsevier.
- Peters, H., W.E. Johns, A.S. Bower, and D.M. Fratantoni (2005a), Mixing and entrainment in the Red Sea outflow plume. Part I: Plume structure, *J. Phys. Oceanogr.*, 35, 569-583, doi: 10.1175/JPO2679.1
- Peters, H., and W. E. Johns (2005b), Mixing and entrainment in the Red Sea outflow plume. Part II: Turbulence characteristics, *J. Phys. Oceanogr.*, 35, 584–600, doi: 10.1175/JPO2689.1
- Price, J. F., and M. O. Baringer (1994), Outflows and deep-water production by marginal seas, *Prog. Oceanogr.*, 33, 161–200, doi: 10.1016/0079-6611(94)90027-2

- Rimoldi, B., J. Alexander, and S. Morris (1996), Experimental turbidity currents entering density stratified water: analogues for turbidities in Mediterranean hypersaline basins, *Sedimentology*, 43, 527-540, doi: 10.1046/j.1365-3091.1996.d01-21.x
- Rodi, W. (1993), Turbulence models and their application in hydraulics, A.A. Balkema, Rotterdam.
- Ruddick, B. R., and T.G.L. Shirtcliffe (1979), Data for double diffusers: Physical properties of aqueous salt-sugar solutions, *Deep-Sea Research*, 26, 775-787, doi: 10.1016/0198-0149(79)90013-X
- Rueda, F. J., W. E. Fleenor, and I. de Vicente (2007), Pathways of river nutrients towards the euphotic zone in a deep reservoir of small size: Uncertainty analysis, *Ecol. Model.*, 202, 345-361, doi: 10.1016/j.ecolmodel.2006.11.006
- Rueda, F., and G. Schladow (2009), Mixing and stratification in lakes of varying horizontal length scales: Scaling arguments and energy partitioning, *Limnol. Oceanogr.*, 54, 2003-2017, doi: 10.4319/lo.2009.54.6.2003
- Samothrakis, P., and A. J. Cotel (2006a), Propagation of a gravity current in a two-layer stratified environment, *J. Geophys. Res. C: Oceans*, 111, C01012, doi: 10.1029/2005JC003125
- Samothrakis, P., and A. J. Cotel (2006b), Finite Volume gravity currents impinging on a stratified interface, *Exp. Fluids*, 41, 991-1003, doi: 10.1007/s00348-006-0222-x
- Sequeiros, O., B. Spinewine, R. T. Beaubouef, T. Sun, M. H. García, and G. Parker (2010), Characteristics of velocity and excess density profiles of saline underflows and turbidity currents flowing over a mobile bed, *J. Hydraul. Eng.*, 136,412-433, doi: 10.1061/(ASCE)HY.1943-7900.0000200
- Sequeiros, O. E. (2012), Estimating turbidity current conditions from channel morphology: A Froude number approach, *J. Geophys. Res.*, 117, C04003, doi: 10.1029/2011JC007201
- Serra, T., J. Vidal, X. Casamitjana, M. Soler, and J. Colomer (2007), The role of surface vertical mixing in phytoplankton distribution in a stratified reservoir, *Limnol. Oceanogr.*, 52, 620-634, doi: 10.4319/lo.2007.52.2.0620
- Smith, P.C. (1975), A stream-tube model for bottom boundary currents in the ocean, *Deep-Sea Res. Oceanogr. Abstr.*, 22, 853-873, doi: 10.1016/0011-7471(75)90088-1

- Stevens, C. L., P. F. Hamblin, G. A. Lawrence, and F. M. Boyce (1995), River-induced transport in Kootenay Lake, *J. Environ. Eng.*, 121, 830-837, doi: 10.1061/(ASCE)0733-9372(1995)121:11(830)
- Stevens, C. L., and J. Imberger (1996), The initial response of a stratified lake to a surface shear stress, *J. Fluid Mech.*, 312, 39-66, doi: 10.1017/S0022112096001917
- Strang, E. J., and H. J. S. Fernando (2001), Vertical mixing and transports through a stratified shear layer, *J. Phys. Oceanogr.*, 31, 2026–2048, doi: 10.1175/1520-0485(2001)031<2026:VMATTA>2.0.CO;2
- Tan, A.W., D.S. Nobes, B.A. Fleck, and M.R. Flynn (2011), Gravity currents in two-layer stratified media, *Environ. Fluid Mech.*, 11, 203-223, doi: 10.1007/s10652-010-9174-z
- Turner, J. S. (1986), Turbulent entrainment: the development of the entrainment assumption, and its application to geophysical flows, *J. Fluid Mech.*, 173, 432-471, doi: 10.1017/S0022112086001222
- Venayagamoorthy, S. K. and Fringer, O. B. (2005), Nonhydrostatic and nonlinear contributions to the energy flux budget in nonlinear internal waves, *Geophys. Res. Lett.* 32, L15603, doi: 10.1029/2005GL023432
- Venayagamoorthy, S. K. and Fringer, O. B. (2006), Numerical simulations of the interaction of internal waves with a shelf break, *Phys. Fluids*, 18(7), 076603, doi: 10.1063/1.2221863
- Venayagamoorthy, S. K., and O. B. Fringer (2007), On the formation and propagation of nonlinear internal boluses across a shelf break, *J. Fluid Mech.*, 577, 137–159, doi: 10.1017/S0022112007004624
- Venayagamoorthy, S. K., and O. B. Fringer (2012), Examining breaking internal waves on a shelf slope using numerical simulations, *Oceanography*, 25, 132–139, doi: 10.5670/oceanog.2012.48
- Vidal, J., F. J. Rueda, and X. Casamitjana (2007), The seasonal evolution of high vertical-mode internal waves in a deep reservoir, *Limnol. Oceanogr.*, 52, 2656-2667, doi: 10.4319/lo.2007.52.6.2656
- Vincent, W., M. Gibbs, and R. Spigel (1991), Eutrophication processes regulated by a plunging river inflow, *Hydrobiologia.*, 226, 51–63, doi: 10.1007/BF00007779
- Wallace, R.B., and B. B. Sheff (1987), Two-dimensional buoyant jets in two-layer ambient fluid, *J. Hydraul. Eng.*, 113, 992-1005, doi: 10.1061/(ASCE)0733-

9429(1987)113:8(992)

- Weast, R. C. (1975), *Handbook of Chemistry and Physics*, CRC Press Inc., 56th ed., U.S.A.
- Wells, M.G, and B. Sherman (2001), Stratification produced by surface cooling in lakes with significant shallow regions, *Limnol. Oceanogr.*, 46,1747-1759, doi: 10.4319/lo.2001.46.7.1747
- Wells, M. G. and J. S. Wettlaufer (2005), Two-dimensional gravity currents in confined basins, *Geophys. Astro. Fluid*, 99, 199–218, doi: 10.1080/03091920500094456
- Wells, M. G., and J. S. Wettlaufer (2007), The long-term circulation driven by gravity currents in a two-layer stratified basin, *J. Fluid Mech.*, 572, 37–58, doi: 10.1017/S0022112006003478
- Wells, M. G., and P. Nadarajah (2009), The intrusion depth of density currents flowing into stratified water bodies, *J. Phys. Oceanogr.*, 39, 1935–1947, doi: 10.1175/2009JPO4022.1
- Wells, M. G., C. Cenedese, and C. P. Caulfield (2010), The relationship between flux coefficient and entrainment ratio in density currents, *J. Phys. Oceanogr.*, 40, 2713-2727, doi: 10.1175/2010JPO4225.1
- Winters, K.B., P.N. Lombard, J.J. Riley, and E.A. D’Asaro, (1995), Available potential energy and mixing in density-stratified fluids, *J. Fluid Mech.*, 289, 115-128, doi: 10.1017/S002211209500125X
- Wobus, F., G. I. Shapiro, J. M. Huthnance, and M. A. M. Maqueda (2013) The piercing of the Atlantic Layer by an Arctic shelf water cascade in an idealized study inspired by the Storfjorden overflow in Svalbard, *Ocean Model*, 71, 54–65 doi: 10.1016/j.ocemod.2013.03.003
- Wüest A., and A. Lorke (2003) Small-scale hydrodynamics in lakes, *Annu. Rev. Fluid Mech.*, 35, 373–412, doi: 10.1146/annurev.fluid.35.101101.161220
- Xu, J. P., M. A. Noble, and L. K. Rosenfeld (2004), In-situ measurements of velocity structure within turbidity currents, *Geophys. Res. Lett.*, 31, L09311, doi:10.1029/2004GL019718
- Xu, X., E. P. Chassignet, J. F. Price, T. M. Özgökmen, and H. Peters (2007), A regional modeling study of the entraining Mediterranean outflow, *J. Geophys. Res.*, 112, C12005, doi: 10.1029/2007JC004145

- Zang, Y., Street, R. L. and Koseff, J. R. (1994), A non-staggered grid, fractional step method for time-dependent incompressible Navier–Stokes equations in curvilinear coordinates, *J. Comput. Phys.*, 114, 18–33, doi: 10.1006/jcph.1994.1146
- Zedler, E. A. and Street, R. L. (2001), Large-eddy simulation of sediment transport: currents over ripples, *J. Hydraul. Eng.*, 127, 442–452, doi: 10.1061/(ASCE)0733-9429(2001)127:6(444)

